A Study on the Fire-Induced Progressive Collapse of Steel Plated Structures of Offshore Installations

by
Kunhou He

Submitted to the Department of Mechanical Engineering
in partial fulfilment of the requirements for the degree of

Doctor of Philosophy
at the
University College London
1st October 2021

Declaration

I, Kunhou He, confirm that the work presented in this thesis is my own. Where information has been derived from other sources, I confirm that this has been indicated in the thesis.

Name

01/03/2022 **Date**

Acknowledgements

When I was a Master's degree student, I never imagined completing the PhD course and being awarded a doctorate. However, thanks to an enormous amount of help from professors, colleagues, and family, I have finished writing my thesis. I would like to express my sincere gratitude to all of them.

First and foremost, I want to convey my heartfelt thanks to Prof. Jeom Kee Paik, my principal supervisor, for his invaluable advice, patience, and support during the research process. Despite his hectic schedule, Prof. Paik made a significant contribution to the completion of this PhD research by providing constructive criticism and scholarly guidance.

Next, I am very grateful to my subsidiary supervisor, Prof. Giles Thomas for guiding my papers, theses and research for the past several years and helping me to meet the graduation requirements. Thanks to him for providing me with his insightful comments in my research.

The large-scale physical model testing and the research study were undertaken at the International Centre for Advanced Safety Studies of the Korea Ship and Offshore Research Institute at Pusan National University, a Lloyd's Register Foundation Research Centre of Excellence since 2008.

Besides, I would like to express my appreciation to our laboratory members and colleagues, especially for Mr. Min Gyu Ryu, Mr. Hyeong Jin Kim, and others on my PhD research.

Finally, I would like to thank my parents, and this thesis is dedicated to them. Since we are a Chinese family, I want to thank them in Chinese, and I ask other readers kindly to understand that part of the acknowledgements is in Chinese.

我对我的父亲贺正全先生和我的母亲武俊清女士感激不尽。从我出生开始到现在的博士毕业，30 年来对我的养育之恩以及无微不至的关怀，对他们的感恩我无以言表。万爱千恩百苦，疼我孰如父母？他们可能无法在学术方面给予我很多帮助，但他们以自己的方式对我的生活和精神世界提供了坚实的后盾。多年留学在外无法在身边尽孝深感自责，只愿将来能做一个对社会对家庭有用的人来回报他们的养育之恩。

I wish all of them health and happiness always. Thank you very much.

01.10.2021　贺堃厚 (Kunhou He)

Abstract

For fire safety engineering of structures and infrastructures, it is required to characterise the structural crashworthiness in fires. The present study aims to develop advanced computational methodologies to simulate the crashworthiness of steel plated structures in fires. To achieve the goals, the following tasks were undertaken: (a) complete a literature review on fire safety engineering of structures, (b) examine the mechanism of structural crashworthiness in fires by large-scale physical model testing, (c) develop advanced computational models for the structural crashworthiness analysis in fires, (d) validate the developed computational models by comparison with test data, and (e) demonstrate the applicability of the developed methods to realistic plated structures in fires.

For this purpose, a physical model testing was performed on a full-scale steel stiffened plate structure under lateral patch loading in fires to obtain a fire test database. Steel plate panels of an as-built 1900 TEU containership in compliance with test facility in maximum size and capacity were considered as a reference structure, with principal dimensions of 7 m long and 4.8 m wide fitted with two transverse frames and seven longitudinal stiffeners. Lateral patch loading was applied using two loading actuators at the centre of each transverse frame. The fire test was conducted in a furnace fuelled by liquefied petroleum gas, where the maximum gas cloud temperature inside the furnace was increased up to 15% below the target ISO 834 fire curve during testing. A time history of the lateral deformations of the test structure was measured with the focus on a critical period until the structure reached the ultimate limit state (or collapse) after the fires started. Details of the test database are documented, which is confirmed to be useful for validating computational models for structural failure analysis in fires.

Additional work was completed to experimentally examine the effects of passive fire protection application on the fire collapse of steel stiffened plate structures. Another full-scale physical model testing was conducted where the test set-up is the same as the previous one, but the transverse frames (primary strength members) were protected with cerawool which is a fire protection material. The structural collapse was monitored at discrete time intervals from when the fire started until the test structure entirely collapsed. The effect of

fire-protected transverse frames on the structural collapse was investigated by comparison with test results on the structure that was unprotected from the fires. It is confirmed that passive fire protection is an efficient option to delay structural collapse.

New computational models for the analyses of heat transfer (from ambient to steel temperatures) and fire-induced progressive collapse behaviour of steel stiffened plate structures without or with PFP were developed using transient thermal elastic-plastic large-deformation finite element models. A comparison between test data and numerical computations was made to validate the developed computational models. It is confirmed that modelling the steel structure and PFP as shell elements in a single layer is successful and the developed computational methods are useful for both heat transfer analysis and nonlinear structural response.

To demonstrate that the developed computational models can be applied to the analysis of the heat transfer and fire-induced progressive collapse behaviour of the topside structures of a ship-shaped offshore installation, a hypothetical VLCC-class floating, production, storage and offloading (FPSO) unit hull structure is considered, and CFD simulations involving fire events under three gas release levels were performed. Transient thermal elastic-plastic large-deformation finite element models were used. Finally, the applicability of the newly developed computational models is verified.

Impact Statement

Steel-plated structures are important in a variety of marine- and land-based applications, including ships, offshore platforms, bridges, power plants, and cranes. The structures and infrastructures constructed with these members are subjected to various types of actions and action effects that are usually normal but sometimes extreme or even accidental. Fires are one of the most common causes of major accidents. Characterising structural actions and their effects in fires is highly nonlinear and non-Gaussian in association with multiple physical processes, multiple scales, and multiple criteria. Besides, it involves several variables which are time and space variants.

To investigate the failure mechanism of steel plated structures in fires, full scale or large-scale physical testing is highly demanding. The present study provides a fire test database on the collapse of full-scale steel stiffened plate structures without and with PFP. The test database presented in this thesis can be useful to validate computational models for the structural crashworthiness analysis in fires in association with PFP.

This thesis also focuses on the applications and industry practices of computational models. It presents advanced computational models for structural crashworthiness analysis in fires in association with PFP. It is helpful in effectively managing fire accidents within the framework of quantitative risk assessment and management. Hence, it is useful for future research methods. The novelty of this study and its contribution to the industry is the development of a practical procedure for the analysis of the fire-induced progressive collapse of steel plated structures with complex geometries which may be a contribution to fire safety engineering. This study provides good information for fire-structural analysis procedure and fire safety for offshore structures in-service conditions.

Four papers have been published in international journals. The author hopes that the present study can be used both inside and outside academia to save lives, preserve assets and protect the environment.

Published Articles

List of Journal Articles

1. **He KH**, Kim HJ, Thomas G and Paik JK (2022). Analysis of fire-induced progressive collapse for topside structures of a VLCC-class ship-shaped offshore installation. Ships and Offshore Structures, DOI: 10.1080/17445302.2022.2027681.

2. Ryu MG, **He KH**, Lee DH, Park SI, Thomas G and Paik JK (2021). Finite element modeling for the progressive collapse analysis of steel stiffened-plate structures in fires. Thin-Walled Structures, 159: 107262.

3. Paik JK, Ryu MG, **He KH**, Lee DH, Lee SY, Park DK and Thomas G (2021). Full-scale fire testing to collapse of steel stiffened plate structures under lateral patch loading (part 1) – without passive fire protection. Ships and Offshore Structures, 16(3): 227-242.

4. Paik JK, Ryu MG, **He KH**, Lee DH, Lee SY, Park DK and Thomas G (2021). Full-scale fire testing to collapse of steel stiffened plate structures under lateral patch loading (part 2) – with passive fire protection. Ships and Offshore Structures, 16(3): 243-254.

List of Conference Proceedings Articles

1. **He KH**, Kim HJ, Thomas G and Paik JK (2021). Progressive fire collapse of ship-shaped offshore installation topsides. The 2021 International Conference on Ships and Offshore Structures, 7th September, Hamburg, Germany.

2. Paik JK, Ryu MG, **He KH**, Lee DH, Lee SY, Park DK and Thomas G (2019). Large scale physical model testing on the collapse of a steel stiffened plate structure in fires. The 12th International Symposium on Plasticity and Impact Mechanics, 2nd October, Busan, South Korea.

3. Paik JK, Ryu MG, **He KH**, Lee DH, Lee SY, Park DK and Thomas G (2019). Large scale physical model testing on the collapse of a steel stiffened plate structure with passive fire protection in fires. The 12th International Symposium on Plasticity and Impact Mechanics, 2nd October, Busan, South Korea.

4. Ryu MG, **He KH**, Lee DH, Park SI, Thomas G, Paik JK (2019). Computational models for the fire collapse analysis of steel stiffened plate structures with or without passive fire protection. The 12th International Symposium on Plasticity and Impact Mechanics, 2nd October, Busan, South Korea.

Table of Contents

List of Figures

List of Tables

Abbreviations

ABS	American Bureau of Shipping
ASTM	American Society for Testing and Materials
BS	British Steel Institute
CFD	Computational Fluid Dynamics
DAL	Design Accidental Load
DNV	Det Norske Veritas
EMSA	The European Maritime Safety Agency
EN	European Norm
FCAW	Flux-Cored Arc Welding
FE	Finite Element
FEA	Finite Element Analysis
FEM	Finite Element Method
FPSO	Floating, Production, Storage and Offloading
FSE	Fire Safety Engineering
FSI	Fluid-Structure Interaction
HSE	Health, Safety and Executive
ISO	International Standard Organization
NIST	National Institute of Standards and Technology
PFP	Passive Fire Protection
QRA&M	Quantitative Risk Assessment and Management
VLCC	Very Large Crude Oil Carrier

Nomenclatures

a	Length of plating
B	Breath of stiffened plate structure
b	Breadth of plating
b_f	Breadth of flange
B_{Oij}	Welding-induced initial deflection
E	Elastic (Young's) modulus of material
h_c	Convection heat transfer coefficient
h_w	Height of web
i	Half-wave numbers in the x direction
j	Half-wave numbers in the y direction
L	Length of stiffened plate structure
q_c	Heat flux by convection per unit area
q_r	Heat flux by radiation per unit area
q_{total}	Total heat flux per unit area
r	Radius of gyration
S	Stephan-Boltzmann constant
T	Gas cloud temperature
t_f	Thickness of flange
t_w	Thickness of web
w_O^c	Column-type initial distortion of the support members
w_O	Initial deflection function
w_{Opl}	Plate maximum initial deflection
β	Plate slenderness ratio

λ	Column slenderness ratio
ε_f	Fracture strain (elongation)
ε_g	Emissivity coefficient of gas
ε_s	Emissivity coefficient of steel
θ_g	Gas cloud temperature
θ_m	Steel surface temperature
σ_T	Ultimate tensile strength
σ_Y	Yield stress

Chapter 1 Introduction

1.1 Background

Ships and offshore structures with more advanced technology continue to be developed to produce offshore oil and gas in deep water and hostile environments (Paik and Thayamballi 2003, Paik 2022). Operated in extreme marine environments, offshore installations are inherently threatened by various hazards that cause harmful consequences such as damage to assets, injury to or death of operators, business disruption, interruption of oil and gas production and pollution of the surrounding environment (Spouge 1999).

The main hazards include fires, explosions, dropped objects and ship collisions (DNV 2010). According to the trends report of the International Union of Marine Insurance of Global Marine Insurance Casualty, from 2012 to 2016 the number of vessels lost or damaged beyond repair directly caused by fire or explosions is about 10 percent of the total losses. In offshore installations, more than 70% of accidents spring from hydrocarbon explosions and fires that involve blast effects and heat (HSE 2005). The European Maritime Safety Agency (EMSA 2019) surveyed ship casualties and incidents with a total of 25,614 cases have occurred during 2011–2018, showing that over 75% of accidents were due to fires and explosions in some years.

Over the years, many fire accidents in ships and offshore structures have occurred. The Piper Alpha disaster on 6th July 1988 remains the worst offshore oil disaster in history that 167 people were killed (Shallcross 2013). On 6th January 2018, the SANCHI oil tanker accident in the East China Sea caused a serious fire, and the oil tanker eventually sank eight days later. All 32 seafarers aboard died in the accident (Yin et al. 2022). Fire safety design to respond to these potential fire risks should be considered.

In many fires and explosions, heat causes the mechanical properties of the structure to decrease significantly and lead to collapse. The collapse of structures is highly nonlinear and non-Gaussian in association with multiple physical processes, multiple scales, and multiple criteria. Therefore, resolving the related issues is not straightforward (Paik 2015). For fire safety engineering, it is essential to identify the structural crashworthiness (their responses) in fires. To achieve this, advanced technologies should be developed.

The structures that are most likely to be exposed to fire (such as hydrocarbon fire) and/or explosion hazards are the ship structures and FPSO (ship-shaped offshore structure) and the topsides of offshore drilling platforms, which treat combustible oil and gas and are consistently exposed to hydrocarbon fires and explosions with the potential for disastrous consequences (Czujko and Paik 2012a, 2012b). Plated structures are a key component of all of these structures. Steel stiffened-plate panels are used in naval, offshore, mechanical, and civil engineering structures as primary strength sub-structures. The present study focuses on the crashworthiness of steel plated structures in fires.

1.2 Problem Statement

For fire safety engineering, structural failure characteristics must be identified by looking at how structures deform with time after fires start. They are a nonlinear problem associated with multiple physical processes, multiple scales and multiple criteria. Advanced computational models for the structural failure analysis in fires are available in the literature, but it is highly demanding to validate the computational models by comparison with physical model test databases. As similarity laws are unavailable to convert small scale models to full-scale prototype structures, full scale or large-scale physical testing is highly demanding to capture fire physics and structural failure mechanisms. Cong et al. (2005) performed fire testing on the collapse of a largescale steel I-girder. Whilst some fire tests on framed structure models on small and large scales are reported in the literature (Wainman and Kirby 1987, ISO 1999, Rahmanian and Wang 2009, BS 2014), no full-scale fire testing on steel plated structures has previously been conducted.

Furthermore, passive fire protection (PFP) is recognised as an effective option to protect structures in fires (Shetty et al. 1998, Cozzani et al. 2006, Landucci et al. 2009, Roberts et al. 2010, Ahmad et al. 2013, Kim et al. 2013, Friebe et al. 2014, Mroz et al. 2016, Bradley et al. 2019, Lim et al. 2019, Paik 2020). It is very important to quantify how much PFP contributes to delaying the structural collapse so that a greater period can be attained in the process of escape and evacuation. A fire test database on the collapse of a full-scale steel stiffened plate structure with passive fire protection is required.

For the analysis of these full-scale physical model tests, new computational models for the analyses of heat transfer and fire-induced progressive collapse behaviour of steel stiffened plate structures without and with PFP is required. Numerous useful studies are found in the literature in association with the fire-induced progressive collapse analysis of land-based structures which are rather portal frames than plated structures (Lou et al. 2018, Suwondo et al. 2019, Parthasarathi et al. 2018, Sun et al. 2012, Shan et al. 2020, Shan et al. 2019, Fu et al. 2020, Gernay et al. 2018). Moreover, it is necessary to apply the newly developed computational models to genuine steel plated structures under fire, such as ship structures and offshore installations, in order to demonstrate their applicability.

1.3 Aims and Scope

The primary aims of this study are to develop new computational models for the analyses of heat transfer and fire-induced progressive collapse behaviour of steel stiffened plate structures without or with PFP. For this purpose, transient thermal elastic-plastic large-deformation finite element models are required. The application of the new methods is demonstrated in the consequence analysis of the progressive collapse behaviour of the topside structures of a ship-shaped offshore installation in fire events. The detailed objectives of the present study are as follows:

Creating fire test database on the collapse of full-scale steel stiffened plate structures without or with PFP.

Analysing the heat transfer and nonlinear structural response for steel stiffened plate structures without and with PFP.

Validating the computational models by comparison with the test data.

Applying the developed numerical methods to a hypothetical VLCC-class floating, production, storage and offloading (FPSO) unit hull structure.

1.4 Structure of the Thesis

The thesis is prepared and organised in the following manner (Figure 1.1).

Chapter 1 presents an overall outline of the thesis, as well as its background and aims.

Chapter 2 is a review of the literature on fire risk assessment and management. The methods of the existing procedures (heat transfer analysis

and structural crashworthiness analysis) are studied and the approaches of physical model testing are reviewed.

Chapter 3 presents details of the large-scale physical model testing on the steel stiffened plate structures without and with PFP in fires. Test databases such as steel temperatures and lateral deformations are established.

In Chapter 4, advanced computational models for the analyses of fire-induced progressive collapse behaviour without or with PFP is formulated at the elevated temperature including heat transfer analysis and nonlinear structural responses analysis. These are validated by comparing the numerical results with tests results.

In Chapter 5, an application study is carried out on a hypothetical VLCC-class FPSO unit hull topside structure to demonstrate the applicability of newly developed computational methods. In addition. The fire CFD simulation is performed to determine the distribution of the gas cloud temperature.

Chapter 6 provides the conclusions and findings of this study. It gives answers to the thesis research questions and identifies the implications of the work concerning both the academic discipline and the industrial practices. According to the limitations of this study, the future research direction is discussed.

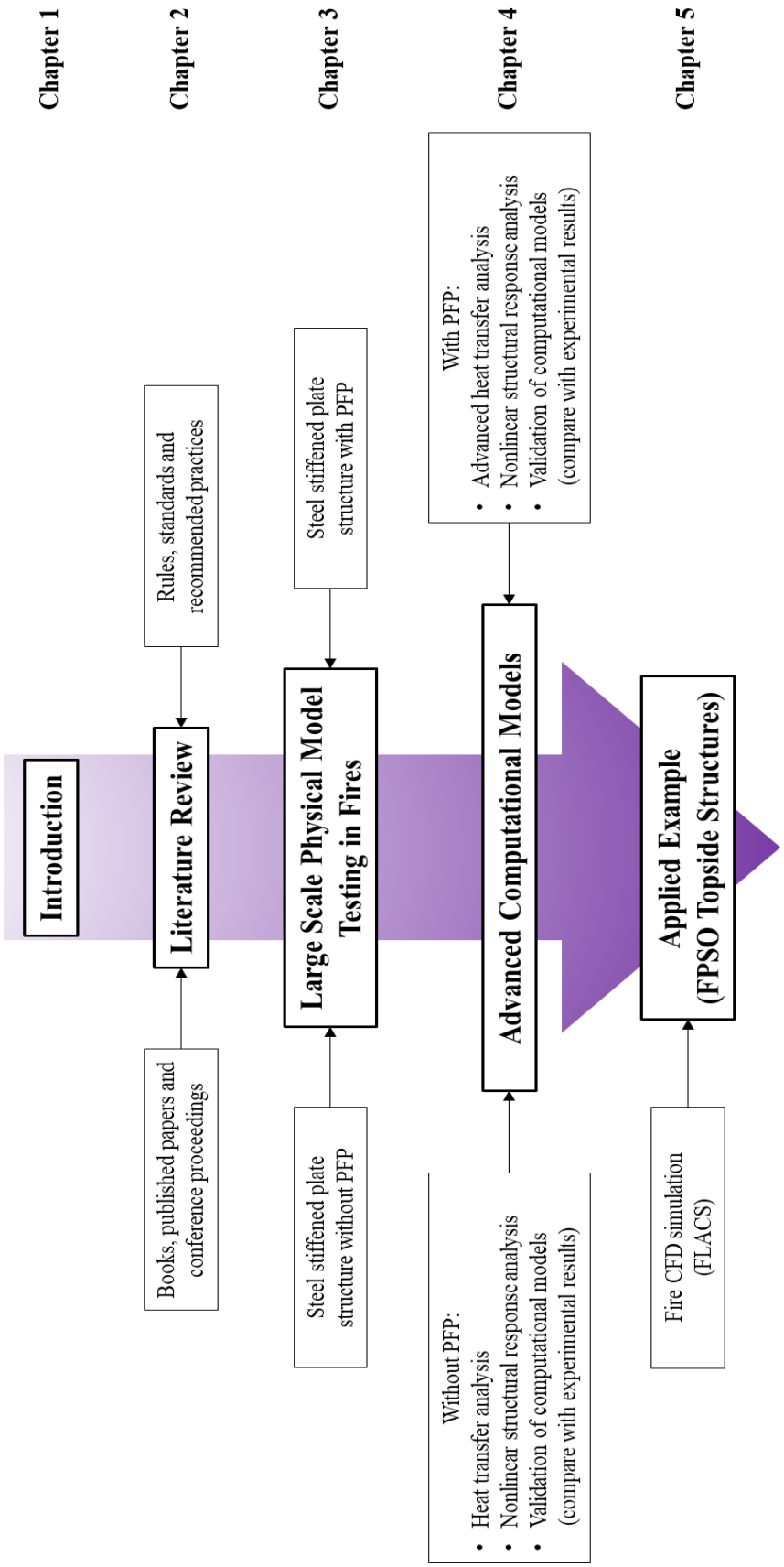

Figure 1.1 Structure of the thesis.

1.5 Contributions and Innovations

The effects of PFP application on the fire collapse of steel stiffened plate structures are experimentally examined. Fire safety engineering requires quantification of how much PFP contributes to delaying the structural collapse so that a greater period can be attained in the process of escape and evacuation. Time history of the lateral deformations of the test structures is measured with the focus on a critical period until the structure reached the ultimate limit state (or collapse) after the fires started. Details of the test database are documented to contribute to producing a fire test database on the collapse of full-scale steel stiffened plate structures without and with PFP, which will be useful for validating computational models for structural failure analysis in fires. The test database fills in the gaps of the experimental data of full-scale fire-induced progressive collapse analysis of plated structures.

New computational models for the analyses of heat transfer and nonlinear computations of the fire-induced progressive collapse behaviour of steel stiffened plate structures without or with PFP are presented. Transient thermal elastic-plastic large-deformation finite element models are formulated. The novelty of this thesis is associated with a new practical procedure for analysing the fire-induced progressive collapse analysis of large-scale steel stiffened-plate structures with complex geometries which is critical for a contribution to fire safety engineering of steel plated structures. The developed computational models will be useful to quantify the fire consequences within the framework of quantitative risk assessment. For fire safety engineering, not only the fire collapse loads but also the critical period until the collapse is reached should be determined. The proposed methods can help ensure the safety of engineering structures and infrastructures in fire events and determine the critical period for establishing the safety scheme of escape and evacuation.

The main contributions of this study are the fire test database on the collapse of full-scale steel stiffened plate structures without and with PFP, modelling of fire degradation of the material, the use of PFP within the FEM element, the correlation to the experimental data and the potential application for determining the benefits of PFP in practical applications.

Chapter 2 Literature Review

2.1 Introduction

The central theme of the present literature review is about the crashworthiness of structures in fires. The main objectives are divided into four divisions. Firstly, the study of quantitative fire risk assessment and management includes fundamentals of fire safety engineering and procedure for assessing fire risk. Secondly, the heat transfer analysis from gas cloud temperature to surrounding structures. Thirdly, the computational models for structural crashworthiness analysis in fires which includes nonlinear finite element method modelling and modelling technique for structures without and with PFP. Finally, review surveys on the published work that is relevant to the fire test (experimental study).

In this chapter, the presented theories, approaches, methodologies, ideas and applications from various literature are studied and evaluated. The methodologies that can be used for the present study are learned and the gaps in previous research are discussed. In the end, the major contributions of significant studies to the knowledge under review are summarised.

2.2 Quantitative Fire Risk Assessment and Management

Fire hazards exist in natural and industrial environments and even in people's homes. Fire is one of the most significant accidents that may lead to catastrophes affecting personnel, asset and the environment. Fire is defined as "an exothermic chemical reaction that emits heat and light" in Webster's Dictionary. According to NEPA-921 (2017), "Fire is a rapid oxidation process, which is a chemical reaction resulting in the evolution of light and heat in varying intensities." The brief procedure for quantitative assessment and management of fire risks in structures and infrastructures is presented in this chapter.

2.2.1 Fundamentals of Fire Safety Engineering

According to ISO/TR 13387-1 (1999), the main purposes of "Fire Safety Engineering" (FSE) is to:

- quantify the risks and hazards of fire and evaluate its effects
- save life, protect property, and preserve the environment and heritage

- to limit the consequences of fire within prescribed levels the necessary measurements of optimum prevention and protection should be evaluated analytically

To achieve these, the fire scenario, the effect of fire and the reaction and behaviour of people should be assessed scientifically with the application of rules, engineering principles and expert judgement.

2.2.2 Procedure for Assessing Fire Risks

To prevent fire accidents from escalating and develop proactive measures detailed knowledge of relevant phenomena and their consequences is required. This has been reflected in the fire risk assessment and management, which includes presented rules and recommended practices, which have been identified for reducing the risk of fire accidents (Spouge 1999, NORSOK 2010, Czujko and Paik 2012a, 2012b, ABS 2014, LR 2014). Moreover, to detail the means of risk assessment and management the design guidelines have been established by Paik and Czujko (2012). Figure 2.1 illustrates the procedure for Quantitative Risk Assessment and Management (QRA&M) of offshore installations in fires, as proposed by Paik et al. (2013), which aims to assess and manage fire risks in a quantitative manner. Generally, the risk is defined as a product of frequency and consequence. Thus, the main task is to accurately calculate the frequency and consequences of specific events within the framework of risk assessment and management. Structural design and safety assessment both require the identification of the actions and action effects of fire (DNV 2011, Hirdaris et al. 2015).

The industry has tried to provide a combination of control, detection, mitigation, and prevention measures to reduce the risk. These measures should be consolidated at the concept design stage when design and operating philosophies are established, and the systems should be designed to meet these philosophies as well as normal engineering acceptance criteria. In this situation, the concept of “design accidental load” (DAL) has been introduced to ensure the safety of offshore installations (Kim et al. 2016). The purpose of identifying and assessing the DAL is to verify that accidents do not cause risks that exceed the defined criteria for the design of the structures (HSE 2000).

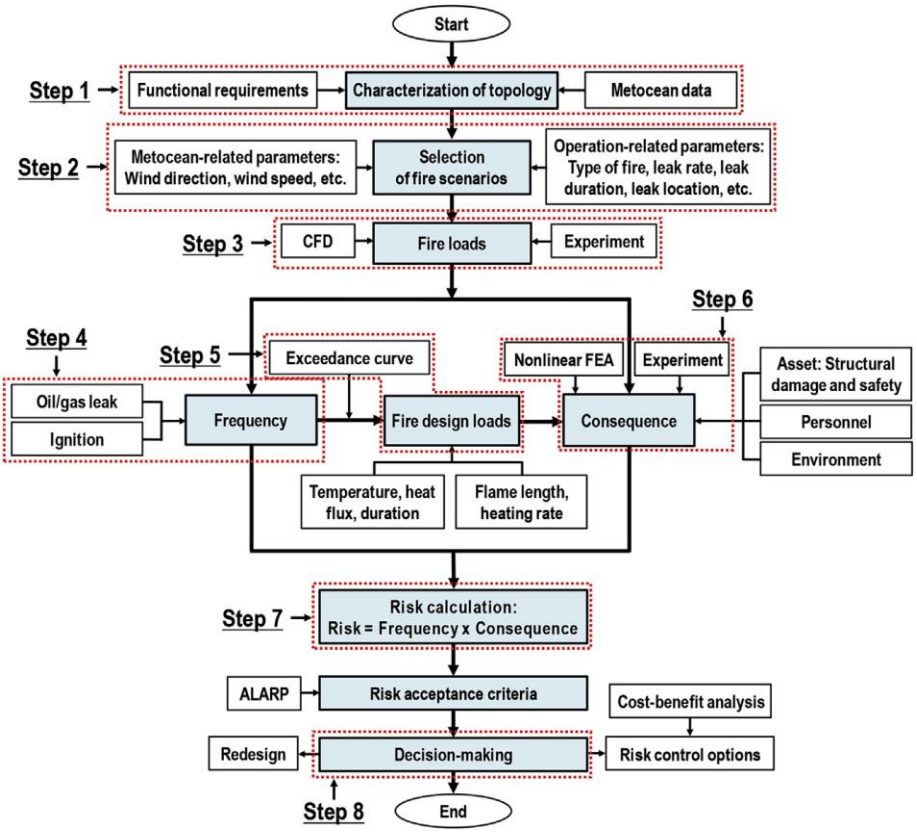

Figure 2.1 The procedure for the quantitative fire risk assessment and management (Paik et al. 2013, Paik 2020).

Essentially, the conventional fire safety engineering approaches include a series of standards, procedures, and regulations. To make it more pragmatic, complementing these approaches with integrated fire safety engineering approaches that are based on performance in principle is necessary (Paik 2020). Integrated fire safety engineering requires the analysis of heat transfer from gas cloud to structure (Section 2.3) and nonlinear structural response analysis (Section 2.4).

2.3 Heat Transfer Analysis

To estimate heat fluxes and gas cloud temperatures which are associated with the characteristics of heat sources temporally and spatially in fires, CFD simulations are commonly applied. The fire load is physically correlated with the elevated temperatures and heat fluxes in the gas cloud obtained by fire CFD simulations. In determining fire loads the radiation and convection associated with fire are crucial roles (Paik 2020).

In fire safety engineering, according to NIST (2018), the unit of heat flux is kW/m^2 which means the rate of heat energy transferred per unit area. The rate of fire releases heat energy is called heat release rate which is measured in the unit of Joules per second (J/s) or watts (W). It is known that heat is always transferred from hotter objects to colder objects. Paik (2020) illustrates that in the heat transfer process conduction, convection and radiation are important factors of fire dynamics. Conduction is heat transfer between contracting solids or within solids. The heat transfer caused by the movement of liquids or gases is convection. The heat transfer caused by electromagnetic waves is radiation.

According to Purkis (2006) and Franssen (2010), it is assumed that the heat flux is constant throughout fire in the conventional fire safety design of a structure. This means fire heats in each direction and every area is the same with uniform intensity. Conversely, in actual physics, the heat transfer process involves space-variable and time-variable conduction, convection and radiation which result in continuous change in temperature with time. As shown in Figure 2.2, the conventional approach oversimplifies these factors.

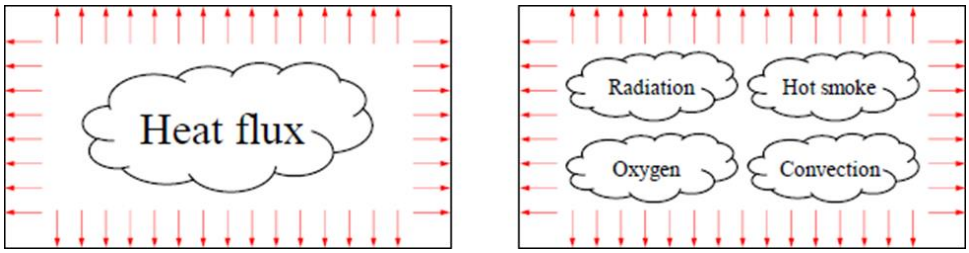

Figure 2.2 Conventional assumption (left) and actual physics (right) in fire load characterisation (Paik 2020).

2.4 Structural Crashworthiness Analysis in Fires

As a result of fire loads, structures and infrastructures in fires exhibit highly nonlinear responses due to elevated temperatures and heat fluxes until and after the collapse. As described in previous chapters, such analysis is the significant goal within the framework of quantitative fire risk assessment and management. An approach for the consequence of nonlinear structural analysis in fires is shown in Figure 2.3.

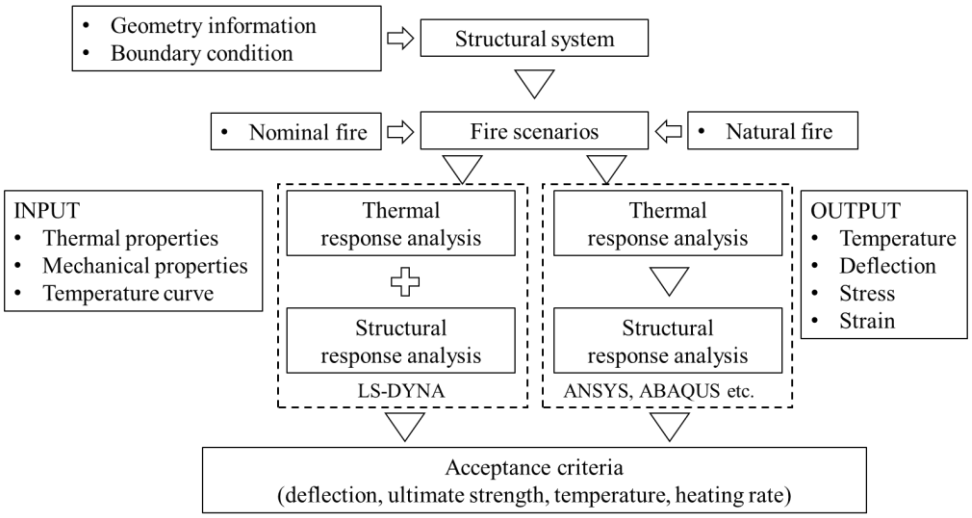

Figure 2.3 Procedure for nonlinear structural consequence analysis in fires (Paik et al. 2013).

For the fire scenarios section, there are two relevant fire load profiles: nominal fire and natural fire. The nominal fire load profile represents an artificial fire, where the temperature increases gradually with time until it reaches a peak temperature and then the temperature remains constant with time. When defining design fire loads the nominal fire load profile is the one that is mostly considered. Natural fire is represented by the natural fire load profile, due to the energy of the heat source eventually exhausted the temperature decreases after a peak temperature. Fire load profiles are usually characterised in terms of ambient or gas cloud temperature-time history via computational fluid dynamics (CFD) simulations. Fire load profiles are then applied to considered structures in the crashworthiness analysis. The effect of heat transferred to structures from the gas cloud temperatures is identified via heat transfer analysis (so-called thermal analysis). Finally, the result from transferred temperatures and external forces are structural consequences (Paik 2020).

There are two methods of structural crashworthiness analysis in fires, the one-way method and the two-way method. According to Paik (2020), a one-way method is a sequential approach. Its prediction of the fire load profile, heat transfer analysis, and structural response analysis are conducted sequentially in a single way. Furthermore, the interacting effects between fire loads and structural responses with time are not considered. The two-way method captures fire consequences more realistically. To be specific,

prediction of the fire load profile, heat transfer analysis, and nonlinear structural response analysis are conducted simultaneously.

Using typical quantitative risk assessment (QRA) outputs, Celnik and Murray (2016) proposes an efficient approach for determining firing loads on targets. This method can be applied to engineering designs to optimise equipment layout, obstacles, and passive fire protection by combining discrete target analysis and area analysis.

2.4.1 Nonlinear Finite Element Method Modelling

2.4.1.1 Beam Element Models Versus Plate-Shell Element Models

Nonlinear finite element method modelling is widely used for both heat transfer analysis and structural crashworthiness analysis in fires. The structures are commonly modelled using beam elements, plate-shell elements, or both in the engineering community. Moreover, utilising plate-shell elements is more desirable to capture nonlinear responses properly. Figure 2.4 shows a non-uniform temperature distribution of the web section of an I-section girder in fires. Paik et al. (2013) indicate that with multiple nodes on the web section in the plate-shell element model the non-uniform temperature distribution can be captured properly. However, with a single node on the web section in the beam element model, the temperature distribution is unable to be represented correctly, as it should be dealt with uniformly. In some special computation models, the temperature distribution may be approximated at most linearly rather than uniformly. This is still insufficient to accurately capture the actual physics. This recommendation for finite element method (FEM) modelling shall be applied in both the heat transfer analysis and the nonlinear structural response analysis (Paik 2020).

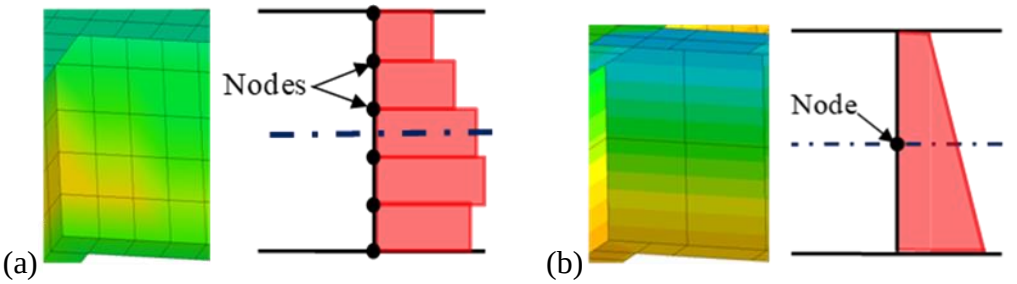

Figure 2.4 Schematic non-uniform temperature distribution of an I-section girder web in FEM (a) plate-shell element model with multiple nodes (b) beam element model with a single node (Paik et al. 2013).

2.4.1.2 Thermal and Mechanical Properties of Materials

The thermal and mechanical properties of materials are the main factors affecting structural integrity in fires. It is required to define accurately the thermal and mechanical properties of structural members precisely to identify the responses of the structures more accurately in fires. For heat transfer analysis, the thermal properties of materials should be defined in association with thermal conductivity. Temperature affects the strength and stiffness of materials. Mechanical properties of conventional structural steel and fire-resistant steel at elevated temperatures (Kumar et al. 2021) were studied.

According to the EN 1993-1-2 (2005), the specific heat and conductivity of steel vary with temperature, as shown in Figure 2.5(a) and (b). The Appendix A.1 and A.2 provides the databases as shown in Figure 2.5. The density and Poisson's ratio are respectively 7850 tonnes/m^3 and 0.29.

The types of steel used to construct the hull structures of ship-shaped offshore facilities are dictated by classification society standards or suggested practices (Paik 2022). The steel must have good buckling and fatigue resistance, as well as be corrosion resistant. In a hull construction, the proportion of reduced thickness, high strength steel should be minimised and the proportion of ordinary steel (e.g., grade A) should be maximised. Structural members that need an ordinary steel plate with a thickness greater than 30 mm, on the other hand, can be constructed from high strength steel to prevent heavy welding and simplify the construction. High-strength steel has a stronger corrosion resistance than low-strength steel, which is significant for the lengthy on-site life required in a ship-shaped offshore installation. Three grades of steel are utilised in the fabrication of hulls for ship-shaped offshore facilities that will be in operation at sub-zero temperatures. Steel grade D is suitable for use at -20°C, steel grade E is suitable for use at -40°C, and steel grade F is suitable for use at -60°C.

Based on the data provided by EN 1993-1-2 (2005), the reduction factor of carbon steel increases with the increase of temperature which leads to decreases in yield strength, elastic modulus and proportional limit value. As shown in Figure 2.6(a), a non-continuous segment plot is based on this definition. At temperatures above 400 ℃, the mechanical properties of steel

decrease significantly. The remaining yield strength is 47% of the original yield strength at 600 ℃, 11% at 800 ℃. The engineering stress-strain curve of carbon steel at various temperatures is illustrated in Figure 2.6(b).

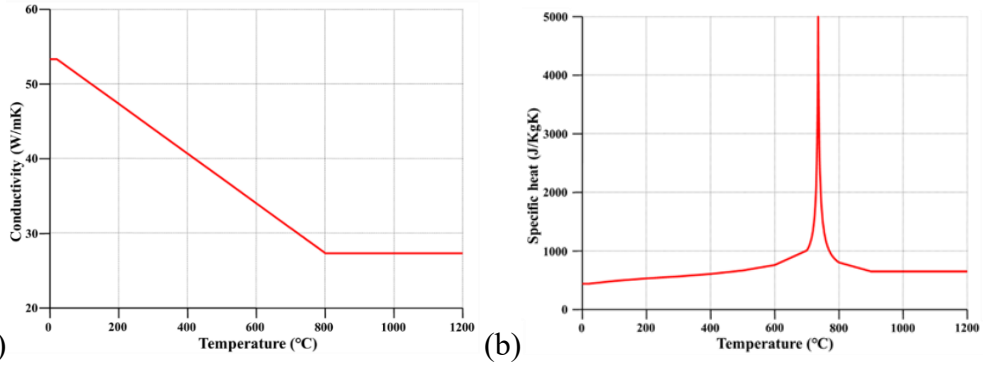

Figure 2.5 Thermal properties of carbon steel (a) thermal conductivity of carbon steel (b) specific heat of carbon steel (Paik et al. 2013).

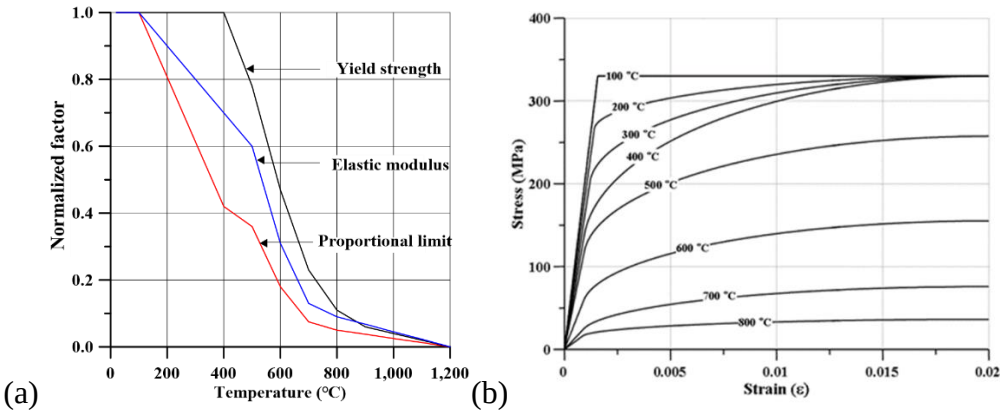

Figure 2.6 Effect of elevated temperature on material properties (a) reduction in the mechanical properties of carbon steel at elevated temperatures (b) illustrative stress-strain relations of carbon steel at elevated temperatures (Paik et al. 2013).

2.4.2 Modelling Technique for Structures Without and With PFP

Mechanical behaviour affected by heat transfer phenomena and design loads to the structure is defined through fire collapse analysis. Figure 2.7 shows the procedure for fire collapse analysis (Kim 2014). Initially, the gas temperature profile was selected by using computational fluid dynamics (CFD) simulation or the reliable gas cloud temperature distribution curves. Secondly, depending on the presence of PFP, the method for steel temperature prediction

was selected to calculate the steel temperature from gas temperature. Finally, coupled thermal and structural response analyses were conducted.

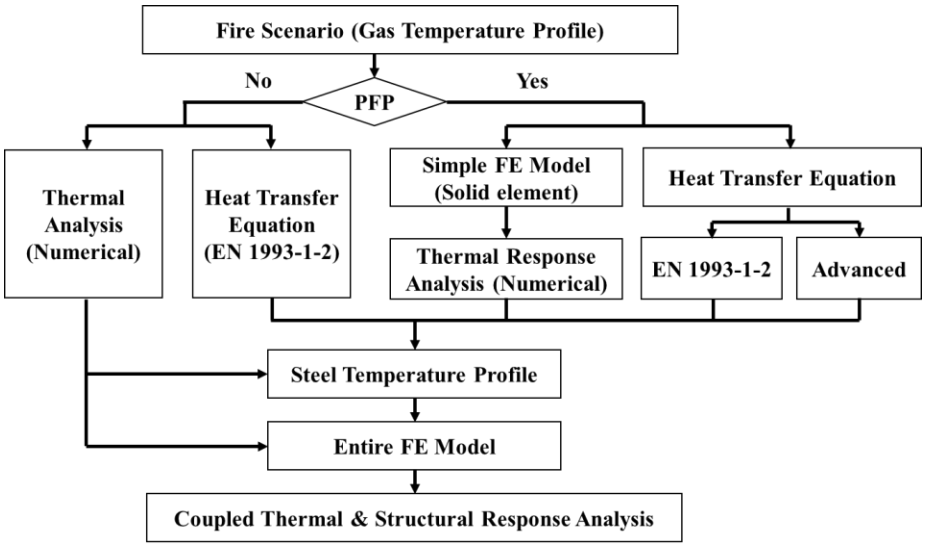

Figure 2.7 The procedure of thermal analysis without and with PFP (Kim 2014).

There are two methods to calculate the steel temperature from gas temperature, namely the thermal analysis method and the heat transfer equation method. Heat transfer equations for structures without PFP and with PFP in fires were obtained from EN 1993-1-2. Thermal analysis methods for steel structure without PFP were conducted with modelling finite element (FE) model with shell element (Paik et al. 2013) which is easy and proved to be accurate. In the case of PFP, thermal analysis methods for structure with PFP were conducted by modelling FE model with solid elements.

Conversely, in the case of the presence of PFP, modelling the FE model with solid elements to perform thermal analysis requires review. This is caused by the modelling of the structure with solid elements for the PFP, which takes considerable time when the geometry of the structure is complex. To improve this, Paik (2020) conducted a new modelling method of heat transfer analysis by modelling the steel structure and PFP as shell elements in a single layer using LS-DYNA. The fire test data on the gypsum board (PFP material) obtained by Rahmanian and Wang (2009) were used as a reference. The steel plate is 6 mm thick with the size of 1 m × 1 m. The thermal and mechanical properties of gypsum board PFP was defined in advance. The

bottom side of the steel plate with gypsum board was subjected to the gas cloud temperature. It was assumed that the gas cloud temperature distribution is uniform. Heat loss on the unexposed side was also considered, where heat flux due to convection and radiation is applied. The thermal load was applied following the profile obtained from the physical test (Rahmanian and Wang 2009). Figure 2.8 shows the different modelling techniques (solid element and shell element) in LS-DYNA conducted by Paik.

This shell element modelling technique reduces pre-posting processing and makes it easier to change the PFP thickness, and it reduces the number of elements and nodes.

After the comparison of the steel temperature results versus time of the solid element method and shell element method with varying gypsum board thickness. It is found that for the relatively thin PFP the results of the shell elements model were in good agreement with the results of the solid elements model. The comparison results of the heat transfer analysis show that modelling steel and PFP as shell elements in a single layer can accurately calculate the temperature of the steel plate.

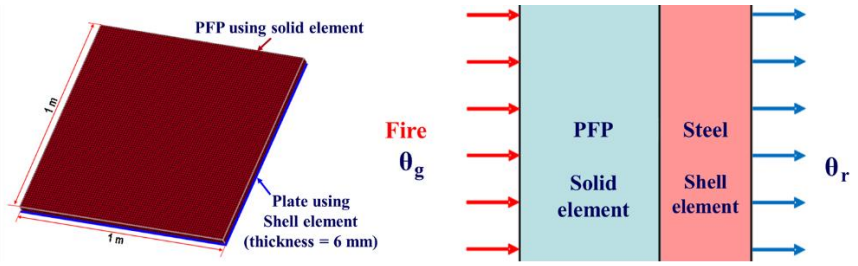

(a) FE Model of steel plate with PFP using solid element (b) Concept of steel plate with PFP using solid element

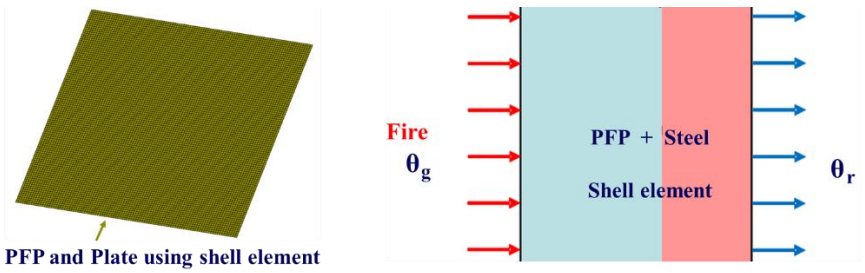

(a) FE Model of steel plate with PFP using shell element (b) Concept of steel plate with PFP using shell element

Figure 2.8 FE Model and concept of Steel plate with PFP using different modelling techniques (Paik 2020).

Effects of the structural strength of fire protection insulation systems in offshore installations (Park et al. 2021) were studied, it was found that the structural influence of insulation material should be considered.

2.5 Experimental Study

The fire collapse physical model testing conducted by Cong et al. (2005) in Southeast University in Nanjing, China is studied. Figure 2.9 shows the schematic of the test. Table 2.1 provides the dimensions of the test beam.

An I-section steel beam simply supported at both ends is subjected to uniform lateral loads that are kept constant at q = 10 N/mm. At ambient temperature (i.e. 20 ℃) the yield stress and elastic modulus of the steel beam are 330 MPa and 210 GPa, respectively with the Poisson's ratio of steel being 0.3. The beam is put inside of a horizontal furnace with hot air temperatures elevated by an oil burner. Figure 2.10 shows the deformation of the beam at collapse state.

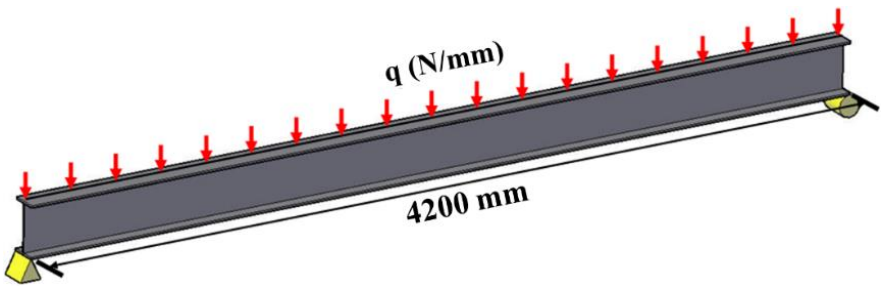

Figure 2.9 I-section steel beam simply supported at both ends subjected to uniform lateral loads (Paik 2020).

Table 2.1 Dimensions of the steel beam (Paik 2020).

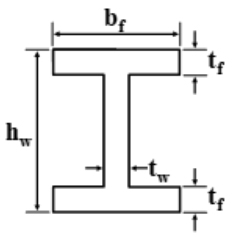

h_w	250 mm
b_f	125 mm
t_w	6 mm
t_f	9 mm

Figure 2.10 Deformed shape of the beam at collapse state obtained in the experiment (Cong et al. 2005).

Experiments on steel structures in fire and under load are extensive, and there are review papers covering a lot of these (Maraveas 2019). Other than the steel structure exposed in fires without any protection, the fire tests conducted with passive fire protection (PFP) on a structure are also studied. For instance, the fire test on the gypsum board (PFP material) obtained by Rahmanian and Wang (2009) is mentioned in Section 2.4.2, as shown in Figure 2.11.

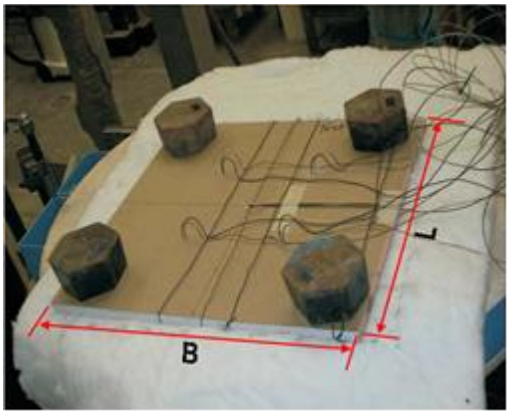

Figure 2.11 Test set-up for the fire test on gypsum board PFP (Rahmanian and Wang 2009).

Gypsum board is a cementitious-type PFP that is widely used on land-based structures. The test specimen is a steel plate 6 mm thick in the size of 1 m × 1 m. The bottom side of the steel plate is protected with a gypsum board. And the protected side is placed horizontally on top of the heat source (subjected to the gas cloud temperature). The other side that faced upward is exposed to the room temperature (19-25 °C). To insulate the contact surface between the heat source and the specimen, 30 mm thick glass wool is laid underneath the specimen. The temperatures on both the exposed and unexposed sides of the

gypsum board are measured using thermocouples. During the test, the thermal load is applied following the profile which is similar to the standard cellulosic fire described in Section 2.3.

A series of fire tests conducted by the British Steel Corporation (1987) are also studied. I-section steel beam subjected to a constant uniform line load of 45.8 N/mm with its temperature elevated inside of a furnace were tested. The beam is simply supported at both ends. The length of the beam is 4,000 mm and the dimensions of the beam are similar to the test conducted by Cong et al. (2005). The present study investigates two sets of testing: one without and one with PFP. For the test without PFP, all four sides are exposed to heat and the steel temperature profiles are identical for all sections. For the set with PFP, the upper flange is protected with PFP (concrete slab-type PFP) so only three sides are exposed to heat. Due to the concrete slab-type PFP, it was found that the peak temperature of the upper flange is 200 °C lower than other sections.

2.6 Concluding Remarks

The fundamental purpose of the present literature review is to conduct review surveys on the published work that is relevant to the crashworthiness of structures in fires. Quantitative fire risk assessment and management provides a basic idea of the procedure for assessing fire risk. It is found that the conventional approach (heats flux is constant) oversimplifies actual physics (space-variable and time-variable). The conduction, convection and radiation in the heat transfer process should be considered. For the review work for structural crashworthiness analysis in fires, the framework of nonlinear structural consequence analysis in fires are established. Two-way method is more realistic than the one-way method. For the nonlinear finite element model for structures and PFP. Shell element modelling reduces pre-posting processing and easy to change the thickness of PFP. After the experimental study, it is found that most of the published work on fire tests are in association with the fire-induced progressive collapse analysis of land-based structures which are rather portal frames than plated structures (Lou et al. 2018, Suwondo et al. 2019, Parthasarathi et al. 2018, Sun et al. 2012, Shan et al. 2020, Shan et al. 2019, Fu et al. 2020, Gernay et al. 2018) and it lacks a test database from large-scale physical model testing for plated structures where

the scaling effects should be minimised to validate the computational methods. Based on these the key research questions are formulated as follow:

- What is the mechanism of crashworthiness of stiffened plate structures in fires? How to examine the structural crashworthiness in fires?
- How to develop advanced computational models to simulate such structural crashworthiness of steel stiffened plate structures in fires?

The answers to these questions will be discussed at length in subsequent chapters.

Chapter 3 Large-Scale Physical Model Testing in Fires

3.1 Introduction

This chapter aims to contribute to producing a fire test database on the collapse of full-scale steel stiffened plate structures without and with passive fire protection under lateral patch loading. The test database is created to validate computational models for structural failure analysis in fires (Chapter 4). In this chapter, the test method and set-up will be illuminated to give background knowledge and provide a better understanding of the computational method.

High strength steel AH32 was selected to be the raw material for the test structures. A series of material tensile tests at different temperatures were conducted. The stiffened plate structure was designed by referencing those on actual vessels. Its dimension in the present fire test is 4.8 m × 7 m, with seven longitudinal stiffeners and two transverse frames. The test was undertaken using a horizontal-type furnace test facility in KOSORI, South Korea (www.icass.center). To prevent any undesired movements of the stiffened plate structure and to create an enclosed environment for the elevated gas cloud temperature, test jigs were designed and built along the four edges around the stiffened plate structure. The test structure was turned over and placed right above the furnace, so only one side of the structure was exposed to the elevated temperature. On the other side, the stiffened plate structure was subjected to lateral patch loads perpendicular to the plate at the centre of two transverse frames since they are the primary support members of the plated structure. The lateral patch load was applied at two and three steps for the fire test without and with PFP, respectively. It was intended to start from a low load and increase it until after the structure collapsed. At each loading step, the magnitude of load application was kept constant so that the applied loading was considered a “dead load”. For the test with PFP, passive fire protection was applied to two transverse frames (primary support members of the plated structure). Figure 3.1 is the schematic of the overall test plan.

The test structures were designed to meet two elements: full-scale structure and KOSORI test facility capacity. Based on preliminary studies of progressive fire collapse responses using the nonlinear finite element method, full-scale hull structures of 1,900 TEU containership were chosen for the testing in terms of structural scantlings, longitudinal stiffener spacing,

transverse frame spacing, etc. As presented in Chapter 4 for computational models and Chapter 5 for applied examples of ship-shaped offshore installations, the thesis aims to develop computational models for the progressive fire collapse analysis of steel plated structures in fires. In upper deck structures of ship-shaped offshore installations, lateral loading mostly arises in the form of (unchanging) dead loads on decks due to the weight of heavy facilities and they are primarily resisted or sustained by strong transverse frames rather than thin plates. The loading condition in the testing was chosen to reflect this situation. However, such full-scale model testing is very expensive and thus loading condition was changed once during the testing to obtain the effect of different loading conditions in the same testing. This idea was considered because the developed computational models will be validated for the progressive fire collapse analysis despite any complex loading conditions that may happen in reality.

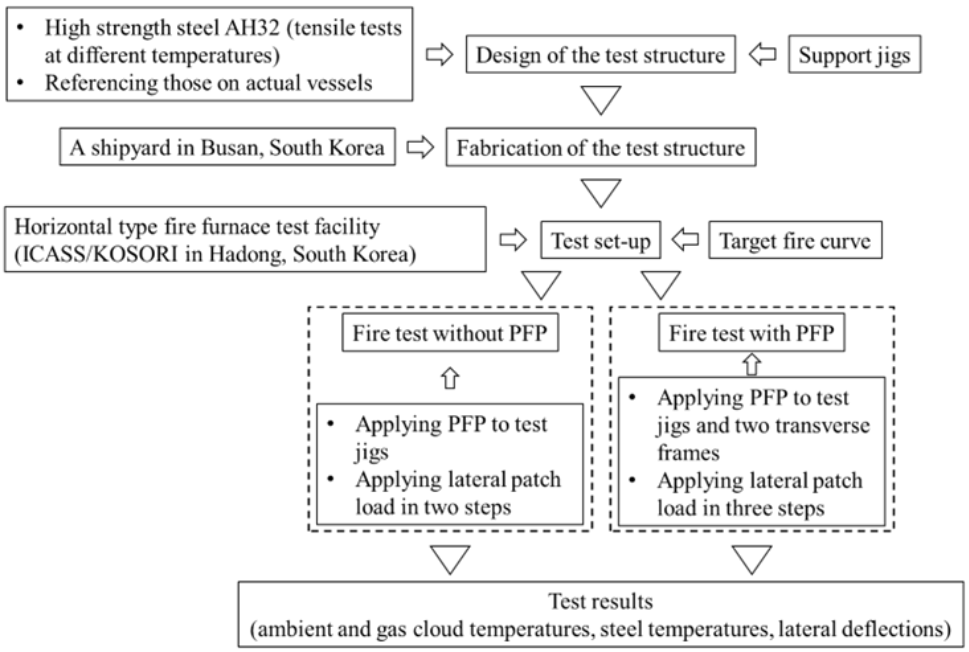

Figure 3.1 Test plan.

3.2 Design of the Test Structure

Steel plate panels of an as-built containership carrying 1,900 TEU as shown in Figure 3.2 are considered. Figure 3.3 denotes the nomenclature of the test structure. Properties of plate panels are characterised by the plate slenderness

ratio, β and the column slenderness ratio of longitudinal stiffeners with attached plating, λ, as follows.

$$\beta = \frac{b}{t}\sqrt{\frac{\sigma_Y}{E}}, \tag{3.1}$$

$$\lambda = \frac{a}{\pi r}\sqrt{\frac{\sigma_Y}{E}}, \tag{3.2}$$

where a is the length of plating (or spacing between transverse frames), b is the breadth of plating (or spacing between longitudinal stiffeners), t is the thickness of the plating, E is Young's modulus, σ_Y is the yield stress of the material, and r is the radius of gyration of longitudinal stiffener with attached plating.

The scantlings of the test structure model which is made of high tensile steel with grade AH32 were determined in compliance with the capacity and size of the test facility. Figure 3.4 shows the drawing of the test structure design. Table 3.1 compares the geometric properties for a reference plate panel versus the test structure.

Support jigs were also designed and constructed to attain a strong support condition along four boundaries of the test structure model associated with the furnace facility. Figure 3.5 shows the drawing of the support jigs which are made of the same high tensile steel with grade AH32 as for the test structure. The support jigs may represent a fixed boundary condition for the structural crashworthiness analysis using computational models.

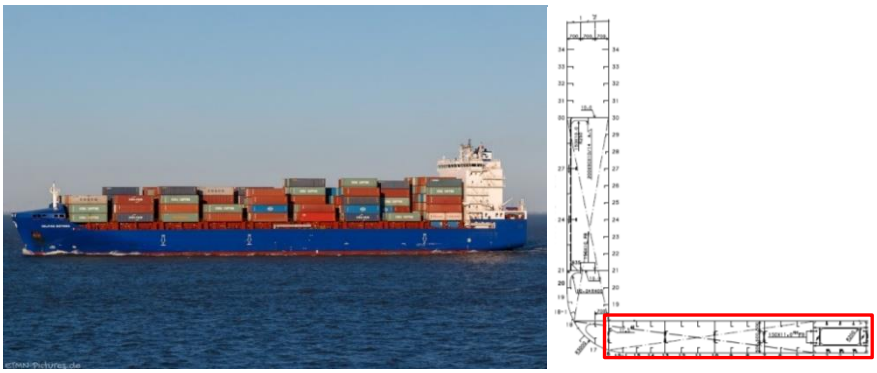

Figure 3.2 A 1,900 TEU containership built by Hanjin Heavy Industries was selected as a reference in the present thesis.

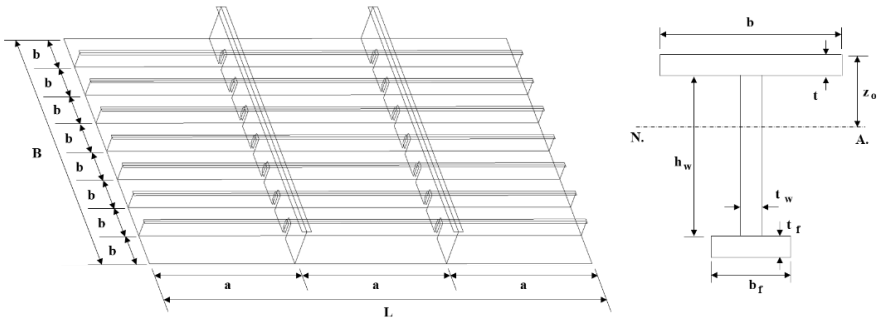

Figure 3.3 Nomenclature of the test structure.

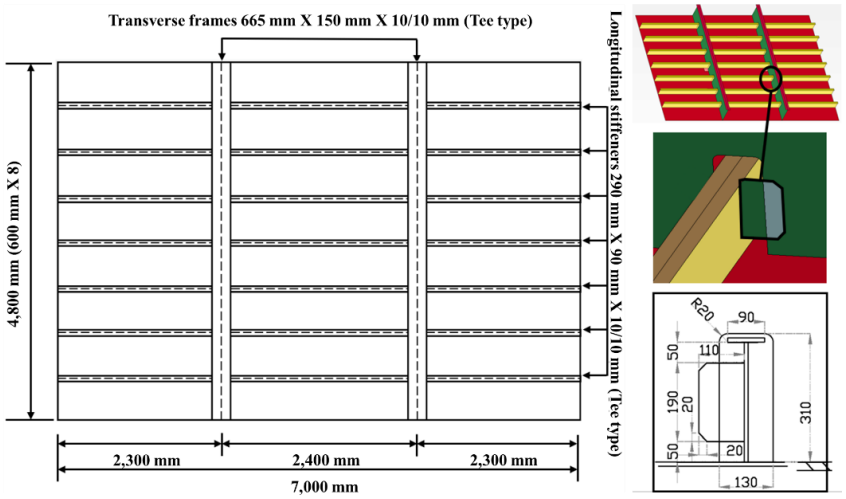

Figure 3.4 Drawing of the test structure design.

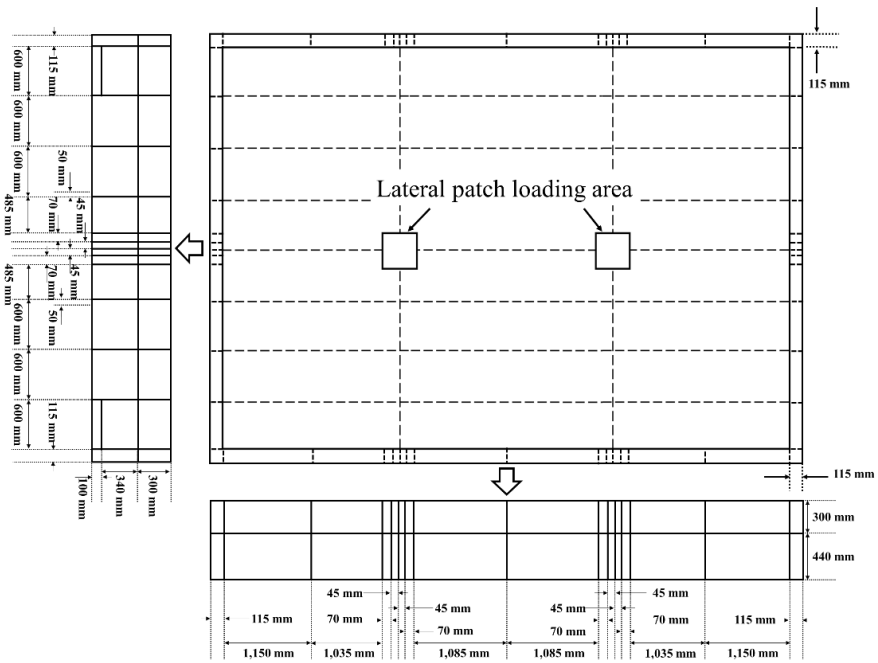

Figure 3.5 Details of the test structure together with supporting jigs along the four boundaries.

Table 3.1 Dimensions of plate panels for the reference ship structure versus the test structure.

Parameter	Reference plate panels	Test structure
Material	AH32	AH32
Length, L	9,450 mm	7,000 mm
Breadth, B	6,912 mm	4,800 mm
Spacing between transverse frames, a	3,150 mm	2,400 mm
Spacing between longitudinal stiffeners, b	864 mm	600 mm
Number of longitudinal stiffeners	7	7
Aspect ratio, a / b	3.65	4.00
Plate thickness, t	12 mm	10 mm
Plate slenderness ratio, β	2.89	2.41
Size of longitudinal stiffener	283×90×13/17 (T) (mm)	290×90×10/10 (T) (mm)
Column slenderness ratio, λ	0.38	0.28
Size of transverse frame	665×150×10/10 (T) (mm)	665×150×10/10 (T) (mm)
Number of transverse frames	2	2
Weight	9.5 ton (9.4505)	4.7 ton

3.3 Material Procurement

High tensile steel with grade AH32 is used to fabricate the test structure and support jigs. Material procurement was conducted under the responsibility of a shipyard in Busan, South Korea which fabricated the test structure as described in Section 3.4. The nominal values of mechanical properties for AH32 high tensile steel at room temperature (20 ℃) provided by the steelmaker are indicated in Table 3.2.

As the test database obtained from the present study will be used to validate computational models for structural crashworthiness analysis in fires, the actual mechanical properties of the material used for fabricating the test structure need to be identified. Furthermore, material properties significantly vary with elevated temperatures in fires as presented in Figure 2.6(a), and thus they should also be characterised. The reduction factor in Figure 2.6(a) indicates a ratio of the corresponding parameter at an elevated temperature to that at room temperature.

After the material procurement, tensile material test specimens with a round rod (bar) type were extracted from the plate sheet following ASTM specifications. ASTM International (2020), formerly known as the American Society for Testing and Materials, is an international standards organization that develops and publishes voluntary consensus technical standards for a wide range of materials, products, systems, and services. ASTM E8/E8M-16a standard was applied for room temperature (20 ℃) test and E21-17 standard was applied for elevated temperature (400 ℃, 600 ℃ and 800 ℃). To characterise the effects of elevated temperatures due to fires on the mechanical properties of the material, tensile testing was conducted with varying elevated temperatures using a universal testing machine with a temperature control chamber.

Figure 3.6 shows a tensile material test set-up at an elevated temperature using the test facility at the ICASS/KOSORI in Yangsan, South Korea (www.icass.center). Figure 3.7 presents the engineering stress-engineering strain curves of the high tensile steel AH32 obtained from the tensile testing. It is observed that neither upper nor lower yield point appears at 400 ℃ until the ultimate tensile strength is reached. In this case, the yield strength was defined as the stress at the intersection of the stress-strain curve and a straight line

through an offset point strain equivalent to the proof stress at 0.2% strain (Paik 2018). Table 3.3 summarises the obtained mechanical properties of the AH32 steel, with varying elevated temperatures associated with fires.

Figure 3.8 shows a comparison of material properties between tension tests and EN 1993-1-2 (2005), where the nominalised factor indicates a ratio of the corresponding parameter at an elevated temperature to that at room temperature. It is confirmed from Figure 3.8 that the EN 1993-1-2 curve generally provides a reasonable guideline to characterise the effects of elevated temperatures on mechanical properties of steel as it is in good agreement with tension tests. New data for ultimate tensile strength and elongation obtained from the present study are also presented. The reduction trend of ultimate tensile strength is quite similar to that of yield strength, but the elongation significantly increases with increase in temperature.

Table 3.2 Nominal properties of AH32 high tensile steel at room temperature (20 ℃), provided by steelmaker.

Elastic modulus, E (GPa)	Yield strength, σ_Y (MPa)	Ultimate tensile strength, σ_T (MPa)	Fracture strain (elongation), ε_f
200	≥ 315	440-570	≥ 0.22

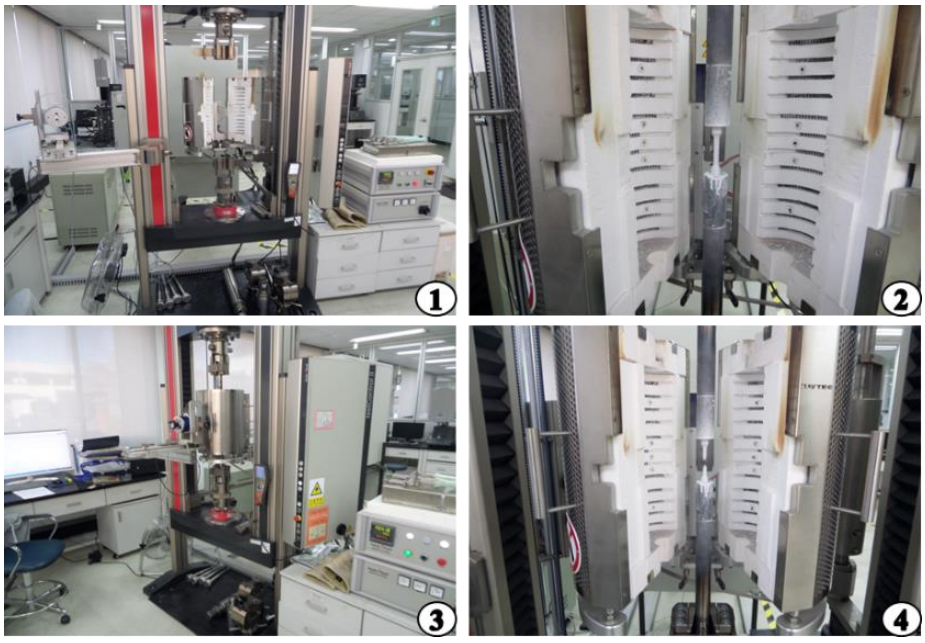

Figure 3.6 Tensile material test set-up using a universal testing machine with an elevated temperature control chamber.

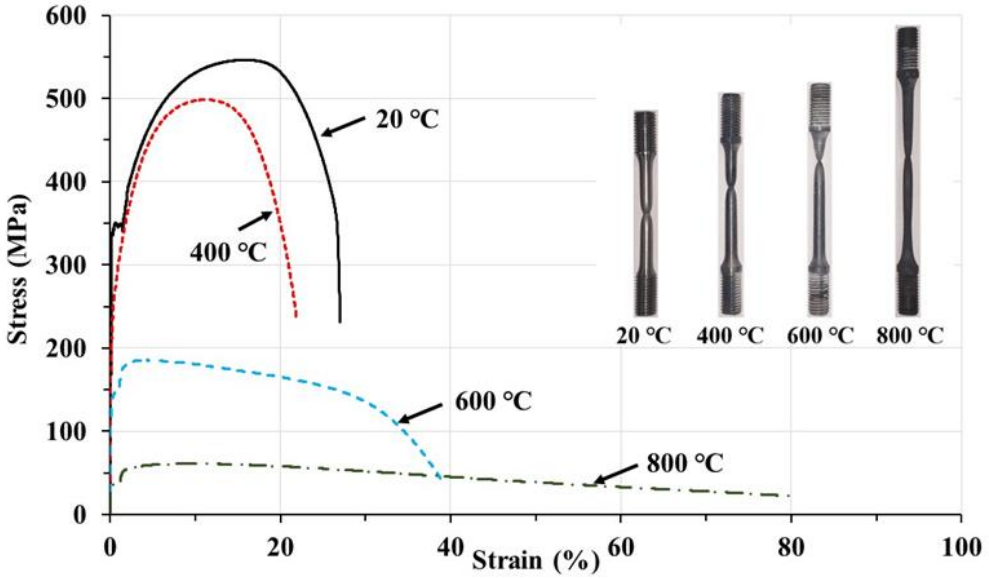

Figure 3.7 Engineering stress-engineering strain curves of high tensile steel AH32 at different temperatures, obtained from tensile tests.

Table 3.3 Mechanical properties of high tensile steel AH32 at different temperatures.

Temperature	20 ℃	400 ℃	600 ℃	800 ℃
Elastic modulus, E (GPa)	224.0	153.80	94.0	31.70
Yield strength, σ_Y (MPa)	340.0	320.71	140.80	34.60
Ultimate tensile strength, σ_T (MPa)	546.20	498.60	185.50	61.20
Fracture strain (elongation), ε_f	0.30	0.37	0.61	1.08

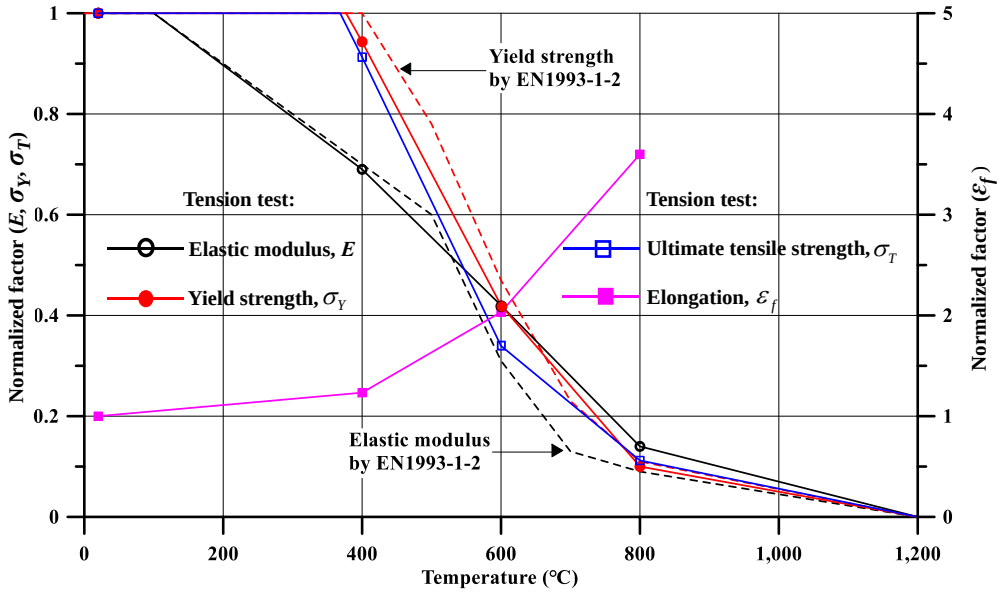

Figure 3.8 Comparison of material properties between tension tests and EN 1993-1-2 for AH32 high tensile steel.

3.4 Fabrication of the Test Structure

The test structure was fabricated at a shipyard in Busan, South Korea using the same welding technology as used in today's shipbuilding industry. The shipyard has built small and medium-sized merchant and patrol ships. It is an intention that the test structure is built at a shipyard to attain the same conditions of flaming cutting and welding as for real ship structures.

Table 3.4 Welding conditions applied for the fabrication of the test structure.

Method	FCAW
Flux-cored wire	CSF-71S
Leg length	7 mm
Current	260 A (225~275 A)
Voltage	28 V (23~32 V)
Welding speed	30 cm/min (24~34 cm/min)
Heat input	14.56 KJ/cm (7~18 KJ/cm)

Note: The value in the parenthesis indicates the welding procedure specification requirements.

Table 3.4 summarises the welding conditions applied for fabricating the test structure. To minimise welding-induced initial imperfections, the plating of the test structure was entirely made of an identical steel sheet by avoiding butt welds to connect pieces of steel sheets. All longitudinal stiffeners and transverse frames were attached by continuous fillet welding where the welding requirements of DNV (2018) were satisfied. The flux-cored arc welding (FCAW) method was applied in compliance with the welding procedure specification requirements as indicated in Table 3.4. Figure 3.9 shows photos representing a flow of the fabrication process. Support jigs along four boundaries were fabricated as shown in Figure 3.10. The test structure was transported using a truck trailer on a highway from the shipyard to the test site at ICASS/KOSORI (www.icass.center) in Hadong, South Korea.

During the process of welding fabrication, initial imperfections are inevitably developed in the form of initial deflections and residual stresses which can significantly affect the ultimate strength under predominantly axial compressive loading (Paik 2018). However, the test structure under consideration in the present study is subjected to lateral patch loading at elevated temperature, and the effects of initial imperfections on the structural crashworthiness in fires are considered to be very small. Referring to articles (Paik et al. 2020; Paik et al. 2021a, 2021b; Ryu et al. 2021; Yi et al. 2019, 2020, 2021) which are associated with the present study. In this regard, the welding-induced initial imperfections were not measured.

The test set-up was built to achieve fixed boundary conditions along the four edges of the test models (as mentioned in Section 3.2 Design of the Test Structure) – this means that computational models can be developed so that the boundary of the test models can be set to be fixed conditions. For this purpose, strong steel support jigs or frames were attached as shown in Figure 3.10. Furthermore, the support jigs were protected by PFP materials so that they should be kept intact during fire testing as for the fixed boundary conditions designated beforehand. During the testing, it was confirmed that the support jigs remained intact until the test structures collapsed, but at the final stage of the testing, some small cracks occurred at the welded sections between support jigs and the framework of the furnace and subsequently, the

gas cloud temperatures were not raised fully (as described in Section 3.9.1 Ambient and Gas Cloud Temperatures).

(a)

(b)

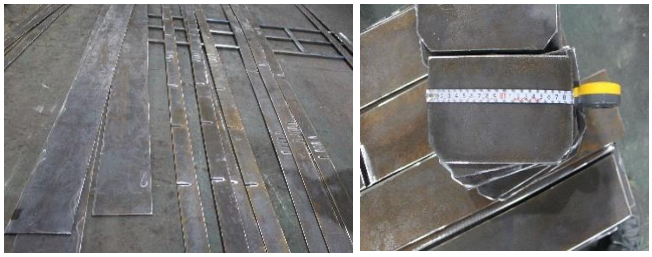

(c)

(d)

Figure 3.9 Photos representing a flow of the fabrication process at the shipyard: (a) raw plate sheet, (b) plate cutting, (c) assembly of support members and support jigs, (d) completion of the test structure.

Figure 3.10 Fabrication of support jigs along four boundaries of the test structure.

3.5 Test Set-Up

The testing was conducted in a horizontal type furnace at the test site of the ICASS/KOSORI in Hadong, South Korea (www.icass.center). Figure 3.11 shows the horizontal type fire furnace test facility used for the testing. The space inside the furnace is 6,500 mm long, 4,500 mm wide and 1,730 mm deep. The test structure is positioned horizontally to cover up the top of the furnace, while burners supplied by liquefied petroleum gases are used to raise the ambient temperature inside the furnace. The maximum gas cloud temperature that can be applied in the test facility is 1,430 ℃. Figure 3.12 shows a target curve of increasing gas cloud temperatures with time as per the ISO 834 fire curve (ISO 834 1999) which presents a guideline for predicting time-variant ambient temperatures for engineering structures in fires. It can be expressed in the following equation:

$$T = 20 + 345\log\left(8t + 1\right), \tag{3.3}$$

where T is the gas cloud temperature in ℃ and t is the time in min. Figure 3.12 also shows the ISO 834 curve 15% below the original curve, which was applied for the present test.

The test structure was set up as a top cover of the furnace where the side of support members such as transverse frames and longitudinal stiffeners was located inside the furnace. The support jigs of the test structure were welded with the framework of the furnace to prevent the whole test structure from moving in the horizontal direction, at a total of 12 locations as shown in Figure 3.13 where a 300 mm long welding of a supporting jig was applied along part of the furnace boundary as shown in Figure 3.14. For nonlinear finite element modelling of the structural framework, a fixed boundary condition may be approximately applicable.

The boundaries of the furnace should be fully shielded to prevent elevated temperatures inside the furnace from flowing outside the test structure, and thus all the four boundaries were insulated by fire protection material, called

cerawool. By decreasing heat conductivity with melted and fiberized high purity silica (sand) and alumina, cerawool may produce an ultra-high temperature-resistant and fireproof state. Table 3.5 and Figure 3.15 present the properties of cerawool (DIFK 2014). The Appendix A.3 provides the thermal conductivity of cerawool as shown in Figure 3.15. Figure 3.16 shows the insulation with fire protection material along the four boundaries of the test structure for the fire test without PFP.

For the test with PFP, application on the fire collapse of steel stiffened plate structures, passive fire protection using cerawool was applied to two transverse frames and support jigs of the test structure. A specialist company was hired for this work. Figure 3.17 shows the test structure after the passive fire protection installation was completed. Figure 3.18 shows the completion of the test set-up including loading and sensors of test data acquisition that will be described later.

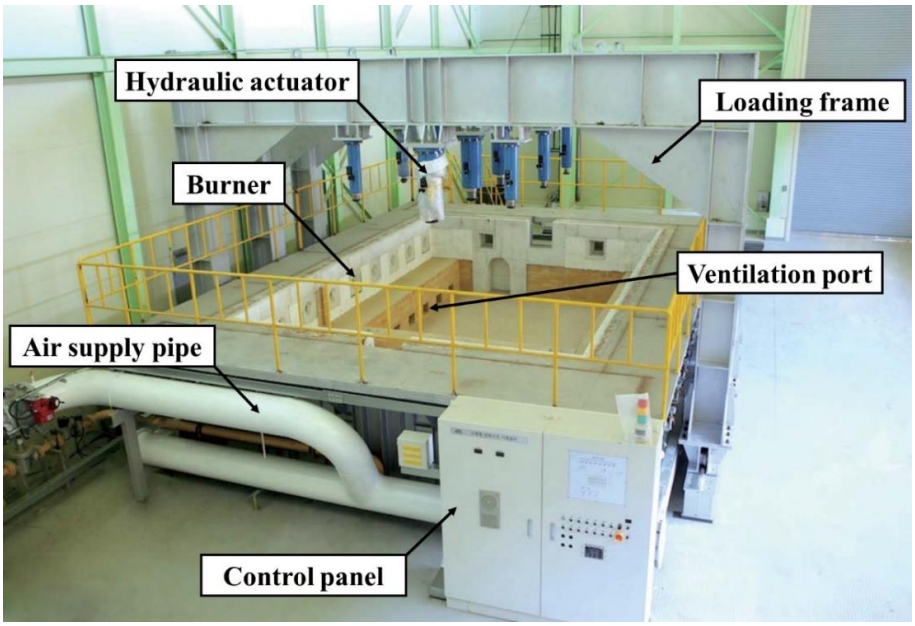

Figure 3.11 Horizontal type fire test furnace facility of the ICASS/KOSORI in Hadong, South Korea.

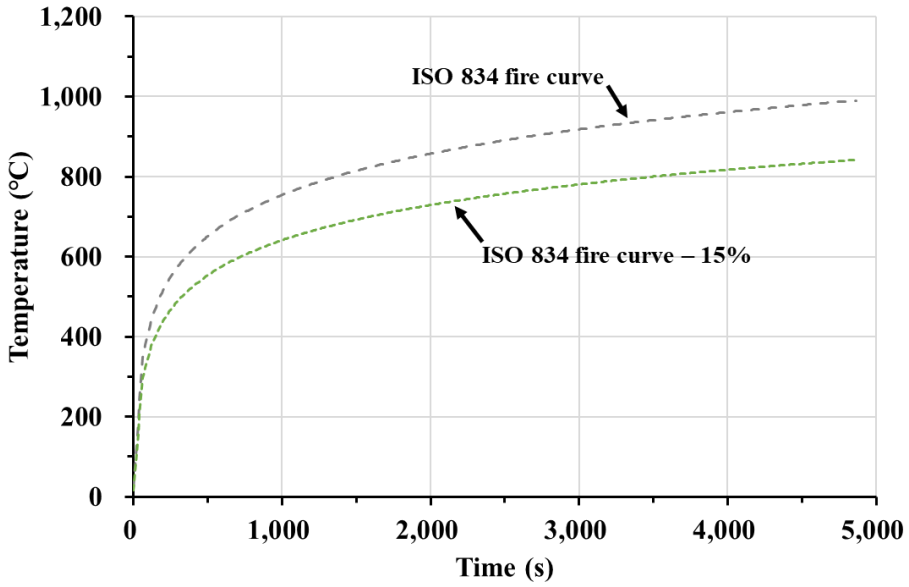

Figure 3.12 A target curve of increasing temperatures with time as per the ISO 834 fire curve.

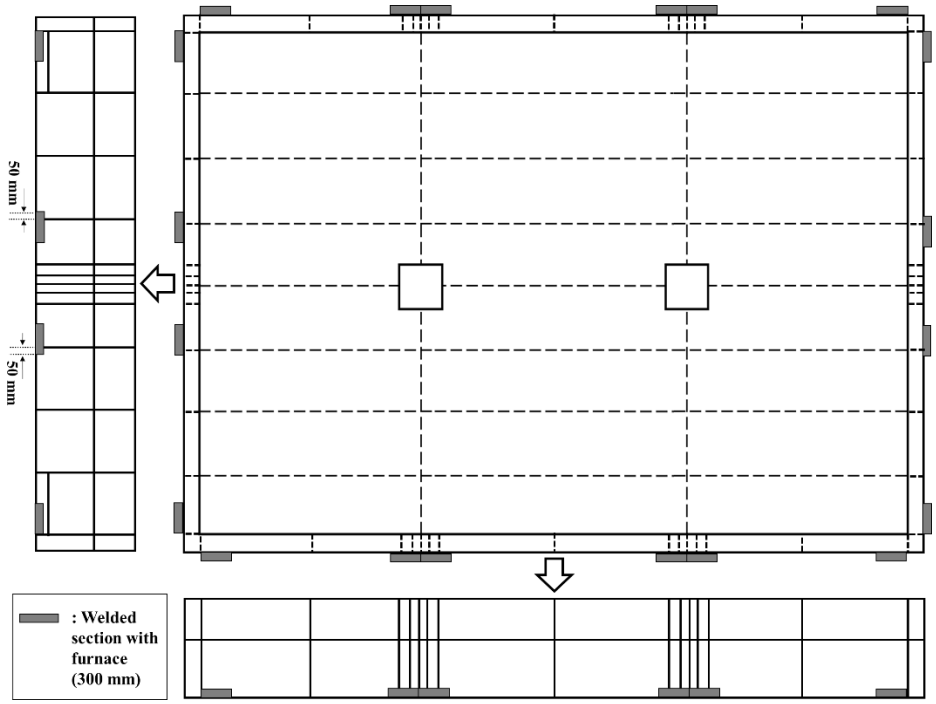

Figure 3.13 Welded locations between supporting jigs and the furnace.

Figure 3.14 A 300 mm long welding of a supporting jig along part of the furnace boundary.

Table 3.5 Material properties of cerawool.

Thickness	Tensile strength	Density	Maximum service temperature	Specific heat
50 mm	0.750 MPa	0.128 ton/m^3	1,200 ℃	2,550 J/Kg ℃

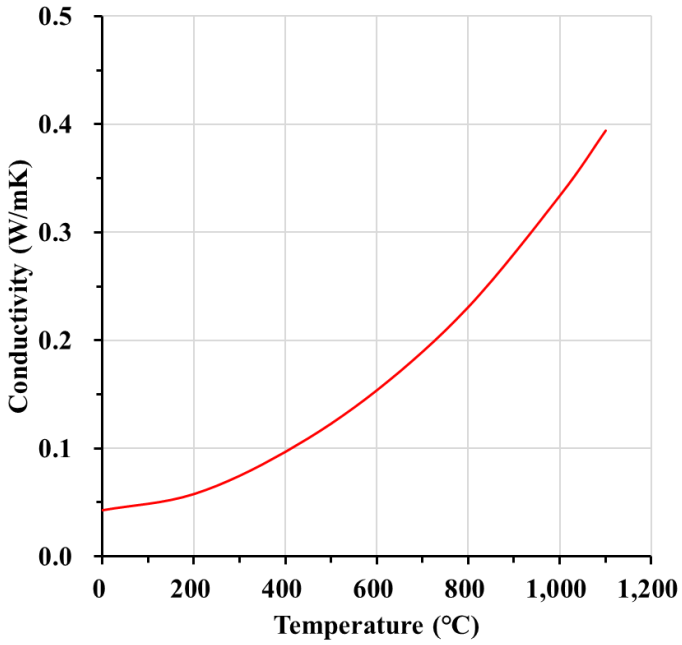

Figure 3.15 Thermal conductivity of cerawool.

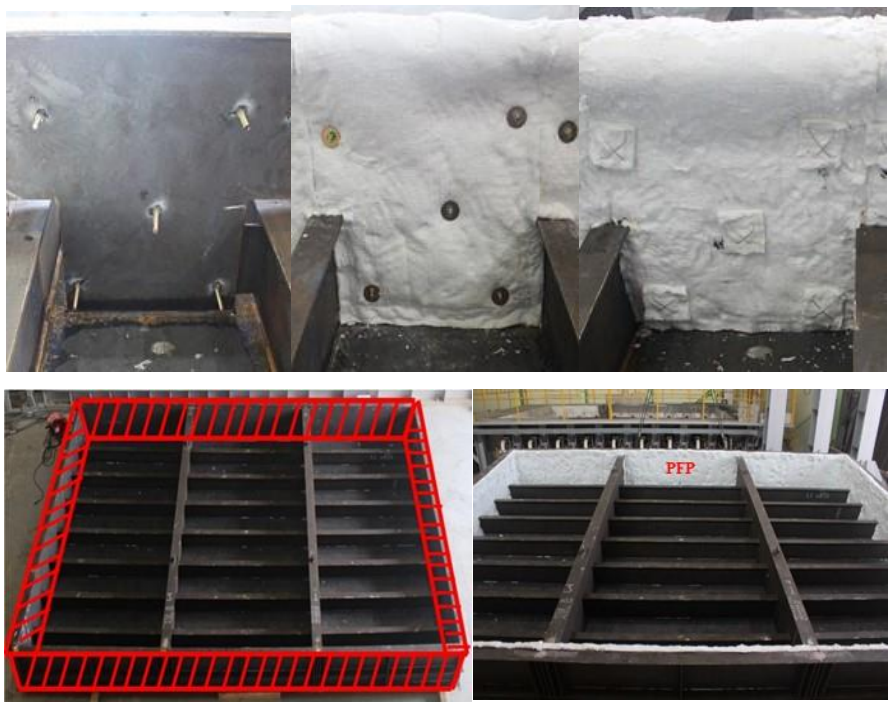

Figure 3.16 Insulation with passive fire protection material along the four boundaries of the test structure for the fire test without PFP.

Figure 3.17 Insulation with passive fire protection material along the four boundaries and two transverse frames of the test structure for the fire test with PFP.

Figure 3.18 Test set-up at the test site.

3.6 Lateral Patch Loading

A set of three hydraulic loading actuators are available to apply external forces up to 3 MN. The test program associated with temperature and external loading is monitored and controlled by a computer system in the control room which is located at an elevation to view an overall test scene away from the furnace. Physical databases such as loads and temperatures (gas cloud and steel) are recorded at an interval of several seconds (e.g., 10 s) during testing by a personal computer in the control room.

Two out of three hydraulic loading actuators were used for the present test where lateral patch loads were applied at the centre of each transverse frame as shown in Figure 3.19. Multiple layered steel plates including one plate insulated with passive fire protection were inserted between the loading actuator tip and the patch area of the test structure, as shown in Figure 3.20 and Figure 3.21, to apply the patch loads uniformly over the patch area and also to protect loading actuators from heat. To prevent the transfer of high temperature from the heated test structure to the loading actuators, which may cause a malfunction, they were insulated by fire protection material with cerawool as shown in Figure 3.22.

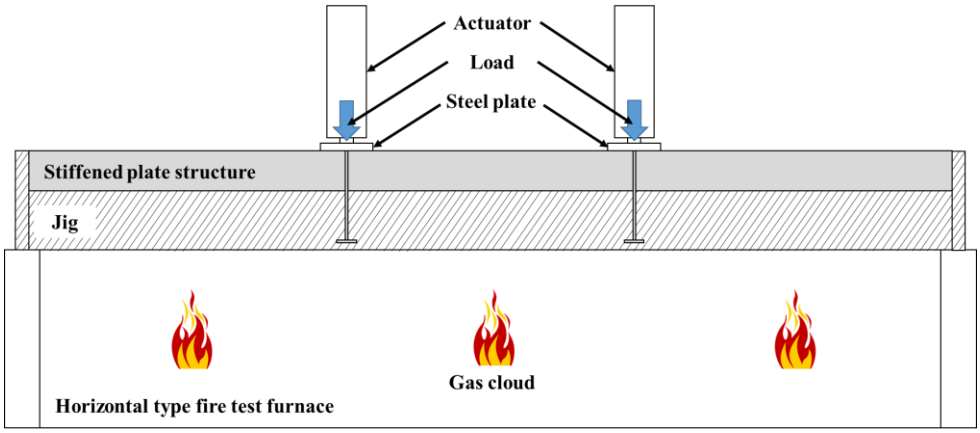

Figure 3.19 Set-up for applying lateral patch loads at the centre of transverse frames.

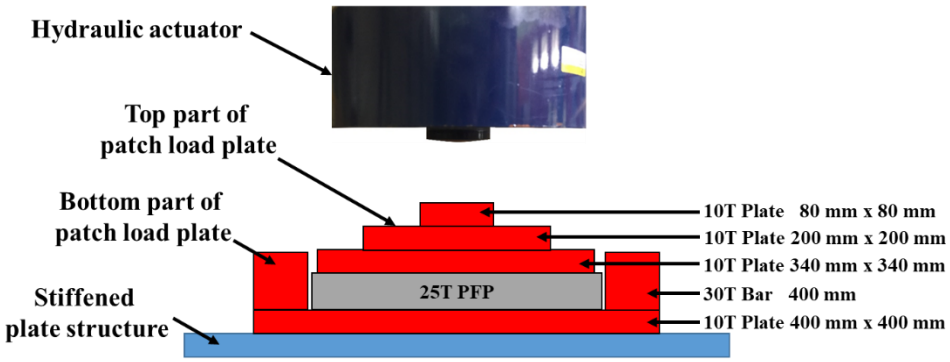

Figure 3.20 Multiple layered steel plates between the loading actuator and the patch loading area (side view).

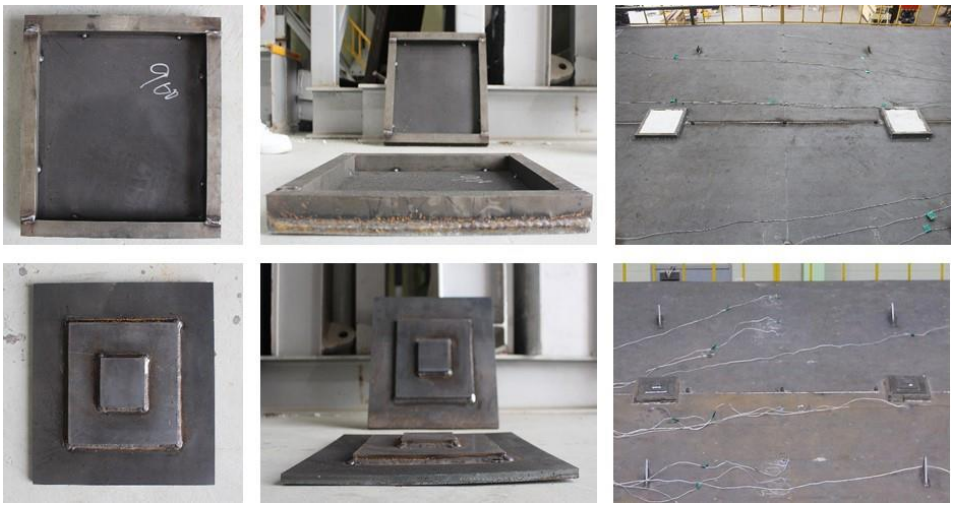

Figure 3.21 Manufactured and installed patch load plates.

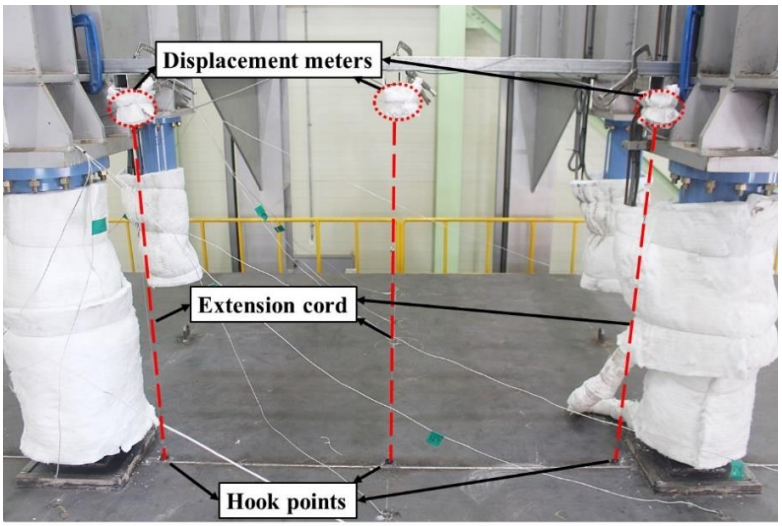

Figure 3.22 Insulation of passive fire protection for loading actuators to prevent them from heat transfer.

3.6.1 Fire Test Without PFP

Lateral patch loads were applied at two steps as shown in Figure 3.23, where 15 tf (ton-force) were applied at each loading point and maintained for 1,580 s in the first step, and 50 tf were applied at each loading point after fully unloading the first load step at 1,630 s and maintained until the test ended by structural collapse at 2,630 s. At each loading step, the magnitude of load application was kept constant, where the stroke of the hydraulic loading actuator was automatically controlled so that the applied loading was considered as a “dead load”. A computer system in the control room was used for this purpose.

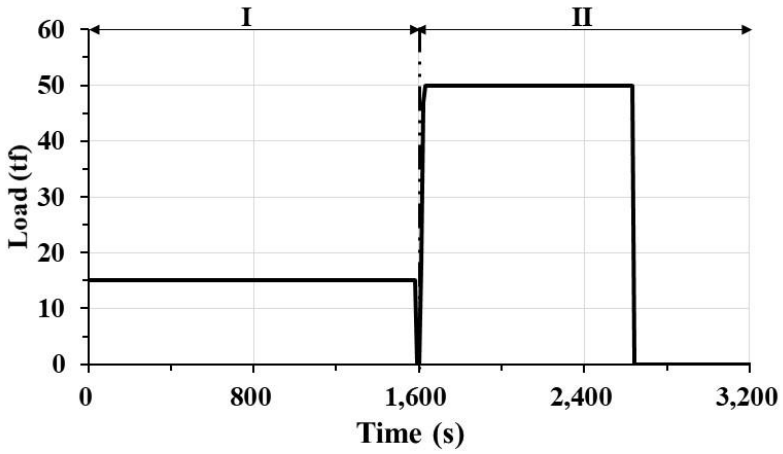

Figure 3.23 Application of lateral patch loads at two steps for the fire test without PFP.

3.6.2 Fire Test With PFP

Lateral loading was applied at three stages with 15 tf (ton-force) at each loading point during 0 to 1,591 s, 50 tf at each loading point during 1,601 to 3,091 s and 75 tf at each loading point after 3,101 s on each patch area, as shown in Figure 3.24.

On the other hand, the test without passive fire protection in transverse frames was conducted with lateral patch loading similarly but at two stages as compared with a dotted line in Figure 3.24. It is noted that the first two load steps are identical to the earlier test without fire protection. It is intended that the structural crashworthiness associated with the first two load steps is compared in terms of transverse frames unprotected versus protected by anti-fire material. The database of applied lateral patch loads for two fire tests is provided in Appendix A.4.

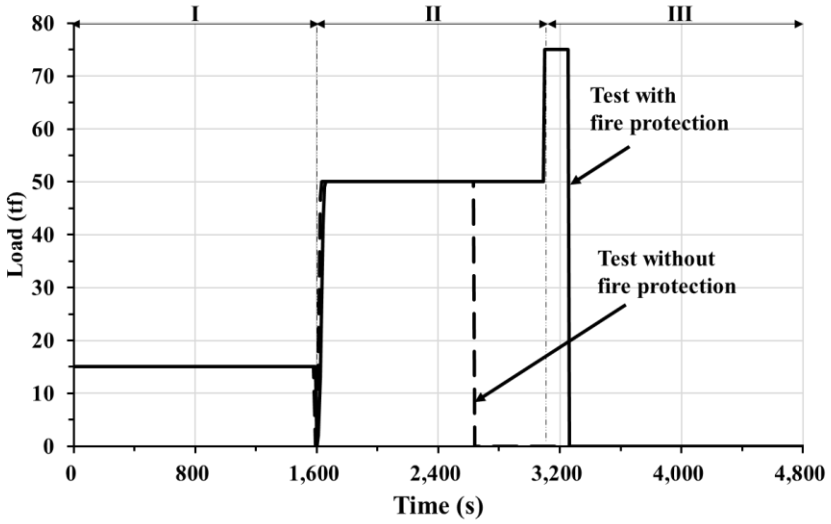

Figure 3.24 Application of lateral patch loads at three steps for the fire test with PFP.

3.7 Test Data Acquisitions

3.7.1 Gas Cloud Temperatures

Gas cloud temperatures inside the furnace were measured with time using thermo-electric couple sensors wired to the personal computer in the control room. A total of 14 points inside the furnace as shown in Figure 3.25 were

monitored to measure gas cloud temperatures. The sensors were positioned 300 mm below the test structure with two arrays on each side.

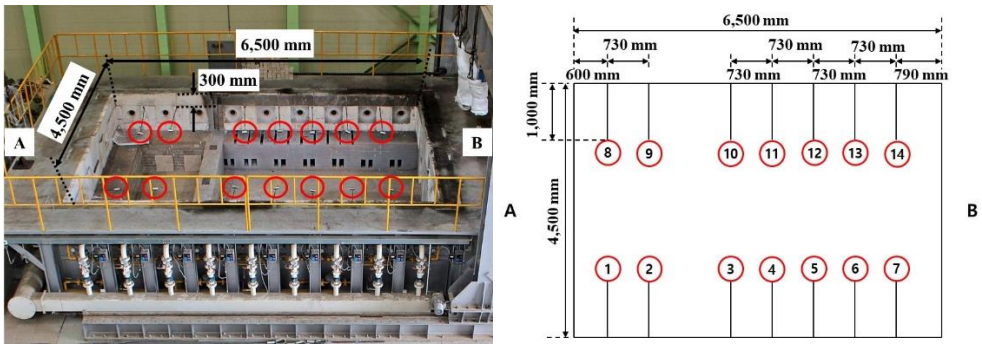

Figure 3.25 A total of 14 monitoring points to measure gas cloud temperatures inside the furnace.

3.7.2 Steel Temperatures

Gas cloud temperatures are transferred to steel, and steel temperatures of the test structure are measured at a total of 14 points (Nos. 1-13 and 21) using thermo-electric couple sensors. Also, a total of 7 locations (Nos. 14-20) were monitored to measure steel temperatures of supporting jigs insulated by fire protection materials, which can be used to assess their support effectiveness against fires. The sensors Nos. 1-20 were allocated to measure steel temperatures at the plating of the test structure outside the furnace. On the other hand, one sensor (No. 21) was used to measure the steel temperatures of the test structure inside the furnace. Figure 3.26 shows the locations of the monitoring points to measure steel temperatures. The thermos-electric sensors were attached by spot welding, as shown in Figure 3.27.

To attach sensors No. 21 and 22 for measuring steel temperatures inside the furnace, a hole with a diameter of 6 mm was made at the centre of the test structure to pass a wire through. Two dummy steel plates with a size of 200 mm × 290 mm were attached to the test structure inside the furnace, and they were placed in overlap with a thickness of 5 mm together with a ceramic tube with a diameter of 4 mm which is enough to pass the insulated wire of the sensor through. Figure 3.28 shows the design of the dummy steel plates, and Figure 3.29 shows the installation of the sensor into the dummy steel plates.

In addition, for the fire test with PFP, with sensor No. 21 unprotected for heat, another sensor No. 22 was allocated to make a comparison between steel temperatures of the transverse frame with and without fire protection. Figure 3.30 shows sensor No. 22 with fire protection using cerawool.

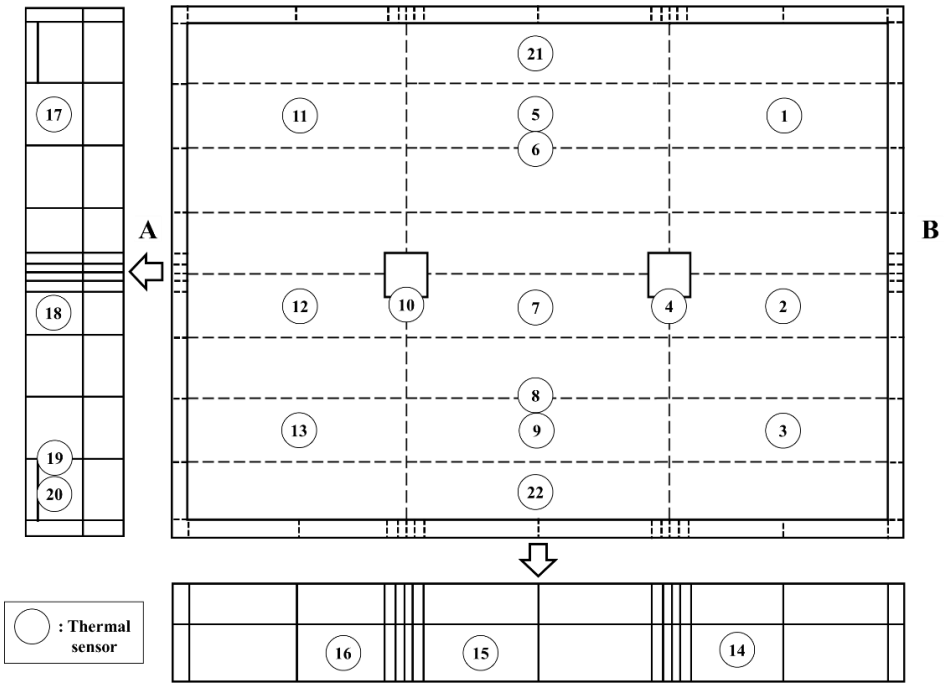

Figure 3.26 Monitoring points to measure steel temperatures (top view).

Figure 3.27 Spot welding to attach thermo-electric couple sensors.

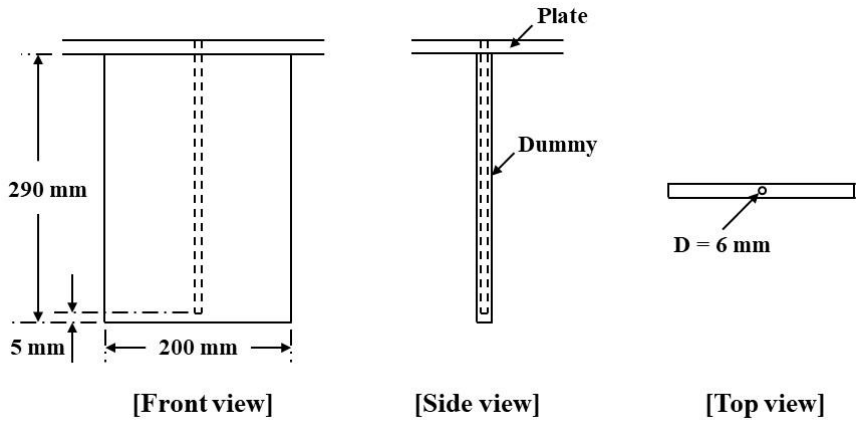

Figure 3.28 Design of the dummy steel plates.

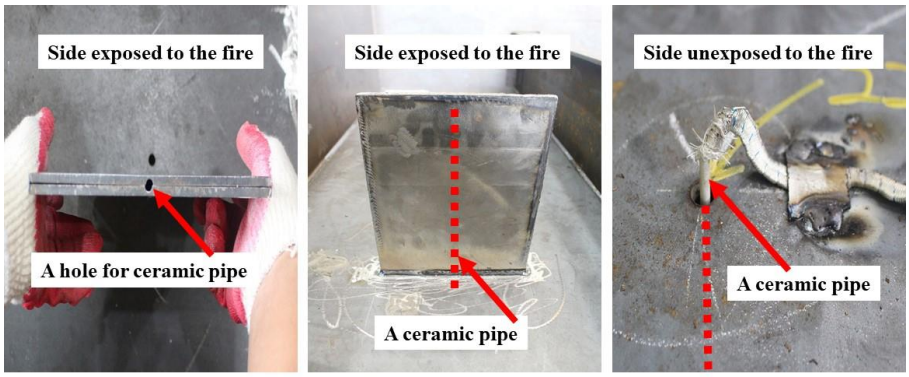

Figure 3.29 Installation of the sensor (No. 21 and 22) into the dummy steel plates.

Figure 3.30 The sensor No.22 with fire protection using cerawool.

3.7.3 Lateral Deflections

Lateral patch loading was automatically controlled by the personal computer in the control room as a dead load after increasing up to the target value. This implies that the stroke of the loading actuator needed to alter for

keeping the same loads despite the increase of lateral deformation. Also, the controller worked to secure the synchronizing of the two loading at the same patch loads.

Lateral deformation continued to occur with time at elevated temperatures even if the applied loads were kept unchanged. Lateral deformations were measured at a total of three points using displacement meters. Because of the loading actuators, the displacement meters were placed 300 mm away from the centre of the patch loading points, as shown in Figure 3.31, while the last displacement meter was positioned on exactly the central point of the test structure. Figure 3.22 shows the set-up of displacement meters at the three monitoring points.

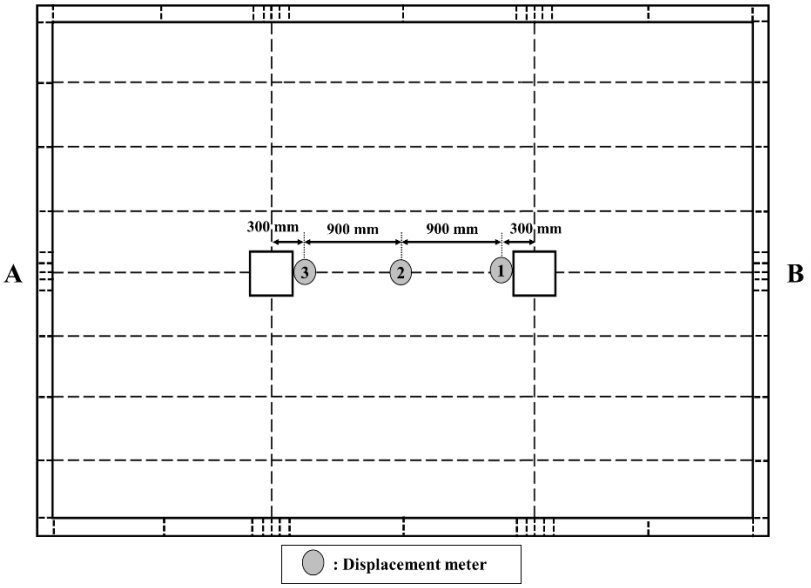

Figure 3.31 Locations of displacement meters.

3.8 Test Results and Discussion for the Fire Test Without PFP

3.8.1 Ambient and Gas Cloud Temperatures

Figure 3.32 presents the change of ambient temperatures around the test structure outside the furnace. The room temperature was 27.6 °C before heating, and it was increased to 30.6 °C after an hour, implying that the room temperature was almost constant.

Figure 3.33 presents gas cloud temperatures measured at monitoring points inside the furnace. The gas cloud temperature on average reached 600 ℃ at

180 s after the start of gas burning, and it remained at 700 - 800 ℃ after 1,450 s until the structure collapsed. From 2,720 s after the collapse of the structure, the temperature was drastically decreased as the gas burner was shut down.

Monitoring points 1, 7, 8 and 14 were located away from the centre of the test structure, and the gas cloud temperatures at these locations are slightly lower than other points close to the centre. However, it is said that the gas cloud temperatures are almost uniform inside the furnace. Figure 3.34 compares the gas cloud temperatures between the measurements and the ISO 834 fire curve. It is seen from Figure 3.34 that the average gas cloud temperature is equivalent to 15% lower than the ISO 834 fire curve.

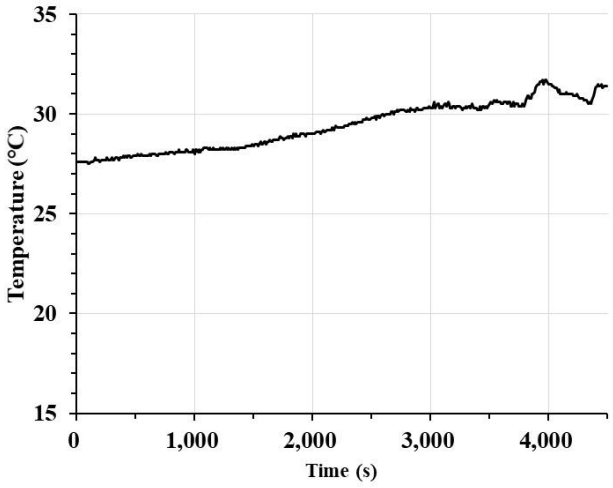

Figure 3.32 Ambient temperature outside the furnace around the test structure for the fire test without PFP.

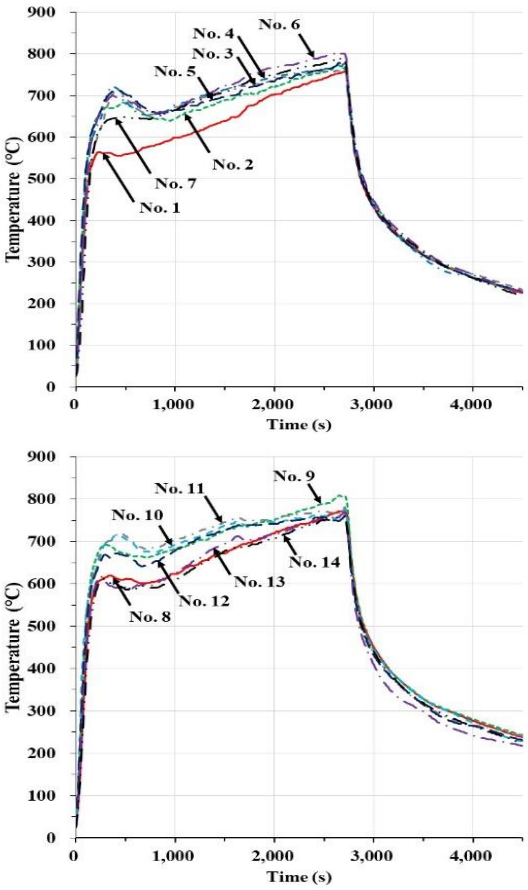

Figure 3.33 Gas cloud temperatures at monitoring points inside the furnace for the fire test without PFP.

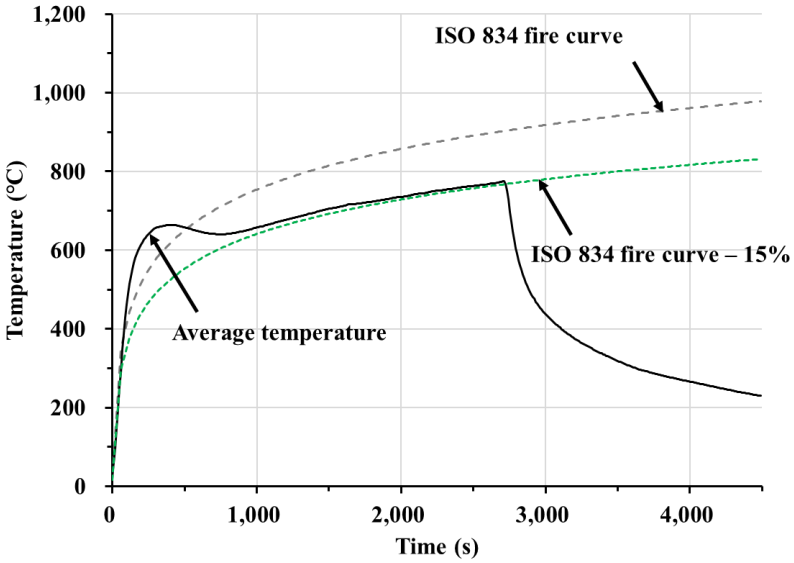

Figure 3.34 Comparison of gas cloud temperatures with the ISO 834 fire curve for the fire test without PFP.

3.8.2 Steel Temperatures

Gas cloud temperatures are transferred to steel structures. Figure 3.35(a)-(c) present steel temperatures measured at a total of 14 monitoring points of the test structure. Comparing steel temperatures in Figure 3.35 and gas cloud temperatures in Figure 3.33 reveals that the former is of course lower than the latter. Steel temperatures measured for supporting jigs are shown in Figure 3.35(d), showing that the maximum temperature is at most 94 ℃. This confirmed that the fire protection material almost fully insulated the supporting jigs and the fixed conditions along the boundaries of the test structure were secured.

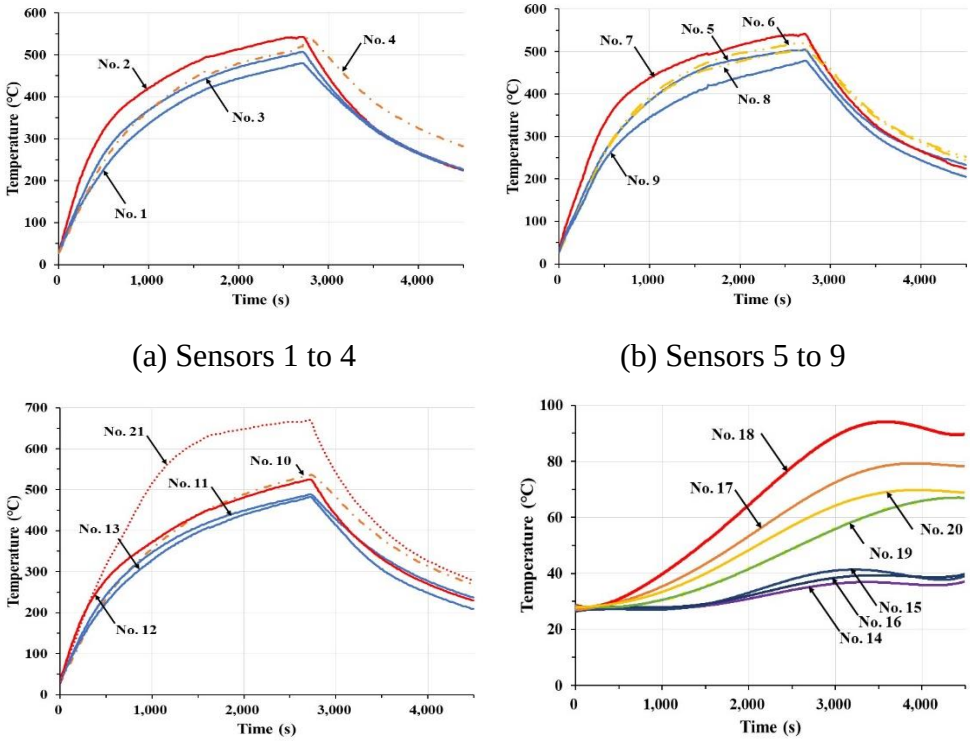

(a) Sensors 1 to 4 (b) Sensors 5 to 9

(c) Sensors 10 to 13 and 21 (d) Sensors 14 to 20

Figure 3.35 Steel temperatures measured at monitoring points for the fire test without PFP.

3.8.3 Structural Crashworthiness

The crashworthiness of the test structure was monitored in association with gas cloud temperatures and lateral deformation. Figure 3.36 presents the lateral deformations at three monitoring points where channel 1 and channel 3 indicate displacement sensors close to the locations of patch loading and

channel 2 is the sensor at the centre of the test structure. Until 1,600 s, almost no lateral deformations occurred under a patch load of 15 tf.

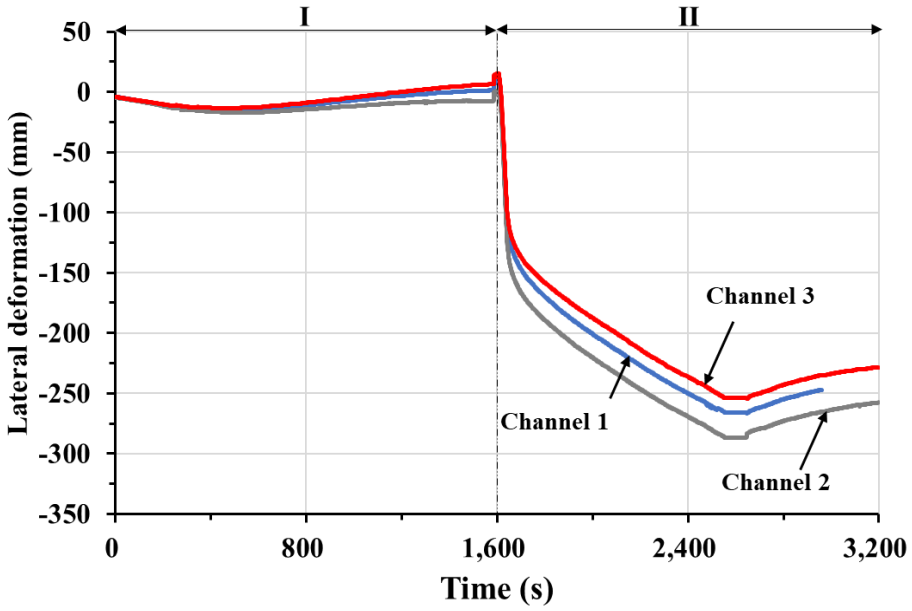

Figure 3.36 Load-lateral deformation curves of the test structure at the three monitoring points for the fire test without PFP.

The lateral deformations started to dramatically increase at 1,630 s when a load of 50 tf was applied at the second load step. The lateral deformations were released at 2,550 s when the applied loads were removed. As far as the present schemes of loading and gas cloud temperatures are considered, the critical period until the test structure reaches the entire collapse is 1,600 s.

The Appendix A.8 provides the lateral deformation versus time history data which can be used to validate computational models for the crashworthiness analysis of the test structure in fires. Figure 3.37 shows deformed shapes of the test structure after testing. It is observed that transverse frames as the main support member deformed significantly, and this triggered the entire collapse of the test structure.

Figure 3.37 Deformed shapes of the test structure for the fire test without PFP.

3.9 Test Results and Discussion for the Fire Test With PFP

3.9.1 Ambient and Gas Cloud Temperatures

For the ambient temperature of the fire test with PFP, as shown in Figure 3.38, although it increased slightly from the beginning with the progress of the test, room temperature at the beginning was 17.6 ℃ and rose to 22.6 ℃ after the test was ended.

Gas cloud temperatures measured at monitoring points inside the furnace are presented in Figure 3.39, where the maximum temperature was reached up to 900 ℃. The distribution of gas cloud temperature is not uniform or identical inside the furnace. Except for monitoring points 1, 2, 8 and 9, however, the temperatures are found to be similar. After the completion of testing, the reason why the temperatures at monitoring points 1, 2, 8 and 9 were comparatively low was investigated. It was found that small cracks occurred at the welded sections between support jigs and the framework of the furnace. The small cracks at these sections were owing to the weak welding points with the increase in the lateral patch loads. Cracks around the monitoring points caused heated gases inside the furnace to leak, and subsequently, the gas cloud temperatures were not raised fully. For those who

use the present test results for their computational modelling, this happening can be considered.

Figure 3.40 presents a comparison of gas cloud temperatures with the ISO 834 fire curve. It is seen that the average values of measurements in the present test are some 15% lower than the ISO 834 standard fire curve.

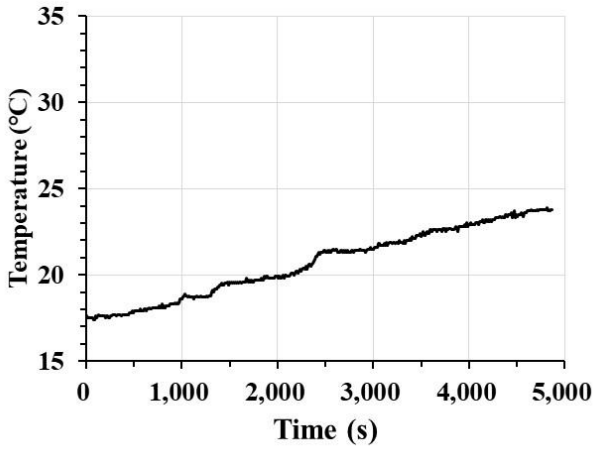

Figure 3.38 Ambient temperature outside the furnace around the test structure for the fire test with PFP.

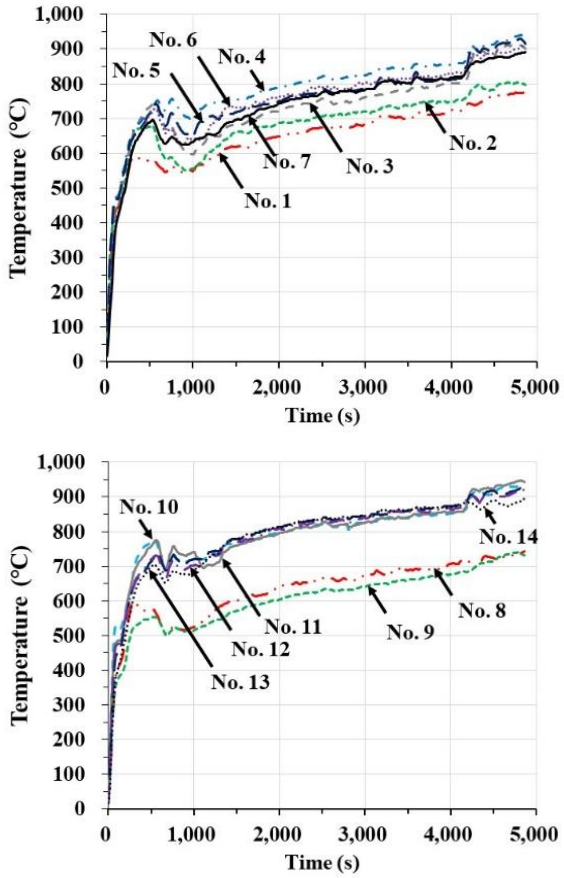

Figure 3.39 Gas cloud temperatures at monitoring points inside the furnace for the fire test with PFP.

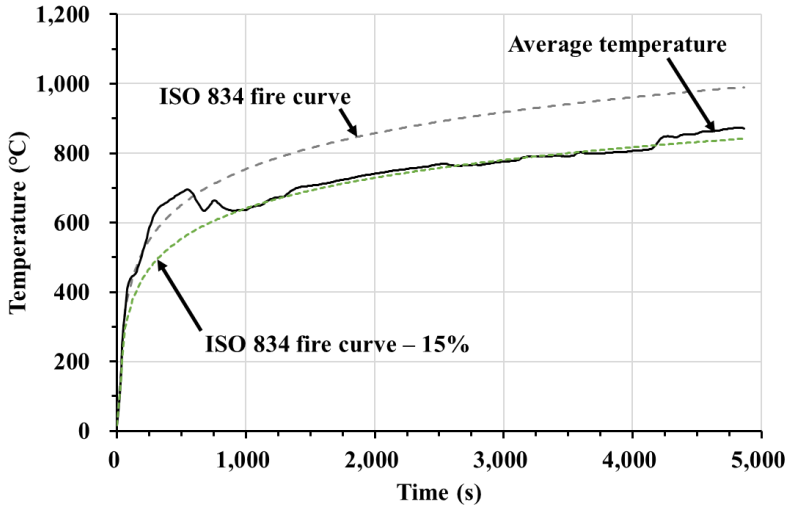

Figure 3.40 Comparison of gas cloud temperatures with the ISO 834 fire curve for the fire test with PFP.

3.9.2 Steel Temperatures

Measurements of steel temperatures at monitoring points are presented in Figure 3.41. Initially, steel temperatures of support jigs with numbers 14 – 20 were less than 100 ℃, as shown in Figure 3.41(d), confirming that the fire protection with cerawool was successful.

Steel temperatures at fire-protected transverse-frames were much lower than other unprotected locations although they also progressively increased with time, as shown in Figure 3.41(a) and Figure 3.41(c). Steel temperature at monitoring point No. 21 which was located inside the furnace was much higher than other monitoring points. This means that steel temperature between inside and outside the furnace is different from each other, implying that the plate side exposed to fires may be more vulnerable than the other side. This is obviously due to the heat transfer mechanism associated with conduction, convection, and radiation (Paik 2020). On the other hand, steel temperature at monitoring point No. 22 with fire protection is much lower than other unprotected locations, as shown in Figure 3.41(c).

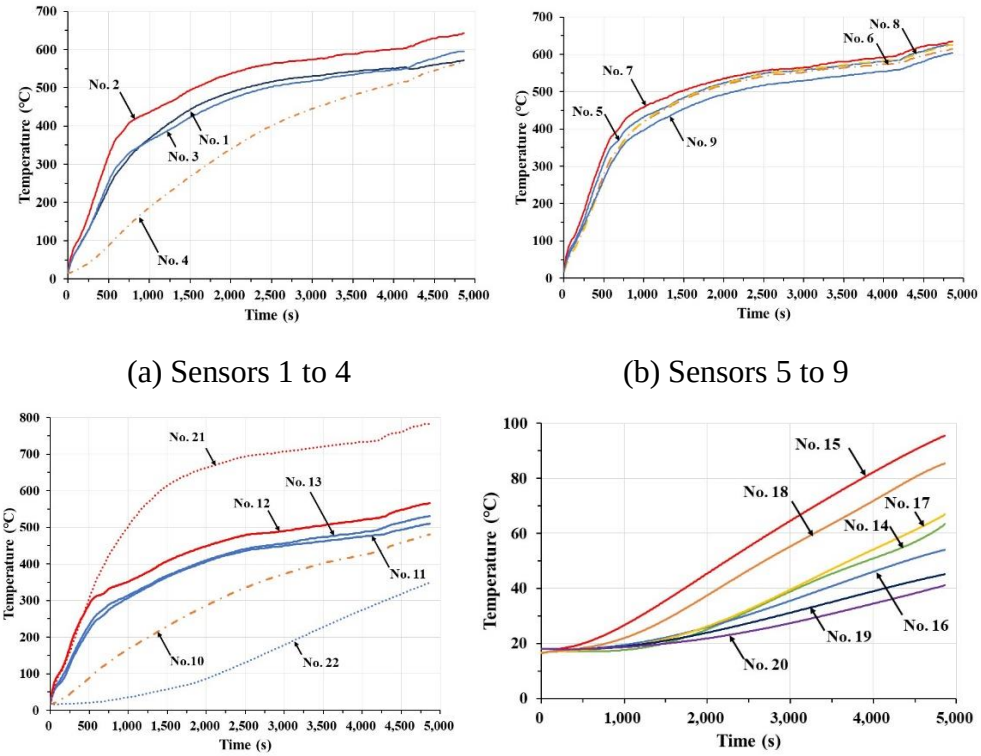

(a) Sensors 1 to 4 (b) Sensors 5 to 9

(c) Sensors 10 to 13 and 21 to 22 (d) Sensors 14 to 20

Figure 3.41 Steel temperatures measured at monitoring points for the fire test with PFP.

3.9.3 Structural Crashworthiness

Lateral patch loading was applied at three phases. Figure 3.42 shows the lateral deformation-time history, where the test data for the test structure without fire protection is compared. The test structure collapsed at 3,101 s at load step 3 when 75 tf was applied.

It is confirmed that passive fire protection is an efficient option to delay structural collapse. Together with complex patterns of failure as shown in Figure 3.43, it is seen that the structure reached the ultimate limit states triggered by the collapse of transverse frames as well as longitudinal stiffeners, which were primary strength members of the structure.

The Appendix A.9 provides the time history of lateral deformations at the three monitoring points obtained from the test with PFP as shown in Figure 3.42 which can be used to validate computational models.

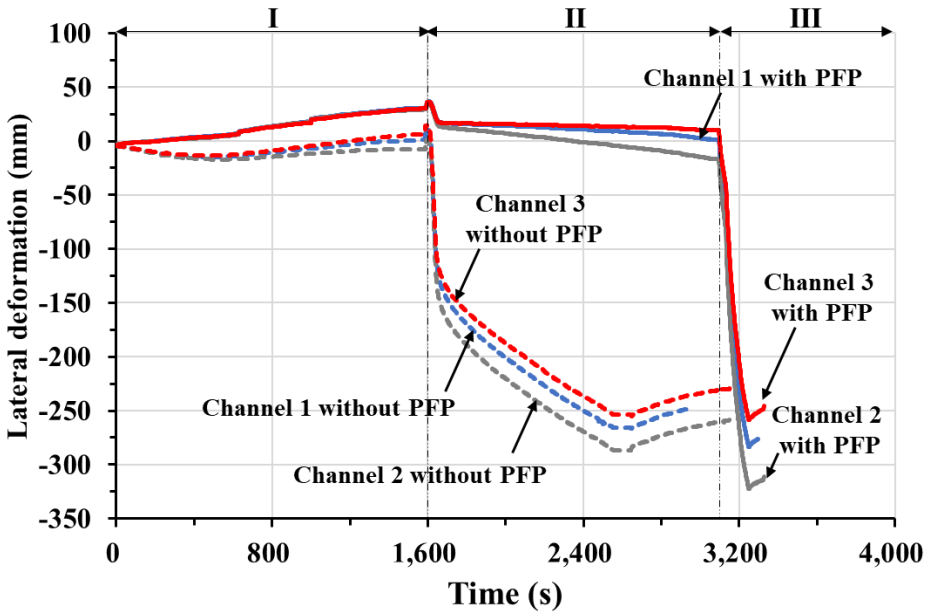

Figure 3.42 Comparison of load-lateral deformation curves between the fire test without and with PFP of the test structure at the three monitoring points.

Figure 3.43 Deformed shapes of the test structure for the fire test with PFP (fire protection materials were removed).

3.10 Concluding Remarks

This chapter aimed to present a fire test database on the collapse of a full-scale steel stiffened plate structure without and with passive fire protection (PFP) under lateral patch loading. For the fire test with PFP, transverse frames

were insulated by cerawool which is a PFP material. The test is intended to experimentally examine the effects of passive fire protection on the collapse of steel stiffened plate structures in fires. Based on the study, the following conclusions can be drawn.

- It was confirmed that setting up the test structure was successful.
- Gas cloud temperatures inside the furnace were increased using a burner with a supply of liquefied petroleum gases. It was confirmed that the increase of gas cloud temperatures was controlled successfully to be 15% below the target ISO 834 fire curve.
- The time history of the steel temperatures transferred from the heat of gas clouds as well as the gas cloud temperatures themselves was measured at monitoring points using thermo-electric couple sensors.
- The PFP application to test jigs along the four edges of the test structure was fully effective as steel temperatures remained low.
- For the fire test with PFP, steel temperatures of fire-protected transverse frames also remained low and thus applied loads were sustained until the structural collapse was reached.
- Lateral patch loads were applied at the centre of transverse frames using two hydraulic loading actuators. The synchronising of the same loading at two points was secured. Patch load applications were made in two steps for the fire test without PFP and it was three steps for the fire test with PFP to make a comparison. The first two load steps were allocated to be identical to both tests.
- For the fire test without PFP, the lateral deformations of the tested structure were small during the first load step, but they increased dramatically at 1,600 s, which were regarded as a critical period for fire safety as far as the loading and temperature schemes considered in the present thesis are applied. A similar assessment of fire safety can of course be made for different loading conditions.
- For the fire test with PFP installed to transverse frames, in the first load step with a lateral patch load of 15 tf, lateral deformations of fire-protected transverse frames were rather slightly increased upward in the opposite direction to the lateral patch loading direction. This may have been caused by the heat expansion of the metal due to the

elevated gas temperature and fire unprotected parts deforming while the fire-protected transverse frames remained intact. In the second load step with a lateral patch load of 50 tf, the transverse frames with passive fire protection were kept intact, although those without passive fire protection collapsed immediately after the loading. The test structure collapsed at 3,101 s at the third load step when 75 tf were applied.

Chapter 4 Advanced Computational Models for the Structural Crashworthiness Analysis in Fires

4.1 Introduction

In this chapter, computational models were developed using the transient thermal elastic-plastic large-deformation finite element method. The computational model to analyse heat transfer from ambient temperature to steel temperature was developed for steel plated structures without or with PFP. The computational model for the analysis of the fire-induced progressive collapse behaviour without or with PFP was formulated at elevated temperatures. The computational models were then validated by comparison with the test data in Section 4.5.

Key tasks to analyse the fire-induced progressive collapse behaviour are heat transfer analysis to define temperature in steel transferred from ambient temperature elevated due to fire, and thermal elastic-plastic large-deformation analysis to identify the progressive collapse behaviour.

Two methods are relevant to calculate the steel temperature from gas temperature, namely the thermal analysis method and the heat transfer equation method. Heat transfer equations for structures without or with PFP in fire may be obtained from EN 1993-1-2 (2005). Thermal analysis for steel structures without PFP can be conducted by finite element method using plate-shell elements (Paik et al. 2013). PFP is usually modelled using solid elements as described by Paik (2020), but for computational costs, a single layer 'shell' element may also be employed. In the present study, the developed models were implemented into LS-DYNA code for the thermal analysis for steel plated structures without or with PFP. The PART_COMPOSITE function in LS-DYNA code was employed to model steel and PFP using shell elements in a 'single layer'. The temperatures of the lower, middle and upper surfaces of the shell can be different and they were calculated separately considering the shell thickness. This was possible in the LS-DYNA code even if steel and PFP were modelled using single-layer shell elements.

4.2 Heat Transfer Analysis

For heat transfer analysis, the heat fluxes transferred from the fire to surrounding structures in time must be defined. The total heat flux per unit area q_{total} is calculated by the sum of the contribution to convection and radiation:

$$q_{total} = q_c + q_r \,, \tag{4.1}$$

where q_c is the heat flux by convection per unit area and q_r is the heat flux by radiation per unit area.

The heat transfer by convection between the structural element with the temperature θ_m and the surrounding gas cloud with the temperature θ_g is suggested by Cengel and Ghajar (2010):

$$q_c = h_c(\theta_m - \theta_g)\,, \tag{4.2}$$

where h_c is the coefficient (W/m^{2}K) of convection. To define the coefficient h_c, an engineering judgement can be attempted. Table 4.1 indicates typical values of the convection heat transfer coefficient (Franssen and Real 2010).

The heat transfer by radiation between the structural element at absolute temperature θ_m and fire environment at an absolute temperature θ_g is suggested by Franssen and Real (2010):

$$q_r = S\varepsilon_g\varepsilon_s(\theta_m{}^4 - \theta_g{}^4)\,, \tag{4.3}$$

where S is the Stephan-Boltzmann constant (5.67 × 10-8 W/m^{2}K^4), ε_g is the emissivity coefficient of gas (which normally takes a value of 1.0), and ε_s is the emissivity coefficient of steel (Franssen and Real 2010). Table 4.2 indicates the radiation emissivity coefficient for different metals by Cengel and Ghajar (2010).

The BOUNDARY_FLUX SET function in LS-DYNA allows the user to input convection and radiation coefficients corresponding to each structural member. In addition, if different sides of the member are exposed to a different temperature, different conditions can be entered on the lower and upper surface of the shell.

For the nonlinear structural response analysis, the definition of adequate boundary conditions and design loads of the target structure is required. The

BOUNDARY_SPC_SET function in LS-DYNA allows the user to input the translational constraint and rotational constraint of nodes. To apply the load condition, the LOAD_NODE_SET function can be used for external loads and the LOAD_BODY_Z function can be used for the application of gravity. In addition, using the CONTACT function, various contact conditions can be entered.

It is important to define the mechanical and thermal properties of the material to perform a highly reliable heat transfer and structural response analysis. The FEA procedure in the present chapter uses the test database (material properties of steel under elevated temperatures) presented in Chapter 3. As shown in Figure 3.7, the nominalised factor represents a ratio of the relevant parameter at a higher temperature to that at room temperature. Figure 3.7 confirms that the EN 1993-1-2 curve is an acceptable guideline for characterising the impact of increased temperatures on the mechanical properties of steel as it is in good agreement with tension testing. The reduction trend of ultimate tensile strength is quite similar to that of yield strength. Hence, the FEA procedure applied the EN1993-1-2 to define the mechanical properties at elevated temperatures. With the increase in temperatures, the mechanical properties of steels such as elastic modulus (Young's modulus), yield stress and ultimate tensile stress are significantly decreased, while the fracture strain increases. This was confirmed by tensile coupon testing with varying elevated temperatures in the present study, and it was found that the EN1993-1-2 formulas are in very good agreement with the test database, and they can therefore be adopted to define the mechanical properties of steels in fires for the purpose of nonlinear finite element analysis. In this regard, the definition of the EN1993-1-2 formulas was used for the present nonlinear finite element analysis rather than using the test databases themselves. This will be a more practical option for industrial applications as presented in Chapter 5 of application examples to realistic ship-shaped offshore installations in fires.

Table 4.1 Typical values of the convection heat transfer coefficient h_c .

	h_c (W/ m^{2}K)
Unexposed side of separating elements:	
Radiation considered separately	4
Radiation is implicitly considered in the convection	9
Surface exposed to the fire:	
Standard fire curve (ISO 834)	25
Hydrocarbon fire curve (EN 1991-1-2)	50
Parametric fire, zone fire model, or external member	35

Table 4.2 Radiation emissivity coefficient ε_s for different metals.

Material		Emissivity (ε_s)
Steel	Polished sheet	0.08-0.14
	Commercial sheet	0.20-0.32
	Heavily oxidised	0.81
Stainless steel	Polished	0.17-0.30
	Lightly oxidised	0.30-0.40
	Highly oxidised	0.70-0.80
Aluminium	Polished	0.04-0.06
	Commercial sheet	0.09
	Heavily oxidised	0.20-0.33
	Anodised	0.80

4.3 Nonlinear Structural Analysis

For the nonlinear structural response analysis, the definition of adequate boundary conditions and design loads of the target structure is required. The BOUNDARY_SPC_SET function in LS-DYNA allows the user to input the translational constraint and rotational constraint of nodes. To apply the load condition, the LOAD_NODE_SET function can be used for external loads and the LOAD_BODY_Z function can be used for the application of gravity. Besides, using the CONTACT function, various contact conditions can be entered. It is very important to accurately define the mechanical and thermal properties of the material to perform a highly reliable heat transfer and structural response analysis.

As described in Section 2.4.2 modelling of steel structures using shell elements and modelling of the PFP using solid elements is time-consuming. As such, simplified models were considered in the present study, where the PFP was modelled as a virtual steel plate with a single layer.

4.4 Application of the Computational Models to the Tested Structures

The computational models presented in Sections 4.2 and 4.3 were applied to the fire-induced progressive collapse testing on full-scale steel stiffened plate structures without or with PFP under lateral patch loading. Details of the test results are presented in Sections 3.8 and 3.9.

During the process of welding fabrication, initial imperfections are inevitably developed in the form of initial deflections and residual stresses, which can significantly affect the ultimate strength under predominantly axial compressive loading, refer to articles (Paik et al. 2020; Paik et al. 2021a, 2021b; Ryu et al. 2021; Yi et al. 2019, 2020, 2021) which are associated with the present study. Conversely, the tested structures under consideration were subjected to lateral patch loading at elevated temperatures, and the effects of initial imperfections on the structural collapse in fires are considered to be very small. In this regard, the welding-induced initial imperfections were not measured.

4.4.1 Construction of the FE Model

LS-PrePost (2020) for pre-processing and post-processing of LS-DYNA code was used to conduct the finite element analysis. It has advantages because multiple models are allowed to import and combine from various sources: LS-DYNA keyword, IDEAS neutral file, NASTRAN bulk data, STL ASCII, and STL binary formats. The FE model of the tested structure was created by ANSYS Mechanical APDL, with which the information of the nodes and elements could be written as a file that can be read by the LS-PrePost program by using the Solution_Write Jobname.k function.

To make the model as close to the experimental conditions as possible, the tested structures with test jigs and the top of the fire test facility were included in the model. Because the four edges of the tested structures were welded to the test jigs as shown in Figure 4.1, the tested structure and the test jigs were modelled as one unit. To impart contact conditions between the test jigs and furnace, the top of the fire test facility was created 10 mm away from the test jigs considering the thickness of the steel plate. The top of the fire test facility was modelled in size sufficiently wider than the area of the contacted test jigs, so it would not be penetrated by the node on the contact surface.

The tested structures included dummies and patch load plates and the top of the fire test facility as shown in Figure 4.2. The size of steel patch load plates was 400 mm × 400 mm × 30 mm and the steel plate with a thickness of 10 mm.

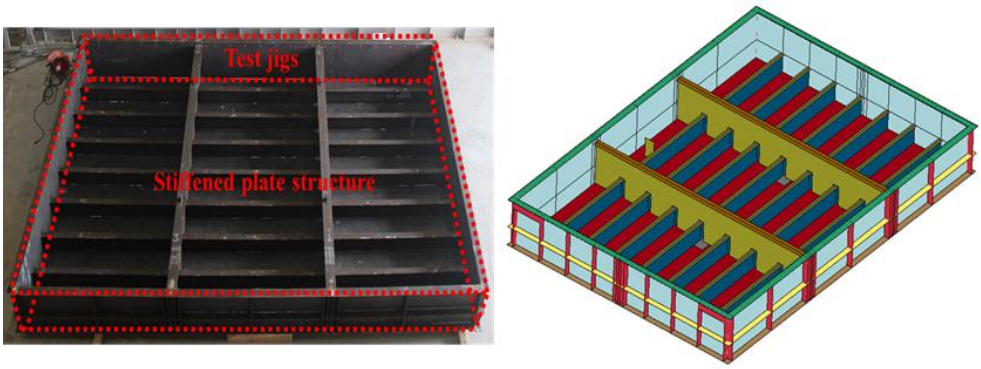

Figure 4.1 The tested structure (left) and the FE model (right).

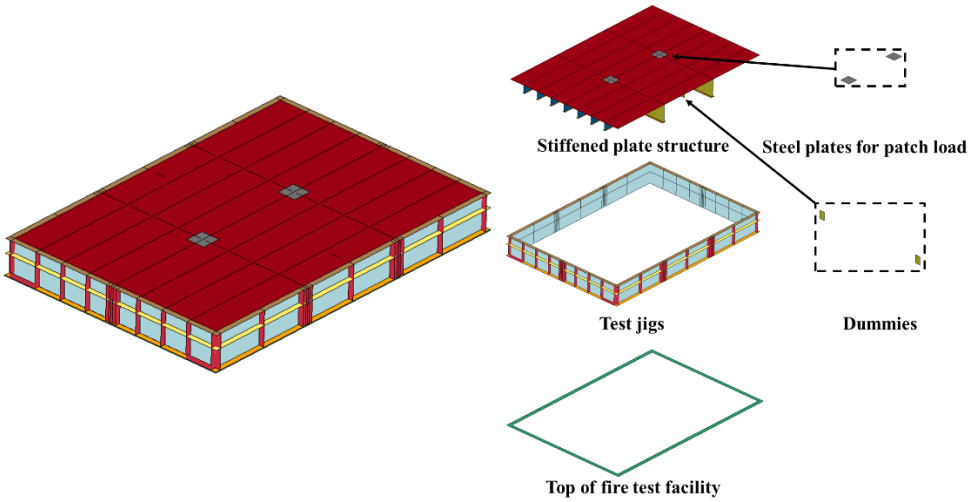

Figure 4.2 Composition of the geometry for the finite element model.

4.4.1.1 Test Structure Without PFP

The first test structure had no PFP, but two transverse frames of the second test structure were protected by PFP. PFP was modelled using shell elements together with PART_PART function in LS-PrePost. This function allowed the users to characterise each part of the structures by entering the mechanical material property ID, thermal material property ID, and member section information ID containing thickness information for the selected member. In addition, all members were given 10 mm thickness, except the stiffened plate structure welded with patch load plates. Since the whole test structures were

modelled using single-layer shell elements, the thickness of the shell elements representing stiffened plate structure welded with patch loads plates was given 40 mm (30 mm patch load plate and 10 mm stiffened plate structure). The mechanical and thermal properties of the material were defined in the MAT function, and the member section information of the shell elements was defined in SECTION_SHELL.

4.4.1.2 Test Structure With PFP

Steel plate members with PFP were modelled using shell elements, where the PART_COMPOSITE function, the thickness of the material, the mechanical material property ID, and thermal material property ID of the steel and PFP were entered separately. In this function, member information was defined in correspondence with the normal vector of each member, so it is essential to secure the normal vector of each member at the modelling stage. In the FE model of the tested structure with PFP, the PART_COMPOSITE function was used for the plate members of the test jigs and the two transverse frames where the PFP was applied.

The AUTOMATIC_SURFACE_TO_SURFACE_COMPOSITE function was used to apply the contact condition between the transverse frames and the longitudinal stiffeners until the structure collapsed. Since it is a function that can only be used between the members defined as the composite type, the longitudinal stiffeners were also applied with the PART_COMPOSITE function, except there is only one layer since there is no PFP on longitudinal stiffeners. For a more accurate shell element response calculation, the CONTROL_SHELL function is used. The ISTUPD option was activated to apply the shell thickness change for deformable shell elements, and the THSHEL option was activated to calculate the temperature gradient through the shell element thickness.

The same FE model was used to perform both heat transfer analysis and structural response analysis simultaneously. The mesh created for heat transfer analysis and structural response analysis is shown in Figure 4.3. The tested structure with the test jigs FE model consisted of 47,027 nodes and 47,090 shell elements. Most mesh sizes were 50 mm × 50 mm, except for some parts where smaller meshes were required. Figure 4.4 shows the distribution of the maximum and minimum side lengths of each element.

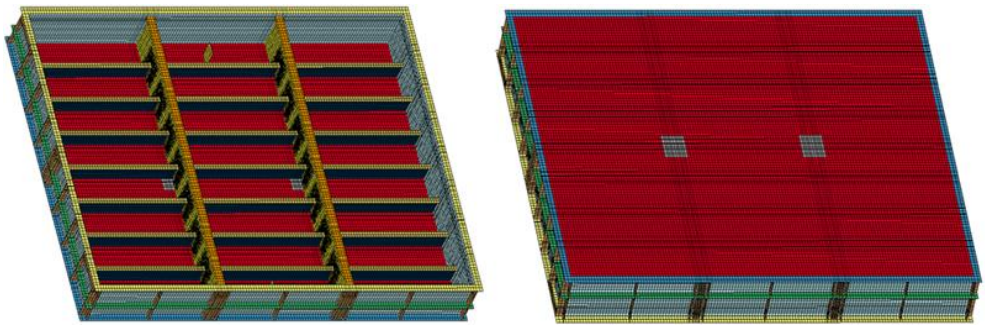

Figure 4.3 FE model for heat transfer analysis and structural response analysis.

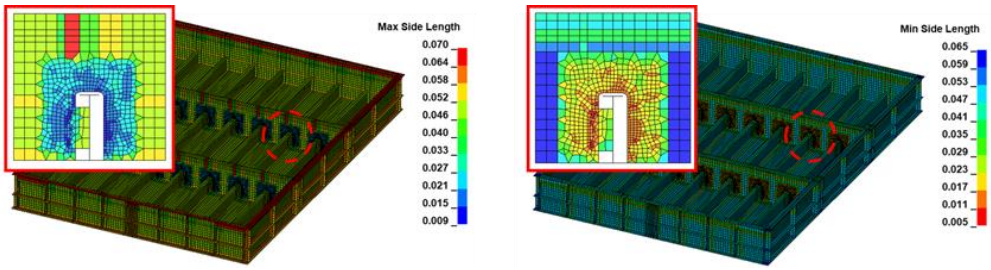

Figure 4.4 Distribution of maximum and minimum side length of each element.

4.4.2 Mechanical Properties at Elevated Temperature

The mechanical properties of steel at elevated temperatures were defined from the reduction factor of EN1993-1-2 (2005). As discussed in Section 3.3, the EN1993-1-2 guidance of the reduction factor was confirmed to be in good agreement with material test data. In LS-PrePost, the mechanical properties of materials were defined up to eight different temperatures using the MAT_004-ELASTIC_PLASTIC_THERMAL function. Table 4.3 shows the input values for the function.

The properties of PFP were defined using the MAT_004-ELASTIC_PLASTIC_THERMAL function. The PFP material used in this study was a product called cerakwool, and its yield strength at room temperature is 0.75 MPa. The strength of the PFP was negligible because it was weak enough to be torn by bare hand. For this reason, Elastic modulus and hardening modulus values were assumed to be 1 and 10-9, respectively. The thermal properties of steel and PFP were defined by loading the specific heat curve and the thermal conductivity curve under elevated temperature into

the computational model using MAT_T10-THERMAL_ISOTROPICTD_LC function. The curve ID was defined in the DEFINE_CURVE function

Table 4.3 Mechanical properties of the AH32 for finite element analysis.

Temperature	0 ℃	100 ℃	400 ℃	
Elastic modulus (MPa)	2.240e+5	2.240e+5	1.568e+5	
Yield stress (MPa)	3.396e+02	3.396e+02	3.396e+02	
Hardening modulus (MPa)	1.000e-10	1.000e-10	1.000e-10	
Temperature	500 ℃	600 ℃	700 ℃	800 ℃
Elastic modulus (MPa)	1.344e+5	6.943e+4	2.912e+4	2.016e+4
Yield stress (MPa)	2.649e+02	1.596e+02	7.810e+01	3.735e+01
Hardening modulus (MPa)	1.000e-10	1.000e-10	1.000e-10	1.000e-10

4.4.3 Boundary Conditions

The boundary conditions applied for the LS-DYNA analysis are described in Figure 4.5. The welded sections to fix the test jigs on the furnace were given fixed conditions, and the top of the fire test facility mentioned before was modelled and assumed to be a rigid body. The dimensions of the welded sections were described in Section 3.5. The BOUNDARY_SPC_SET function can be used to input the translational constraint and rotational constraint on required sections (welded sections).

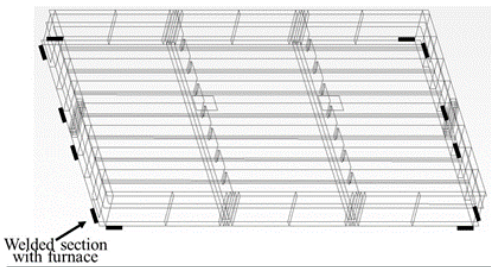

Boundary	Description
Welded section	U_X, U_Y, U_Z, R_X, R_Y, R_Z = Fixed
Furnace	Rigid body

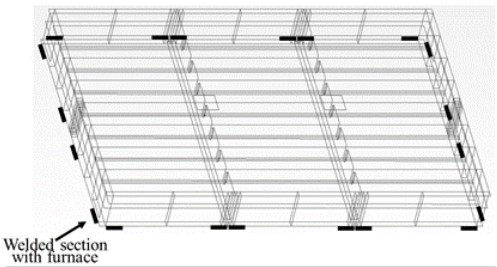

Boundary	Description
Welded section	U_X, U_Y, U_Z, R_X, R_Y, R_Z = Fixed
Furnace	Rigid body

Figure 4.5 Boundary conditions of FEA for the test structure without PFP (left) and with PFP (right).

The lateral deformation of the tested structures occurred, and the structural members were in contact with one another, and thus the contact condition was considered to prevent the node of one member from penetrating another member to affect the accuracy of the simulation.

The CONTACT_AUTOMATIC_SINGLE_SURFACE function was used for the contact condition between the test jigs and the top surface of the horizontal fire test facility. When the tested structures collapsed, the contact condition between the transverse members and the longitudinal members were also considered.

For the FE model without PFP on the transverse frames, the contact condition was assigned using the AUTOMATIC_SINGLE_SURFACE function in the same way as the contact condition between the test jigs and the top surface of the fire test facility.

For the FE model with PFP on the transverse frames, the AUTOMATIC_SURFACE_TO_SURFACE_COMPOSITE function was used because the transverse frames with PFP were modelled using the PART_COMPOSITE function. The commonly used static and dynamic coefficient of friction was used as 0.3 (Paik 2020). The default values for computation with contact surfaces were applied using the CONTROL_CONTACT function.

4.4.4 Gas Cloud Temperature

The fire CFD simulation was not performed to identify the distribution of gas cloud temperature in the present study. Instead, the gas cloud temperature measured from the tests was used for the heat transfer analysis to define the steel temperature, and it was assumed that the gas temperature distribution is uniform over the structures. The tests were terminated after the collapse of the tested structures was reached, and the actuator and heat system were turned off. However, the FE analysis was continued until and after the tested structures collapsed. Figure 4.6 compares the gas temperature of tested structures with time. The database of maximum gas cloud temperature for two fire tests is provided in Appendix A.5.

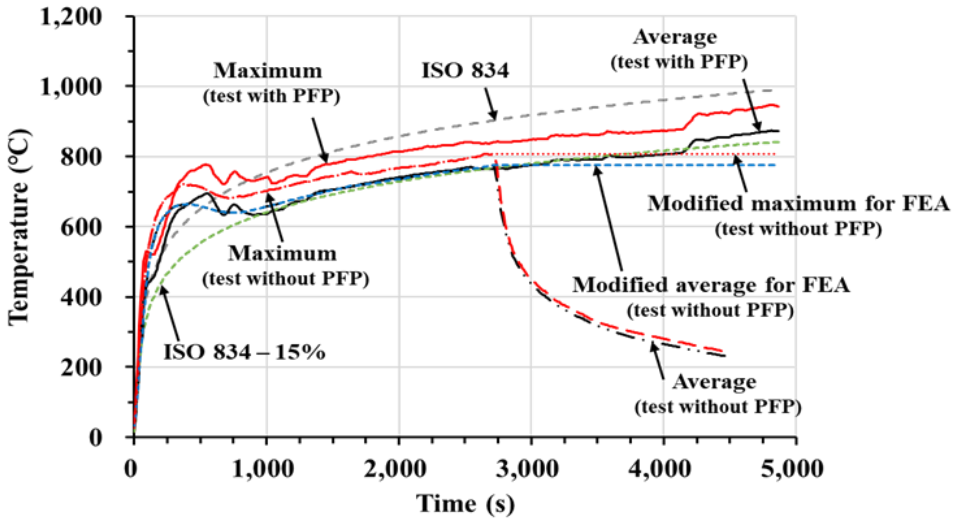

Figure 4.6 Comparison of gas cloud temperature between tests, computational models and ISO suggestions.

Heat loss on the side unexposed to fire was also considered, and the ambient room temperature was measured by the furnace facility during the tests, and it was confirmed that the ambient room temperature distribution was almost uniform. In the tested structure without PFP, the ambient room temperature rose from 27.6 ℃ to 30.6 ℃ after an hour, and that with PFP, it was 17.6 ℃ to 22.6 ℃.

For the heat transfer analysis, heat flux calculation conditions were defined. Heat flux was calculated by the sum of heat flux due to convection and heat flux due to radiation. The FE model developed in the present study was composed of shell elements, and thus it was required to calculate the heat flux by convection and radiation on both sides, so a total of four calculation terms were inevitable. Heat flux calculation conditions were defined using the BOUNDARY_FLUX_SET function, which allowed the user to enter the convection and radiation coefficients on each side of the shell element.

The convection coefficient and the radiation coefficient were defined for the heat flux calculation conditions. In the present study, the convection coefficient of the unexposed side was taken as h_c = 10 W/m^{2}K, and the convection coefficient of the exposed side was taken as h_c = 19 W/m^{2}K by engineering judgement (Paik et al. 2013). The value of the radiation emissivity coefficient of steel was taken as ε_s = 0.24, and the value of the radiation

emissivity coefficient of the PFP was taken as ε_s = 0.90 provided by the manufacturer. The initial temperature of the FE model was set to be 20 ℃ using the INITIAL_TEMPERATURE_SET function.

4.4.5 Lateral Patch Loads

The lateral patch loads applied to the tested structure were defined in the FEA. The LOAD_BODY_Z function was used to impart gravity, and the BODY_NODE_SET function was used to impart the lateral patch loads at the centre of each transverse frame applied by the actuator. Unlike the actual experiments, the lateral patch loads were maintained even after the collapse of the test structure to continuously observe the progressive collapse behaviour. Figure 4.7 shows the patch loads applied at the centre of each transverse frame for the fire collapse analysis model of both experiments.

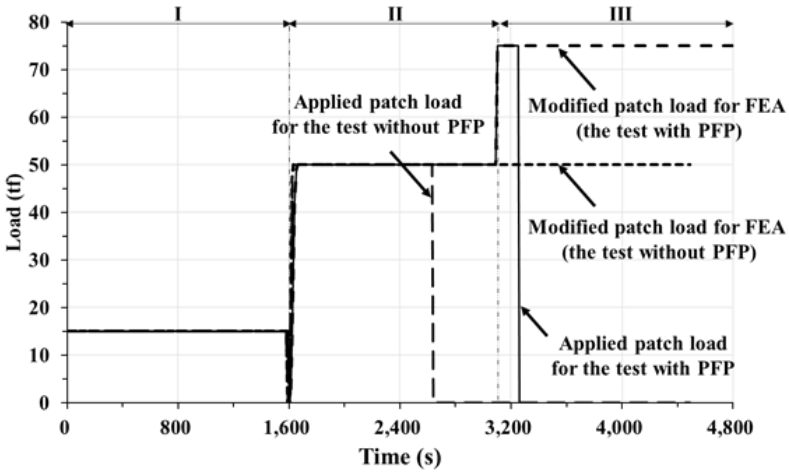

Figure 4.7 Three-phased model for assumed patch load history in the computational model.

4.4.6 Other Settings

Using the CONTROL_SOLUTION function, ‘Structural analysis only’, ‘Thermal analysis only’, or ‘Coupled structural thermal analyses were selected and performed. To confirm the exact coefficient of the convection and the radiation for further finite element analysis, the average temperature data collected from the furnace test facility was first adopted for the heat transfer analysis by selecting the ‘Thermal analysis only’ option. For the coupled structural thermal analysis, the maximum temperature in the furnace was

adopted since the tested structure was mainly affected by the maximum gas cloud temperature inside the furnace. Besides, the transverse frames which are the main structural members in the test were exposed closer to the location of the maximum temperature in the furnace.

During the actual physical model testing, for safety reasons, both experiments were terminated immediately after the collapse of the test structures, but for the numerical analysis, the structural response analysis was performed until 5,000 s to observe the behaviour of the structure after the collapse. Termination time was entered using the CONTROL_TERMINATION function. For the heat transfer analysis, the time step was set to be 1 s using the CONTROL_THERMAL_TIMESTEP function. Other detailed settings for the heat transfer analysis were set using CONTROL_THERMAL_NONLINEAR and THERMAL_SOLVER functions.

The numerical algorithms for structural response analysis can be classified into the implicit analysis and explicit analysis procedure depending on the differential equation analysis method. The present study used the implicit finite element techniques, which have a relatively high accuracy of analysis results by calculating stable response of structure over time, and with less constraint on element size or time interval (Van den Boogaard et al. 2003). The implicit analysis method was applied with the IMFLAG value as 1, and the time step was applied as 50 s with the DT0 value as 50 in the CONTROL_IMPLICIT_GENERAL function. To control the implicit nonlinear method, the parameters were used with the CONTROL_IMPLICIT_SOLUTION and CONTROL_IMPLICIT_SOLVER functions. In case an error occurred due to a convergence problem, various tolerance values were modified.

4.5 Validation of the Developed Computational Models

4.5.1 Steel Temperatures

Figure 4.8 compares the temperature history of the tested structure without PFP, obtained from the test and predicated using the LS-DYNA heat transfer analysis. The Appendix A.6 provides the experimentally acquired steel temperatures for the fire test without PFP as shown in Figure 4.8. It is recognised that the heat transfer analysis is useful to predict steel temperatures

using the finite element method. The temperature of the structure calculated through heat transfer analysis is very well matched with the temperature measured in the test. After 2,720 s the heat system was shut down in the test, but in the computational model, the temperature of the structure was continued to observe without reducing the heat loads. The temperature of the transverse frames was obtained by the heat transfer analysis, it reached 600 ℃ at 1,300 s, which means that the remaining yield strength of the transverse frames was 47% of the original yield strength.

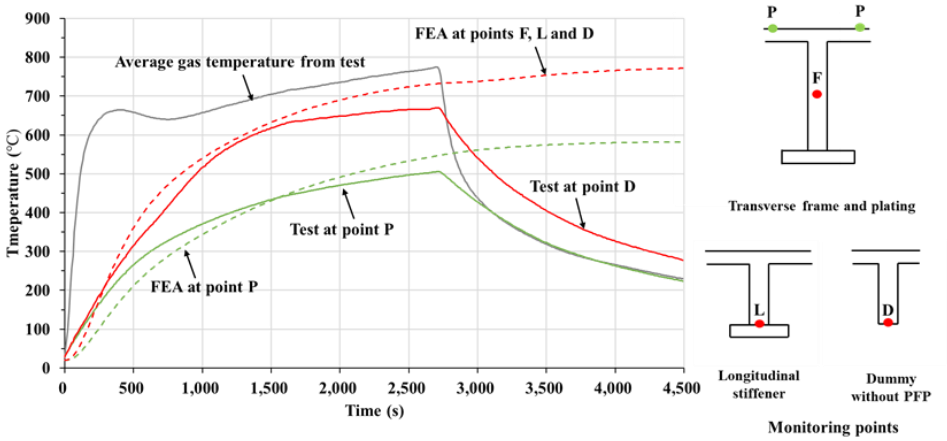

Figure 4.8 Comparison of the structure temperature between the test and computational model for the fire test without PFP.

Figure 4.9 compares the temperature variation of the tested structure with PFP obtained from the test and the LS-DYNA heat transfer analysis. The Appendix A.7 provides the experimentally acquired steel temperatures for the fire test with PFP as shown in Figure 4.9. It is recognised that finite element method analysis is useful for heat transfer analysis to calculate steel temperatures with fire protection. The temperature of the structure calculated through heat transfer analysis is very well matched with the temperature measured in the tests. After 4,860 s the heat system was shut down in the test, but in the computational model, the temperature of the structure was continued to be observed without reducing the heat loads. The temperature of the transverse frame obtained by the heat transfer analysis did not reach 300 ℃ even at 4,000 s.

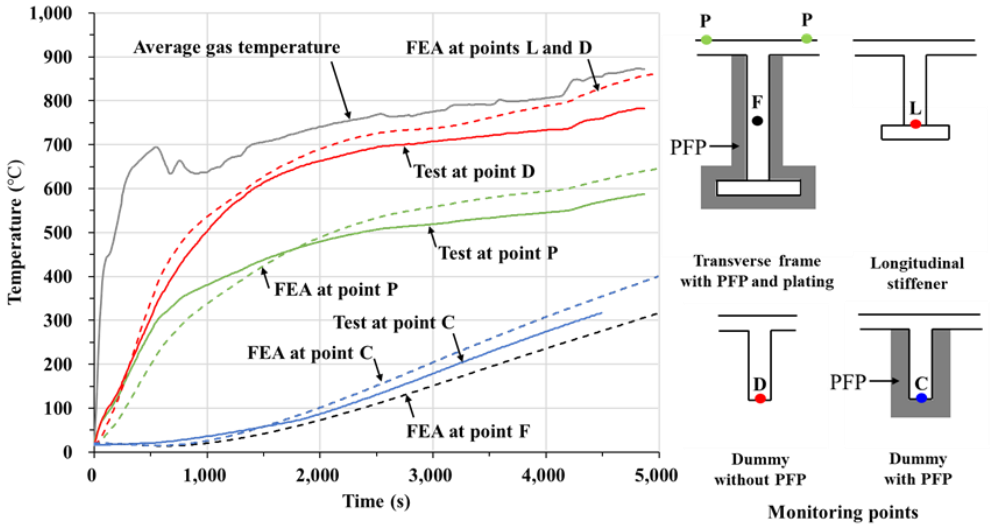

Figure 4.9 Comparison of the structure temperature between the test computational model for the fire test with PFP.

4.5.2 Structural Crashworthiness

Since the fire collapse of the structure is triggered by the highest temperature, the maximum gas temperature inside the furnace was used for structural response analysis. Figure 4.10 compares the lateral deformation at the centre of the transverse frame of the stiffened plate structure without or with PFP between the tests and the LS-DYNA nonlinear structural response analyses. The computations of the LS-DYNA analyses are in good agreement with the tests. Again, lateral deformations in the computations continued to increase since, unlike tests, heat loads and patch loads were not removed after the collapse of the structure.

Figure 4.11 and Figure 4.12 show the comparison of the deformed shape between the test and the computation with or without PFP after the collapse of the tested structure, showing a good agreement. It is found that the collapse of the structure with PFP was delayed, and longitudinal stiffeners were exposed to heat for a longer period, resulting in the deformation greater than the structure without PFP.

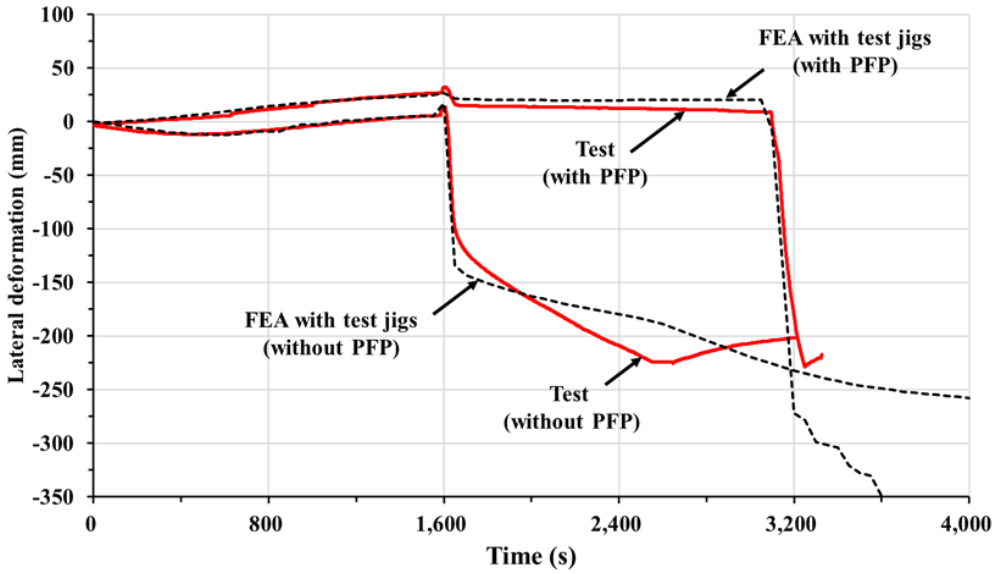

Figure 4.10 Comparison of the deformation at the centre of the transverse frame of the structure with or without PFP between the computation versus the test.

Figure 4.11. Comparison of the deformed shape for the structure without PFP after the collapse between the tested structure and the computation.

Figure 4.12 Comparison of the deformed shape for the structure with PFP after the collapse between the tested structure and the computation.

To confirm the effect of PFP more precisely, the boundary conditions of the two computational models were kept the same and the influence of the test jigs in deformation was eliminated. Since the four edges of the tested structures were fixed by the test jigs, the computational analyses used the same conditions as shown in Figure 4.13. Figure 4.14 shows the comparison of transverse frame temperature without and with PFP as obtained from the computations. For the structure without PFP, the temperature of transverse frames reached 600 ℃ at 1,050 s. On the other hand, the temperature of transverse frames for the structure with PFP was kept under 200 ℃ until 3,000 s.

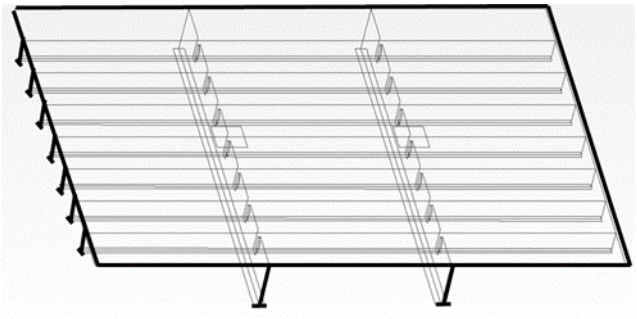

Boundary	Description
4 Edges	U_X, U_Y, U_Z, R_X, R_Y, R_Z = Fixed

Figure 4.13 Computational model of the steel stiffened plate structure without test jigs.

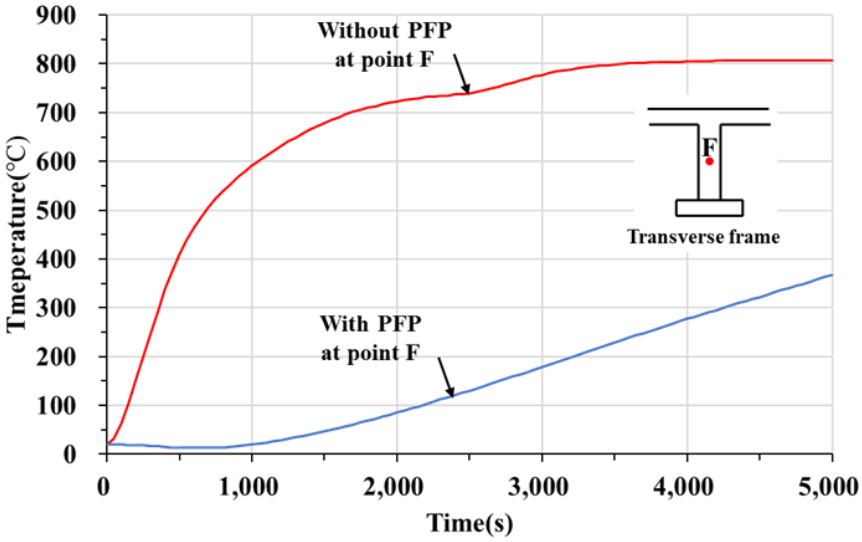

Figure 4.14 Comparison of transverse frame temperature of the structure without PFP versus with PFP as obtained from the computations.

As the steel temperature increases, the steel structure loses the strength of the member, which can easily lead to collapse. The deformation of the stiffened plate structures according to PFP at 500 s, 1,600 s, and 3,000 s are shown in Figure 4.15, Figure 4.16, and Figure 4.17. The transverse frames protected by PFP remained at low temperature, with small deformation. This means that PFP is an effective option to delay the collapse of the structure. Comparing the lateral deformation at the centre of the transverse frame without and with PFP, the effect of the PFP is straightforward on the fire-induced progressive collapse of steel stiffened plate structures as shown in Figure 4.18. The structure without PFP reached collapse under a patch load of 100 tf at 1,630 s. In the same condition, conversely, the structure with PFP was still intact with a small deformation of 23 mm and eventually reached collapse at 3,050 s.

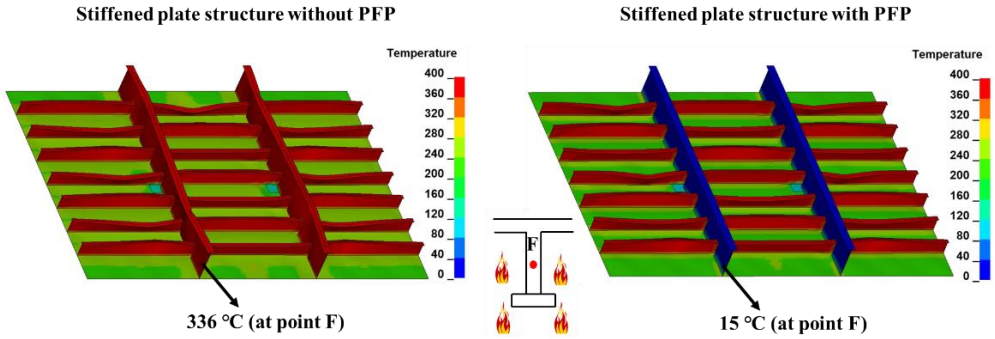

Figure 4.15 Comparison of steel temperature distributions and deformation after 500 s in computational model.

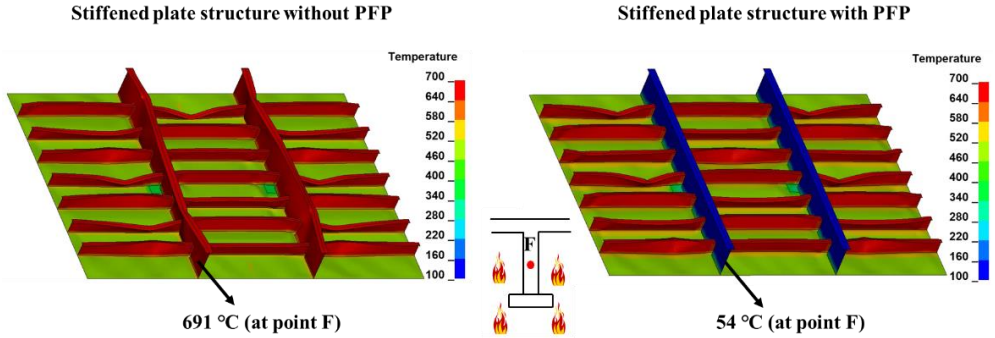

Figure 4.16 Comparison of steel temperature distributions and deformation after 1,600 s in computational model.

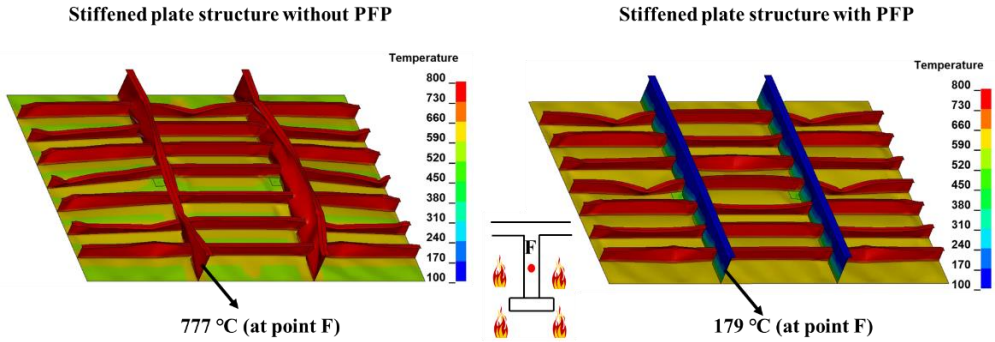

Figure 4.17 Comparison of steel temperature distributions and deformation after 3,000 s in computational model.

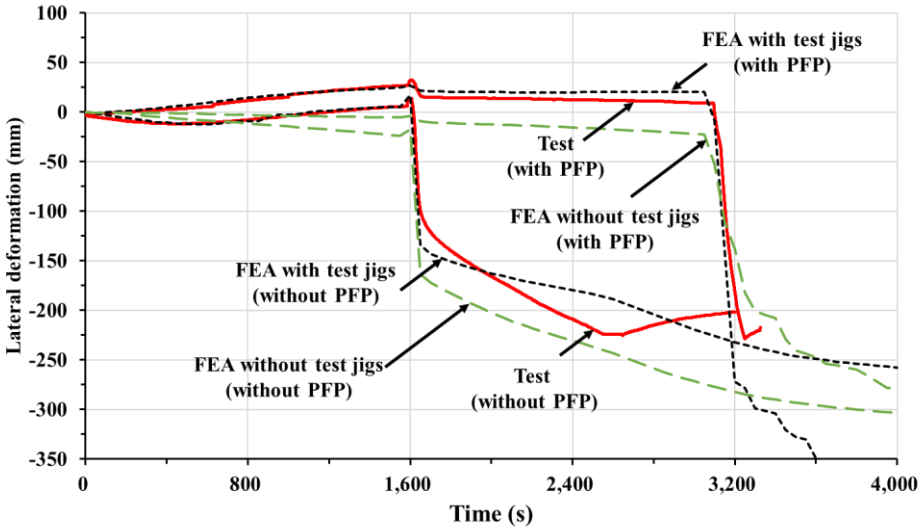

Figure 4.18 Comparison of the lateral deformation at the centre of the transverse frame without PFP versus with PFP.

For the structure with and without PFP, comparing the deformed shape during two lateral patch load phases: 500 s to 1,600 s (maintained at 15tf), 1,600 s to 3,000 s (maintained at 50tf). The different plate members suffered significant deformations even though the lateral patch loading was kept constant. This means that as the steel temperature increases, the steel structure continues to lose its strength leading to the structural members collapsing progressively regardless of the external force. In addition, progressive collapse results when an initially localised failure of a structural element, in this case, the two transverse frames, propagates to other elements leading to a broader structural failure.

4.6 Concluding Remarks

The objective of this chapter was to establish a procedure for the nonlinear computations of the fire-induced progressive collapse behaviour for steel stiffened-plate structures without and with passive fire protection (PFP). Nonlinear finite element method computational modelling techniques for both the heat transfer analysis and the thermal elastic-plastic large-deformation analysis were developed, and they were validated with a comparison with the experimental data. Based on the results, the following conclusions and insights can be drawn.

- Only shell elements were used to model both plating and web and flange of stiffeners. Also, PFP was modelled using a single layer shell

element instead of a solid element. It was confirmed that this modelling technique is successful for both the heat transfer analysis and the nonlinear structural response (fire-induced progressive collapse) analysis.

- Heat fluxes are transferred from fire to the surrounding structures in association with convection and radiation. For the heat transfer analysis, the convection heat transfer coefficient and radiation emissivity coefficient should be defined properly because they significantly affect the heat transfer characteristics.
- Similar to the progressive collapse analysis of steel plated structures at room temperature, not only geometric properties but also material properties should be defined accurately. To account for the fact the material properties are significantly reduced at elevated temperatures, the reduction factor of the material properties suggested by the EN 1993-1-2 is useful to apply.

Chapter 5 Applied Example to A Hypothetical VLCC-Class FPSO Unit Hull Topside Structures

5.1 Introduction

In previous chapters, computational models for the fire collapse analysis of steel stiffened-plate structures were developed and these models were validated through a comparison with full-scale physical model tests in fire scenarios. The developed computational models were based on transient thermal elastic-plastic large-deformation finite element (FE) methods. In this chapter, the progressive collapse behaviour of the topside structures of a ship-shaped offshore installation in fire events was analysed using the abovementioned computational models. Specifically, the topside structures of a hypothetical VLCC-class floating, production, storage and offloading unit (FPSO) hull, shown in Figure 5.1, were considered. Since all the major processes towards fluid products are conducted on the topside, fires have been identified as one of the most significant hazards for FPSO which may result in structural collapse leading to casualty or severe damages to asset and the environment.

This chapter aims to demonstrate the applicability of the newly developed computational models. A hypothetical VLCC-class FPSO unit hull was considered to simulate the progressive collapse behaviour of the topside structures, the upper deck structure to be exact. Gas leak scenarios were designed involving varying amounts of gas with the gas leaks directed to the upper deck structures. CFD simulations were then performed to identify the gas dispersion characteristics. Moreover, a heat transfer analysis was performed to determine the steel temperatures generated by the heated gas clouds in fires after ignition initiation. The fire-induced progressive collapse behaviour was simulated using the computational models based on the transient thermal elastic-plastic large-deformation FE methods. The boundary conditions of the upper deck were given corresponding to its contact conditions with the cargo hold. The lateral patch loading on the upper deck structure due to the enormous weight of topside modules and the axial compressive loading due to a sagging condition were considered. The serviceability limit state was used mainly to see if the sections not influenced by the fire exhibited any lateral deformation. A criterion based on the von Mises stress was used to assess when the structure loses its strength (lateral deformation) since the focal structure was affected by fire loads.

It is considered that the target FPSO is in operation where it is subjected to vertical bending moments which are a sum of still-water bending moment and wave-induced bending moment. Looking at the upper deck structures, they can be subjected to lateral dead loads arising from the weight of heavy process facilities and axial compressive loads due to sagging bending moments or axial tensile loads due to hogging bending moments. Axial tensile loads due to hogging bending moments may not be problematic in structural safety case studies. In this regard, the loading scenario was chosen so that the upper deck structures are subjected to lateral pressure dead loads arising from the weight of topside process facilities and axial compressive loads arising from sagging vertical bending moments, where the sagging vertical bending moments and subsequent axial compressive loads were increased monotonically until structural collapse state is reached. In this case, two types of limit states were considered: serviceability limit states and ultimate limit states. The former is associated with a critical value of lateral deformation and the latter is judged that the lateral deformation increases suddenly in an unstable way.

Figure 5.2 illustrates the practical procedure for analysing the fire-induced progressive collapse. The FLACS CFD code (FLACS 2021) and LS-DYNA code (ANSYS 2021) were used to perform the gas dispersion analysis and transient thermal elastic-plastic large-deformation FE analysis, respectively.

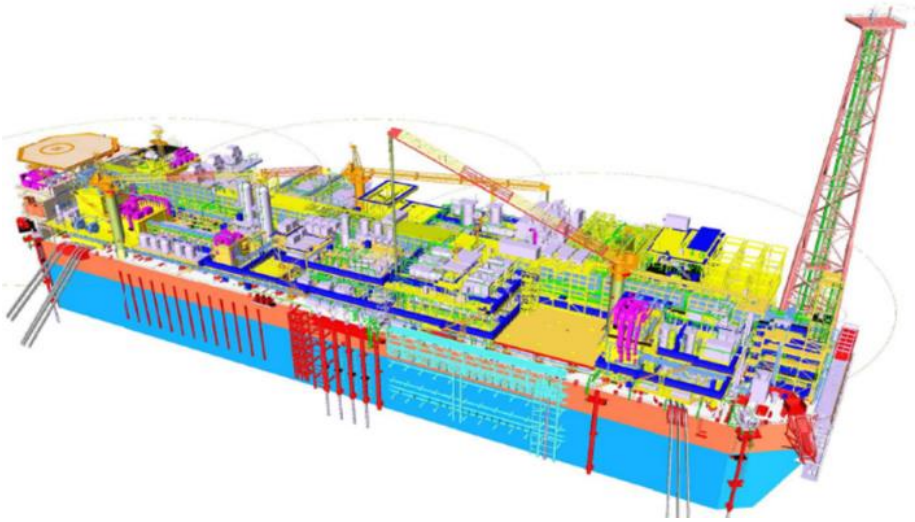

Figure 5.1 Hypothetical VLCC-class ship-shaped offshore installation.

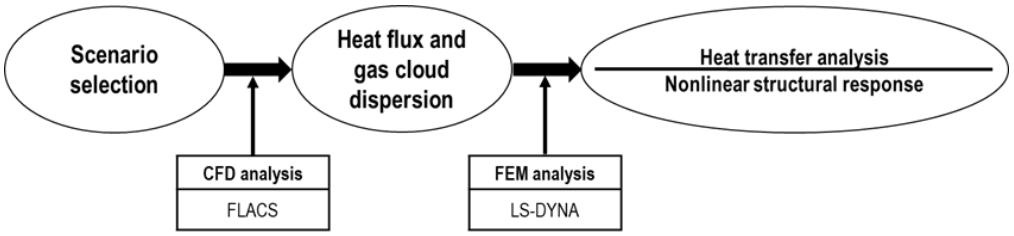

Figure 5.2 Procedure to analyse the progressive collapse in fire events.

5.2 Gas Leak Scenarios

In the scenarios, gases were assumed to leak from a pressure vessel on the topside modules. Five parameters were used to define three gas leak scenarios, categorised as minor, significant, and major (Paik 2020) based on the amount of gas leaked. All of the parameters except the leak amount were constant values.

- Leak amount = 1 kg (minor), 100 kg (significant) and 350 kg (major)
- Leak direction = –Z
- Leak position in the X-direction = 81.29 m
- Leak position in the Y-direction = 262.85 m
- Leak position in the Z-direction = 106.48 m

The gas leak scenarios applied for the computations are from the practices of the offshore industry (HSE 2017, Paik 2020). Figure 5.3 presents the detailed schematics of the topside modules for the FPSO hull. The leak direction –Z and the coordinates (X-, Y- and Z-direction) of leak position ensured the leakage occurred from the topside module P4 to the upper deck of the FPSO hull. For the fire CFD simulation, existing topside modules (P4 and S4) were used, and the coordinates of leak position were used in defining the coordinate in the FLACS code. In other words, for the present problem, the most unfavourable scenarios were selected. The selection of the scenarios was a deterministic approach rather than a probabilistic approach to ensure that the gas leaked from the topside module to the upper deck, so the area affected by the fire was the upper deck of the FPSO hull. The FLACS code was used to perform the CFD simulations of the gas dispersion for the three different leak amounts. For gas releases, the minor releases should be a leak amount <1 kg, the significant releases should be a leak amount <300 kg and the major releases should be a leak amount >300 kg. For this reason, the above-

mentioned leak amounts were selected. It was assumed that no shutdown equipment was activated during the leak.

For the gas leak scenarios, the industry recommended practices (HSE 2017, Paik 2020) based on historical measurements are grouped into three types, namely minor, significant, and major leaks. In this regard, the present study adopted these practices for the progressive fire collapse analysis, despite the scenario selection of gas leaks is not the focus of the present study. Rather, the present study aims to develop advanced computational models which are useful for the progressive fire collapse analysis at any given scenarios of gas leaks.

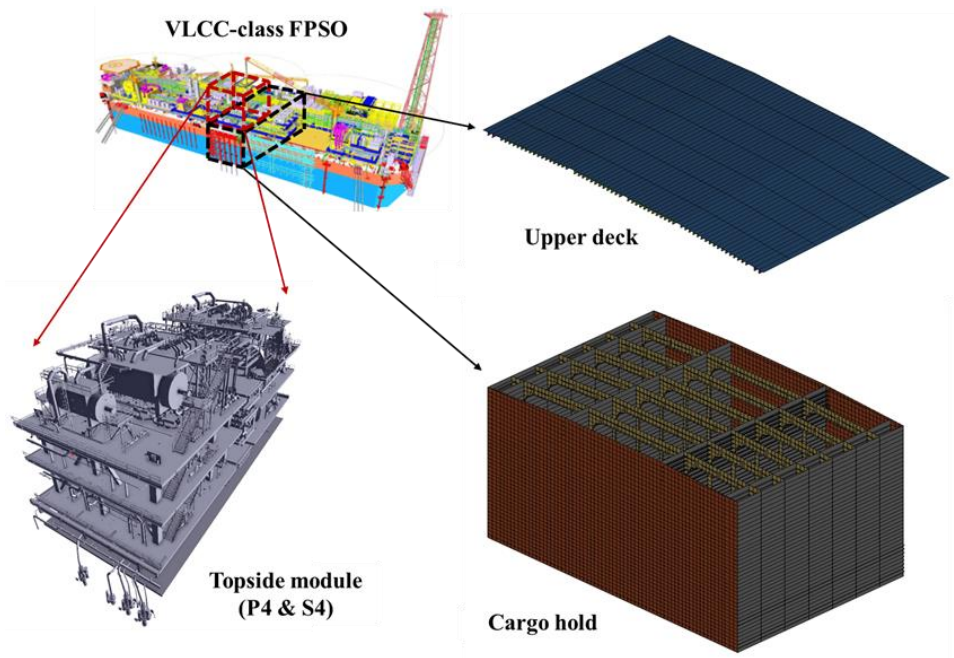

Figure 5.3 Details of the topside modules.

5.3 CFD Simulations for the Gas Dispersion

In general, leaked gases spread over time. CFD simulations were performed to analyse the characteristics of the gas dispersion patterns, which were time- and space-dependent. The gas cloud temperatures and heat fluxes caused by the fires at ignition were also determined using the CFD simulations. The physical correlation between the increased temperatures and heat fluxes in the gas cloud represents the fire loads. The radiation and convection associated with fire are crucial factors in determining fire loads (Paik 2020). The FLACS

code was based on a three-dimensional transient finite volume CFD method. Moreover, the fuel composition is a key factor influencing the mechanism of fires. Table 5.1 summarises the gas composition considered in the CFD simulations.

Table 5.1 Gas composition used in the CFD simulation.

Component	Mole fraction (%)
Nitrogen	0.38
Carbon dioxide	2.22
Methane	80.24
Ethane	5.69
Propane	5.36
Butane	3.20
Pentane	1.46

Figure 5.4 shows the FLACS model for the gas dispersion analysis of the topside modules P4 (port side) and S4 (starboard side), indicating the grids and leak location. The input data of the FLACS code included the conditions of fuel leakage such as the leak position, direction and amount and fuel temperature. Monitoring points were selected to investigate the gas dispersion characteristics, as shown in Figure 5.5. All the monitoring points lay in the space between the topside modules and upper deck structure of the FPSO, taking into account the fire impact area. The distance between individual points was 2 m. The relative gas cloud temperature distributions between the topside modules and upper deck structure of the FPSO 1 s and 10 s after ignition is shown in Figure 5.6. The fire did not reach the upper deck in the minor release scenario, but it reached the upper deck in the significant and major release scenarios.

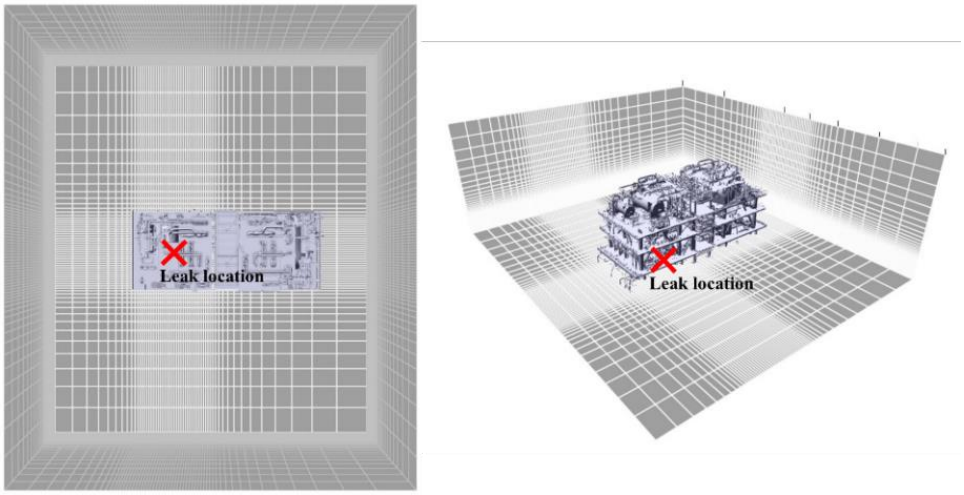

Figure 5.4 FLACS model with grids and leak location for the topside module P4.

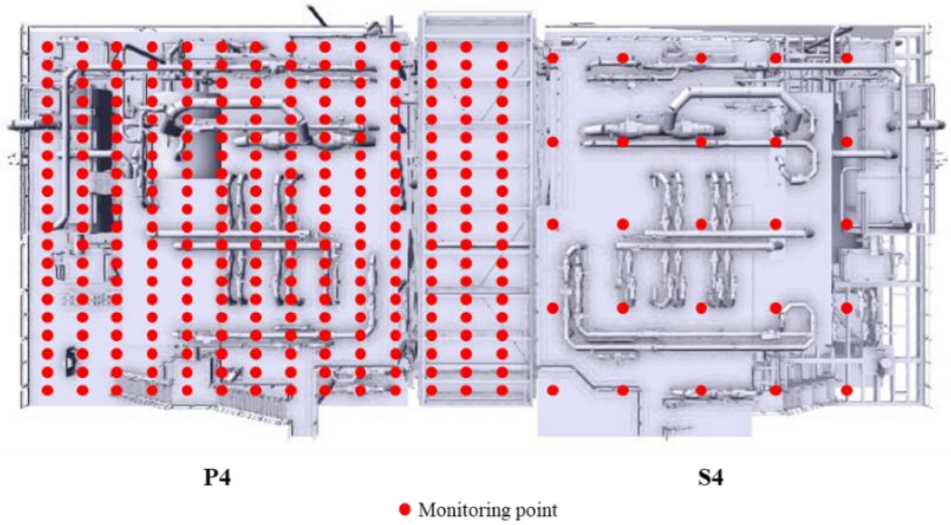

Figure 5.5 Locations of monitoring points between the topside modules and upper deck structure.

(a) Minor release: 1 kg

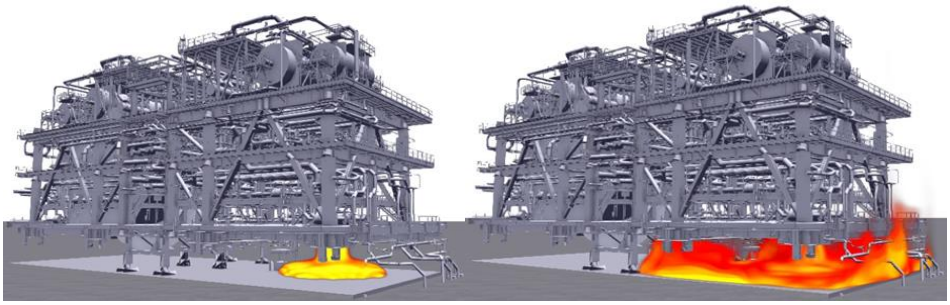

(1) 1 s after ignition (2) 10 s after ignition

(b) Significant release: 100 kg

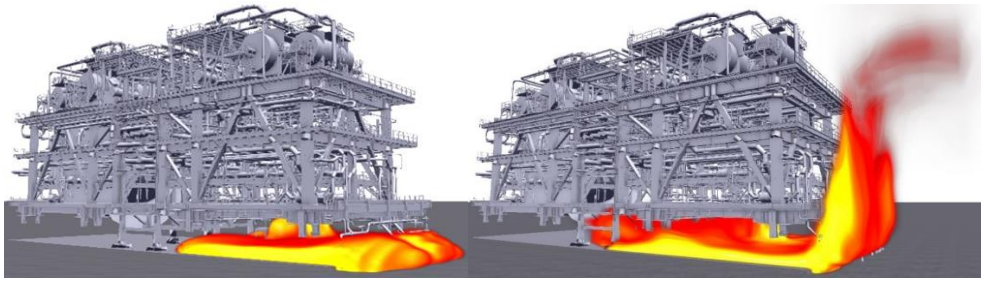

(1) 1 s after ignition (2) 10 s after ignition

(c) Major release: 350 kg

Figure 5.6 Gas cloud temperature distributions between the topside modules and upper deck structure.

5.4 FE Modelling of Upper Deck Structures

The dimensions of the upper deck structures are presented in Figure 5.7 and Table 5.2. HyperMesh (HyperWorks 2017) was used to construct the FE model of the upper deck of the hypothetical FPSO using shell elements. The information on the nodes and elements was written as a k. file that could be read by the LS-PrePost program using the Export_Solver_Deck function. Figure 5.8 shows the constructed FE model. This model was used to simultaneously perform the heat transfer analysis and the structural response

analysis. The FE model consisted of 428,127 nodes and 426,656 shell elements. The mesh size in most regions was 100 mm × 100 mm (Paik 2018), except for certain parts in which smaller meshes were implemented.

In general, early defects are generated in the form of initial deflections and residual stresses during the welding process, which can considerably influence the ultimate strength when a structure is subjected to axial compressive loads. Referring to articles (Paik et al. 2020; Paik et al. 2021a, 2021b; Ryu et al. 2021; Yi et al. 2019, 2020, 2021) which are associated with the present study. Notably, the upper deck structure was subjected to massive lateral patch loads at high temperatures, only the influence of the initial imperfections on the structural collapse in fire events was considered. The plate initial deflection and column-type initial deflection of a stiffener were calculated using the following equations (Paik 2018).

The plate initial deflection was defined as:

$$\frac{w_O}{w_{Opl}} = \sum_{i=1}^{M}\sum_{j=1}^{N} B_{Oij} \sin\frac{i\pi x}{a}\sin\frac{j\pi y}{b},\ w_{Opl} = C_1 b, \tag{5.1}$$

where a and b represent the plate length and breadth, respectively. B_{Oij} indicates the welding-induced initial deflection amplitude normalised by the maximum initial deflection. w_{Opl} can be determined from the initial deflection measurements. Subscripts i and j denote the half-wave numbers in the x and y directions, respectively. $C_1 = 0.005$ was set as the average value for steel plates, based on the definition from Paik (2018).

The column-type initial deflection was defined as:

$$w_O^c = w_{Oc} \sin\frac{\pi x}{a},\ w_{Oc} = C_3 a, \tag{5.2}$$

where w_O^c is the column-type initial distortion of the support members. a is the length of the small stiffeners between two adjacent strong support

members. $C_3 = 0.0015$ was set as the average value for steel plates, based on the definition from Paik (2018).

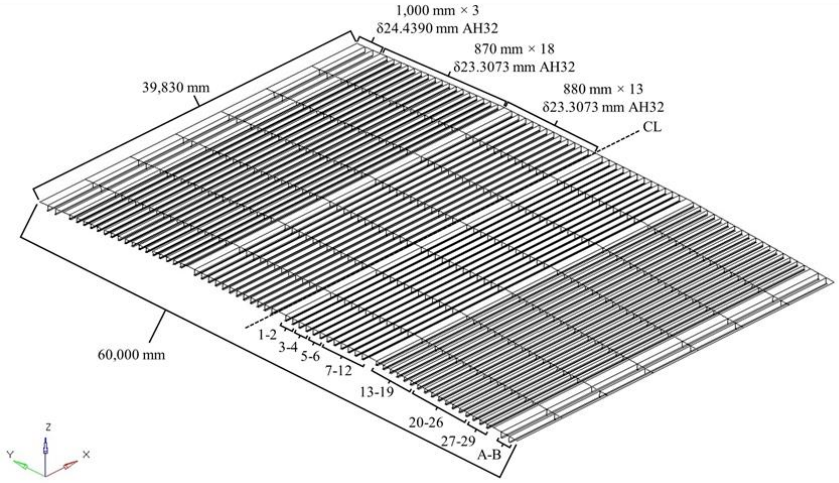

Figure 5.7 Dimensions of the upper deck.

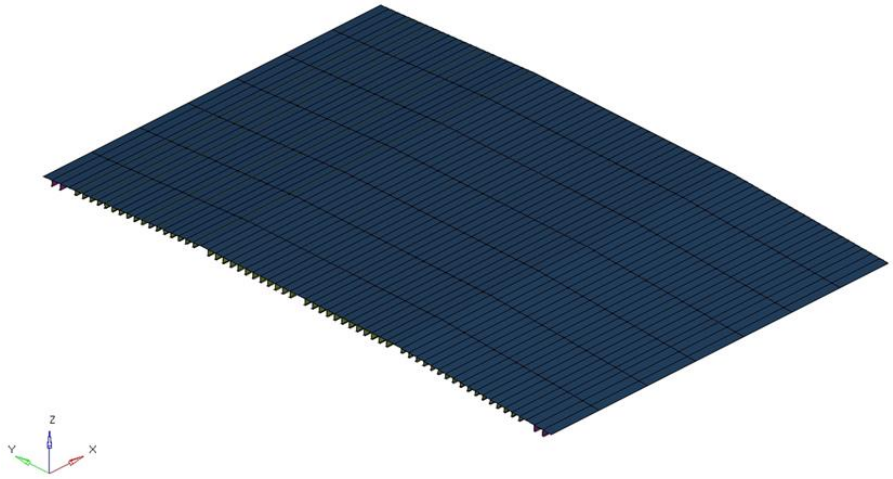

Figure 5.8 Finite element model of the topside structure (upper deck) of the floating, production, storage and offloading unit for the heat transfer and structural response analyses.

Table 5.2 Scantling of longitudinal stiffeners.

Longitudinal stiffener number	Scantling (mm)
1–2, 5–6	600×200×15.611/18.323 (T) AH32
3–4, 7–12	600×200×18/21 (T) AH32
13–19, 27–29	450×200×15.611/18.323 (T) AH32
20–26	450×200×18/21 (T) AH32
A–B	590×150×17.4068/16.323 (IA) AH32

5.5 Gas Cloud Temperature Analysis

As mentioned in previous chapters, a fire CFD simulation was performed using the FLACS code to determine the distribution of the gas cloud temperature. The gas cloud temperature data at the monitoring points, obtained using the FLACS code, were input in the heat transfer analysis to determine the steel temperature. Figure 5.9 shows the maximum gas cloud temperature data obtained in the FLACS simulation for the significant and major release scenarios. Approximately 10 s and 5 s were required to reach the maximum gas cloud temperatures of 1,439 ℃ and 1,497 ℃ for the significant (leak amount of 100 kg) and major (leak amount of 350 kg) scenarios, respectively. Heat loss on the unexposed side was considered along with the heat flux caused by convection and radiation. In addition, owing to the large room volume and adequate ventilation associated with the usual environment for the FPSO structure, the ambient room temperature was considered to be a constant value.

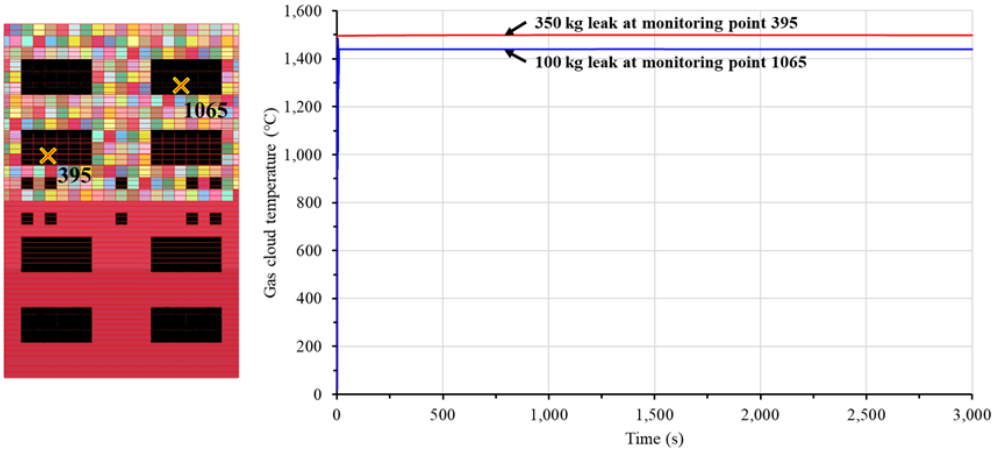

Figure 5.9 Chronology of maximum gas cloud temperature, determined through the FLACS CFD simulation.

5.6 Heat Transfer and Steel Temperature Analyses

5.6.1 Heat Transfer Analysis

Heat flux calculation criteria were established for the heat transfer analysis. The total heat flux was defined as the sum of the heat flux caused by convection and the heat flux caused by radiation. Because the FE model used in this study was composed of shell elements, it was necessary to compute the

heat flux via convection and radiation on both sides, resulting in a total of four calculation terms. The BOUNDARY_FLUX_SET function in LS-PrePost was used to establish the heat flux calculation conditions, which enabled the user to input the convection and radiation coefficients on each side of the shell element. The INITIAL_TEMPERATURE_SET function was used to set the starting temperature of the FE model as 20 °C.

To set the heat flux calculation conditions, the convection and radiation coefficients were defined. The heat transfer via convection between the structural element and surrounding gas cloud, modelled by Cengel and Ghajar (2010), was considered. To define the coefficient of convection (h_c, W/m^{2}K), the convection coefficients for the unexposed and exposed sides were set as h_c = 10 W/m^{2}K and h_c = 19 W/m^{2}K, respectively (Paik et al. 2013). The heat transfer via radiation between the structural element and fire environment, modelled by Franssen and Real (2010), was considered. The radiation emissivity coefficient of steel was set as ε_s = 0.24.

In addition, to obtain accurate results, the thermal properties of steel were clearly defined. The conductivity and specific heat of steel change as the temperature increases, as shown in Figure 2.5 (Section 2.4.1.2).

5.6.2 Steel Temperature Analysis

Figure 5.10 shows the steel temperature distributions after 700 s in the significant and major release scenarios. The fire impact area in the major release scenario (leak amount of 350 kg) was considerably larger than that for the significant release (leak amount of 100 kg) scenario.

As mentioned in Section 5.5, monitoring points 1065 and 395 corresponded to the maximum gas cloud temperature for the scenarios involving leak amounts of 100 kg and 350 kg, respectively. Figure 5.11 presents a comparison of the steel temperature influenced by the maximum gas cloud temperatures for different release levels.

Notably, the thickness of the upper deck plate was not uniform, which led to inconsistent locations for the maximum gas cloud temperature and maximum steel temperature. The maximum steel temperature was observed near monitoring points 191 and 1067. Figure 5.12 shows the gas cloud temperature at monitoring points 191 and 1067 for the significant and major

leak scenarios, and Figure 5.13 shows the comparison of the steel temperature in these two scenarios.

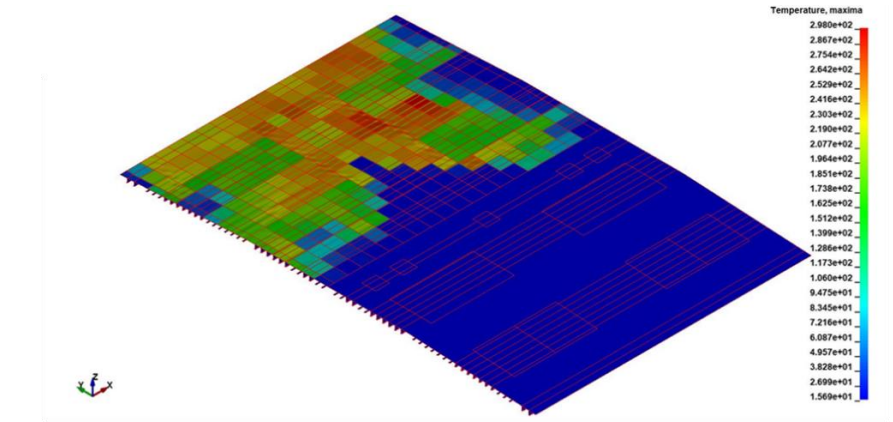

(a)

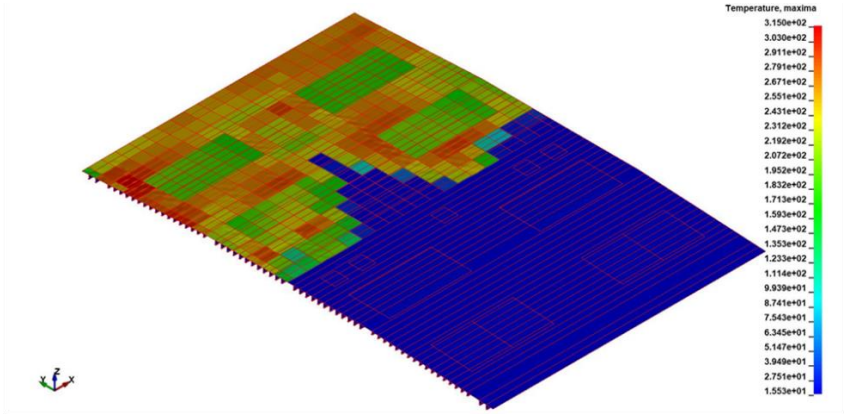

(b)

Figure 5.10 Steel temperature distributions after 700 s: (a) Significant release: 100 kg, (b) major release: 350 kg.

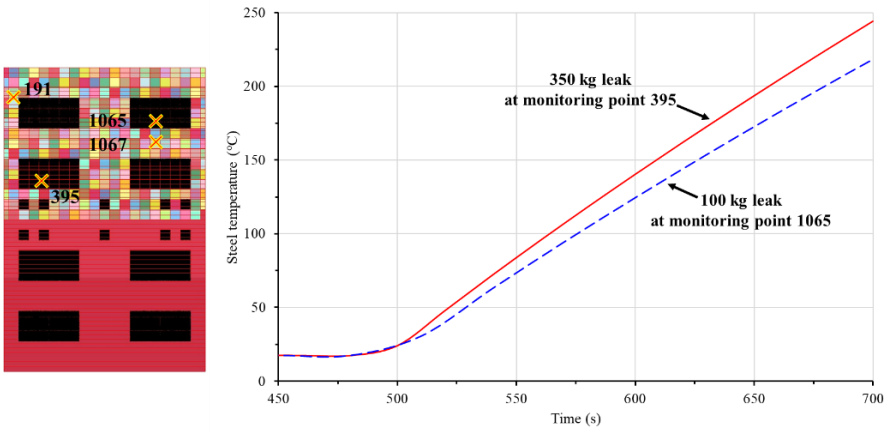

Figure 5.11 Steel temperatures in the significant and major gas leak scenarios, influenced by the maximum gas cloud temperature.

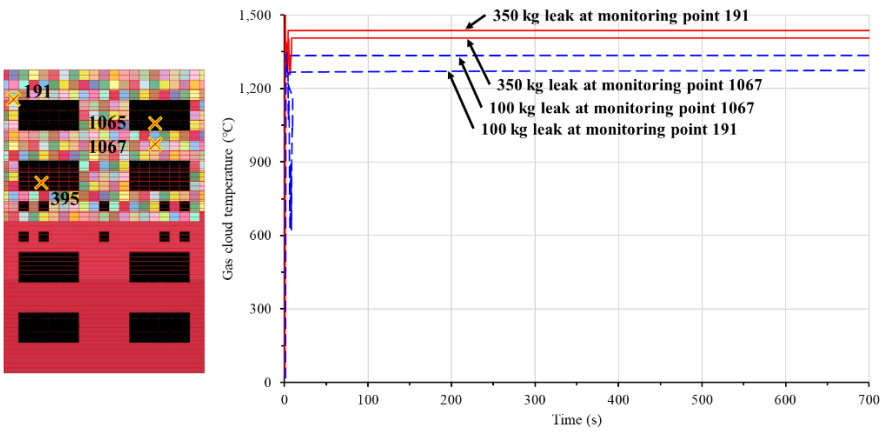

Figure 5.12 Gas cloud temperature at monitoring points 191 and 1067 for the significant and major gas leak scenarios.

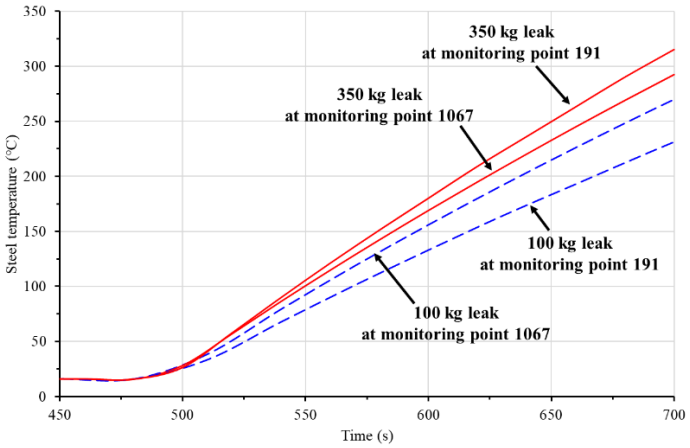

Figure 5.13 Comparison of maximum steel temperature in the significant and major gas leak scenarios.

In the considered case, the transverse frames were not directly exposed to fire; however, heat could still be transferred to the frames from the deck plate structure via conduction. Their temperatures were examined at different distances from the fire impact area. Figure 5.14 shows that the temperature at point A (closer to the fire impact area) is higher than it at point B (further away from the fire impact area), this is obviously due to the heat transfer mechanism associated with conduction. However, the leaked gas was ignited at 500 s and the simulation was terminated at 700 s, which means that the heat conduction process is very short. Besides, the heat loss on the unexposed side (transverse frames side) was also considered in the simulation. Due to the large room volume and adequate ventilation associated with the usual environment for the FPSO structure, the ambient room temperature was

considered to be a constant value (20 ℃). The above-mentioned content may be the reason why the steel temperature of transverse frames is not high. The maximum temperature of the transverse frames was less than 50 ℃, which meant that their mechanical properties were not influenced by the fire. Hence, the structural integrity of the transverse frames was intact. Therefore, passive fire protection (PFP) was not necessary, and the effects of PFP were not considered in the simulation of the fire-induced progressive collapse.

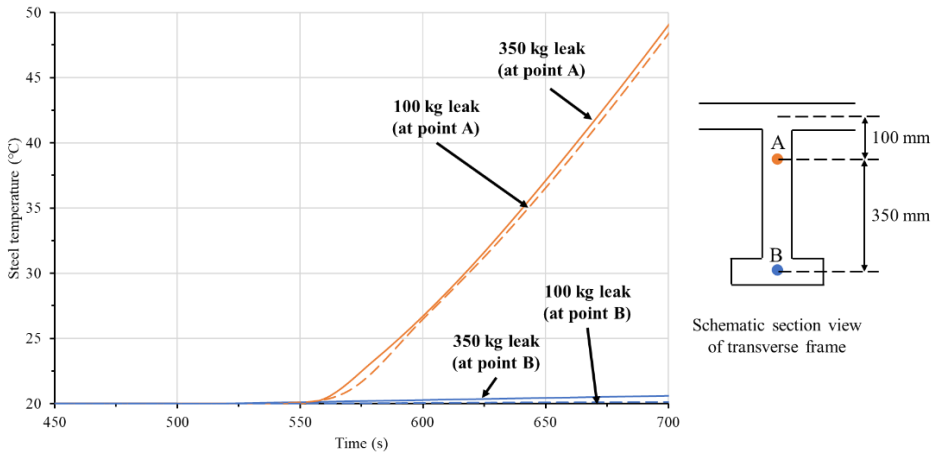

Figure 5.14 Temperature of transverse frames in the significant and major gas leak scenarios.

5.7 Analysis of Fire-Induced Progressive Collapse

5.7.1 Boundary Conditions

To perform the structural response analysis, it is necessary to establish the boundary conditions and set the design loads of the target structure. Moreover, it is necessary to accurately define the mechanical and thermal properties of the material to perform reliable heat transfer and nonlinear structural response analyses.

Figure 5.15 illustrates the boundary conditions used in the LS-DYNA analysis. To set the translational and rotational constraints on the required sections, the BOUNDARY_SPC_SET function was used. As mentioned in Section 5.3, the upper deck of one cargo hold was considered in this study. Hence, the boundary conditions of the upper deck were set corresponding to its contact conditions with the cargo hold. As shown in Figure 5.15, the side in contact with the transverse bulkhead was set as a fixed condition. On the other

side, translational movement in the local z-direction and rotational movement in the local y-direction were constrained. The locations in contact with the longitudinal bulkhead were constrained in the local z-direction and local x-direction in terms of the translational and rotational movements, respectively. The locations in contact with the transverse web sections were constrained in the local z-direction and local y-direction in terms of the translational and rotational movements, respectively.

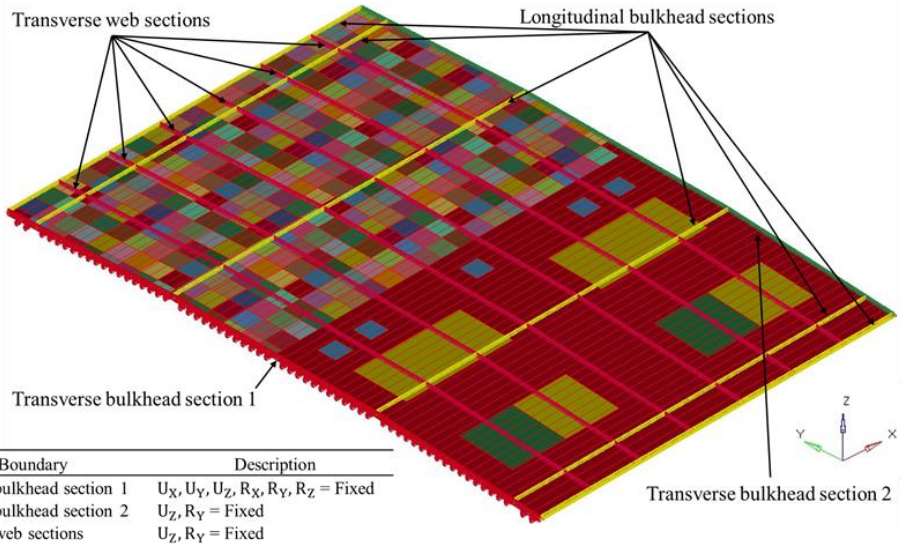

Boundary	Description
Transverse bulkhead section 1	$U_X, U_Y, U_Z, R_X, R_Y, R_Z$ = Fixed
Transverse bulkhead section 2	U_Z, R_Y = Fixed
Transverse web sections	U_Z, R_Y = Fixed
Longitudinal bulkhead sections	U_Z, R_X = Fixed

Figure 5.15 Boundary conditions of the finite element analysis model.

5.7.2 Lateral Patch Loading

In the FE analysis, the lateral patch loads and axial compressive loads applied to the model were specified. The LOAD_BODY_Z function was used to apply the gravitational load, and the LOAD_SEGMENT_SET function was used to apply the lateral patch loads on the required sections. The LOAD_NODE_SET function was used to apply the axial compressive load.

The structural members were in contact with one another. Because of the lateral deformation of the upper deck model, the contact condition was considered to ensure that the node of one member did not penetrate another member and affect the simulation accuracy. The contact condition was assigned using the AUTOMATIC_SINGLE_SURFACE function. The static and dynamic coefficients of friction were set as 0.3 (Paik 2020), as commonly

implemented. The default values for computation with contact surfaces were applied using the CONTROL_CONTACT function.

In ship-building, to strengthen the upper deck to bear the large weight of the topside modules, the thickness of the deck plate and longitudinal stiffeners must be increased. Figure 5.16 shows the plan view of the upper deck, with the locations of the lateral patch loading sections marked in black. The thickness of the deck plate at these sections was set as 36 mm, as commonly used in the FPSO ship-building industry. The area of each patch loading section was 6,000 mm × 6,000 mm, except at the bridge section, which was 2,000 mm × 2,000 mm. In addition, the thickness of the stiffeners under these sections was increased, as indicated in Table 5.2 (longitudinal stiffener numbers 3–4, 7–12, 20–26). The weights of all the topside modules are listed in Table 5.3. Subsequently, the pressure at each loading section could be calculated. Figure 5.17 shows the pressure applied in the local z-direction on different sections in the computational model.

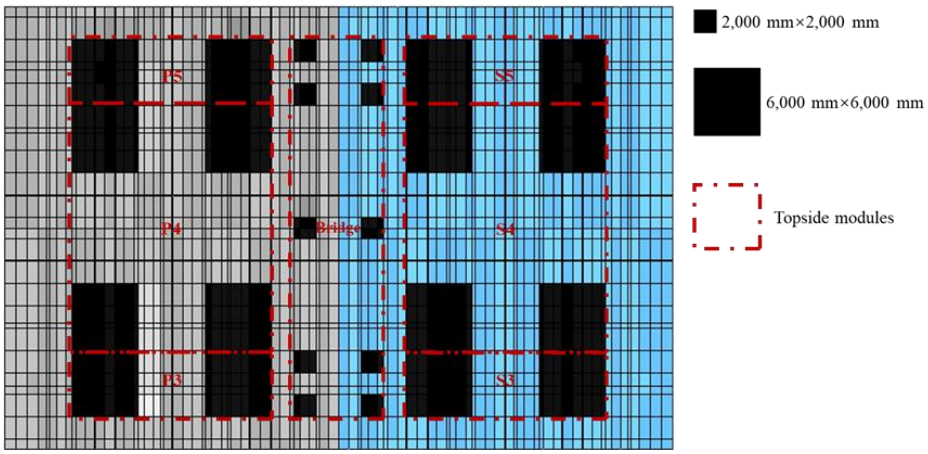

Figure 5.16 Plan view of the upper deck and sizes of the lateral patch stress sections for different topside modules.

Table 5.3 Weights of topside modules.

Topside modules	Weight (ton)
P3+S3	3,500
P4, S4	2,300
P5+S5	3,800
Bridge	20

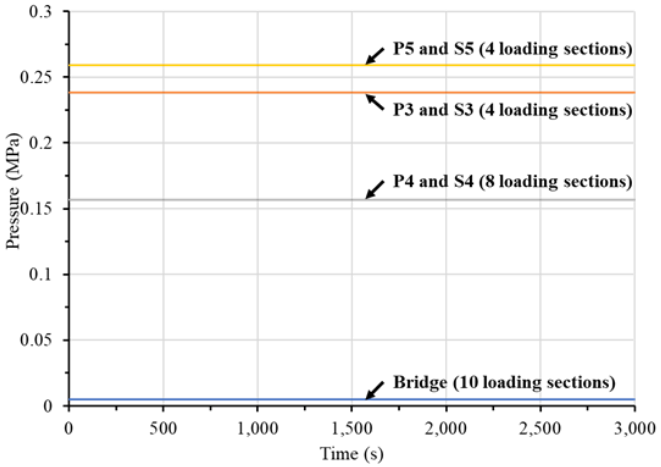

Figure 5.17 Lateral patch stress history for different sections in the computational model.

5.7.3 Axial Compressive Loading

Upper deck structures are subjected to axial compressive loading, which can be attributed to the sagging bending moment of the FPSO hull. Figure 5.18 shows the axial compressive load applied in the local x-direction to the side in contact with the transverse bulkhead in the computational model. The maximum load occurred at 500 s. For the analysis, the calculated axial compressive load was implemented at 500 s. Simultaneously, it was assumed that the leaked gas was ignited at 500 s. Since a constant loading condition is considered, a sufficiently long load increment time is required to identify progressive structural behaviour before the fire occur (500 s). Besides, if the increment time is too long it may cause much longer CPU time. Hence, the 500 s was selected for above purposes. The compressive load was calculated by considering the design vertical bending moments presented in the IACS Common Structural Rules (2021).

The applied axial compressive load was calculated by the formula derived from the simple beam theory:

$$\sigma_b = \frac{My}{I} = \frac{M}{Z} \tag{5.3}$$

where σ_b is the bending stress, M is the total bending moment, y is the distance from the neutral axis, I is the moment of inertia and Z is the section modulus. The section modulus of the present FPSO deck is 90.494 m^3.

The total bending moment acting on the hypothetical FPSO was calculated by the sum of still water bending moment and vertical wave-induced bending moment. Each bending moment was calculated by the IACS Common Structural Rules (IACS 2021) as follows:

The minimum still water bending moment in the sagging condition:

$$M_{SW-S-\min} = -0.85 f_{SW} (171 C_W L^2 B (C_B + 0.7) 10^{-3} + M_{WV-S-\mathrm{mid}}) \qquad (5.4)$$

where f_{SW} is the distribution factor along the ship length L which is 1 for the present study, C_W is the wave coefficient which is 10.75 for the present study, B is the moulded breadth which is 70 for the present study, C_B is the block coefficient which is 0.975 for the present study and $M_{WV-S-\mathrm{mid}}$ is the vertical wave bending moment for strength assessment in sagging conditions. Details about all the values and calculations are available in the IACS Common Structural Rules (2021).

The vertical wave-induced bending moments in sagging condition:

$$M_{WV-S} = -0.19 f_{nl-VS} f_m f_p C_W L^2 B C_B \qquad (5.5)$$

where f_{nl-VS} is the coefficient considering nonlinear effects applied to sagging which is 0.996 for the present study, f_m is the distribution factor for vertical wave bending moment along the ship's length L and f_p is the coefficient for strength assessment, they are all taken as 1 for the present study.

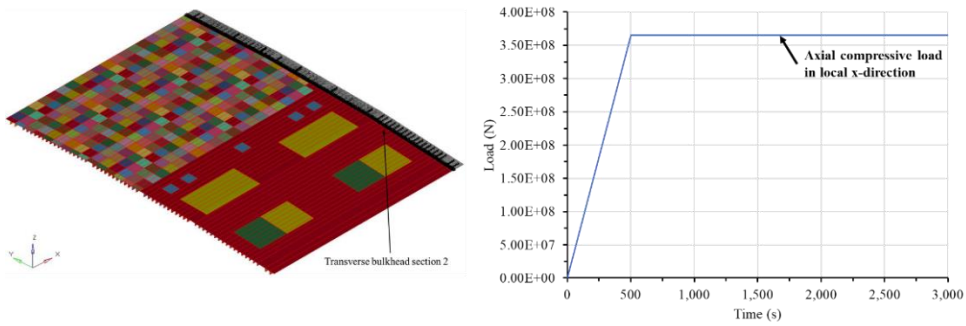

Figure 5.18 Axial compressive load history for the computational model.

5.7.4 Mechanical Properties at Elevated Temperatures

The reduction factor recommended in EN 1993-1-2 (2005) was used to characterise the mechanical characteristics of steel at high temperatures. As mentioned in Section 3.3, the EN 1993-1-2-recommended reduction factor is consistent with the material test data. Figure 3.7 shows the comparison of material properties obtained in tension tests and specified in EN 1993-1-2. The mechanical characteristics of the materials at eight temperature values were specified using the MAT 004-ELASTIC PLASTIC THERMAL function in LS-PrePost. Table 4.3 lists the input values.

5.7.5 Deformed Shapes and Von Mises Stresses

Figure 5.19 shows the deformed shape of the upper deck structure at 700 s. The 350 kg leak causes a more severe deformation than the 100 kg leak. Figure 5.20 shows the von Mises stress distributions at 500 s and 700 s for the two release levels.

Figure 5.21 presents a comparison of the lateral deformation of the most severely deformed section for the significant and major release levels. The 350 kg leak causes a greater lateral deformation than the 100 kg leak. Using the serviceability limit state equation suggested by Paik (2018), the serviceability limit state of the upper deck structure was calculated as 28.45 mm. It is obvious that sections not influenced by the fire did not exhibit any lateral deformation.

$$\frac{L}{200} = \frac{5690}{200} = 28.45\,\text{mm}, \tag{5.6}$$

where L is the span of the beam between supports; in the considered case, $L = 39830 / 7 = 5690\,\text{mm}$.

In the significant scenario (100 kg gas leak), the serviceability limit was reached at approximately 600 s. Because higher temperatures were encountered in the major scenario (350 kg gas leak), the serviceability limit state occurred earlier at approximately 580 s. In addition, sections not influenced by the fire did not exhibit any lateral deformation.

There are numerous criteria for assessing lateral deformation at 20 ℃. Conversely, the focal structure in this study was affected by fire loads; hence, a criterion based on the von Mises stress was used. Figure 5.22 shows the change in the von Mises stress with time at the most severely deformed section, obtained by LS-DYNA. The upper deck structure loses its strength at approximately 600 s and 700 s in the major and significant release scenarios, respectively.

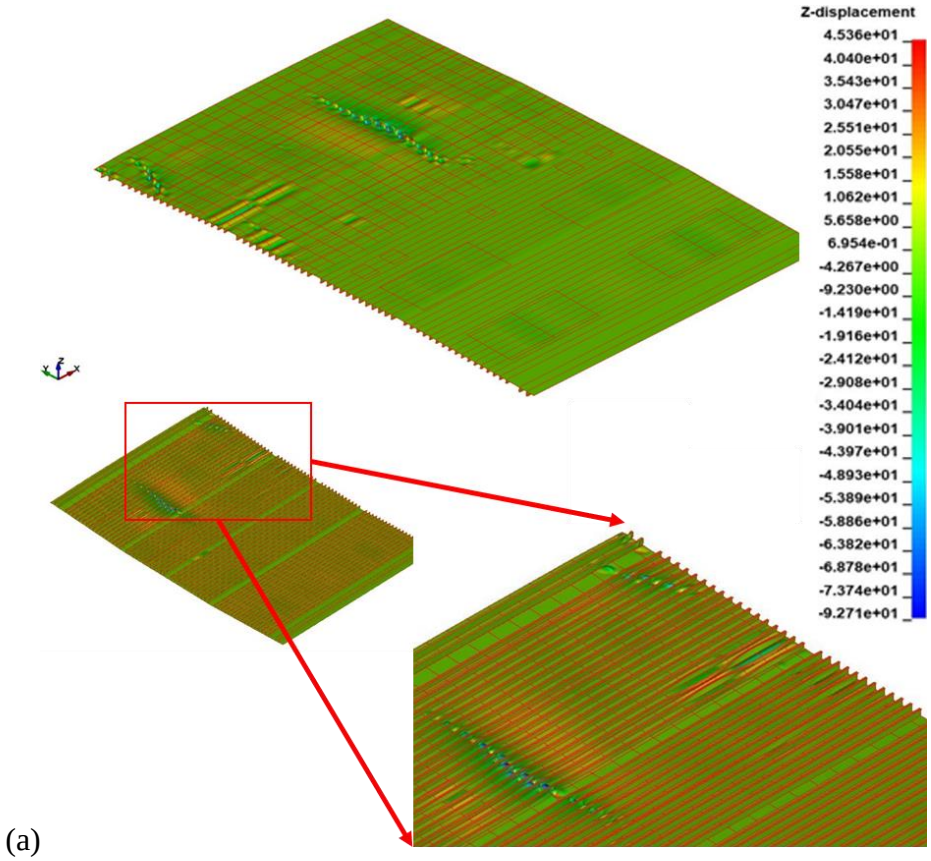

(a)

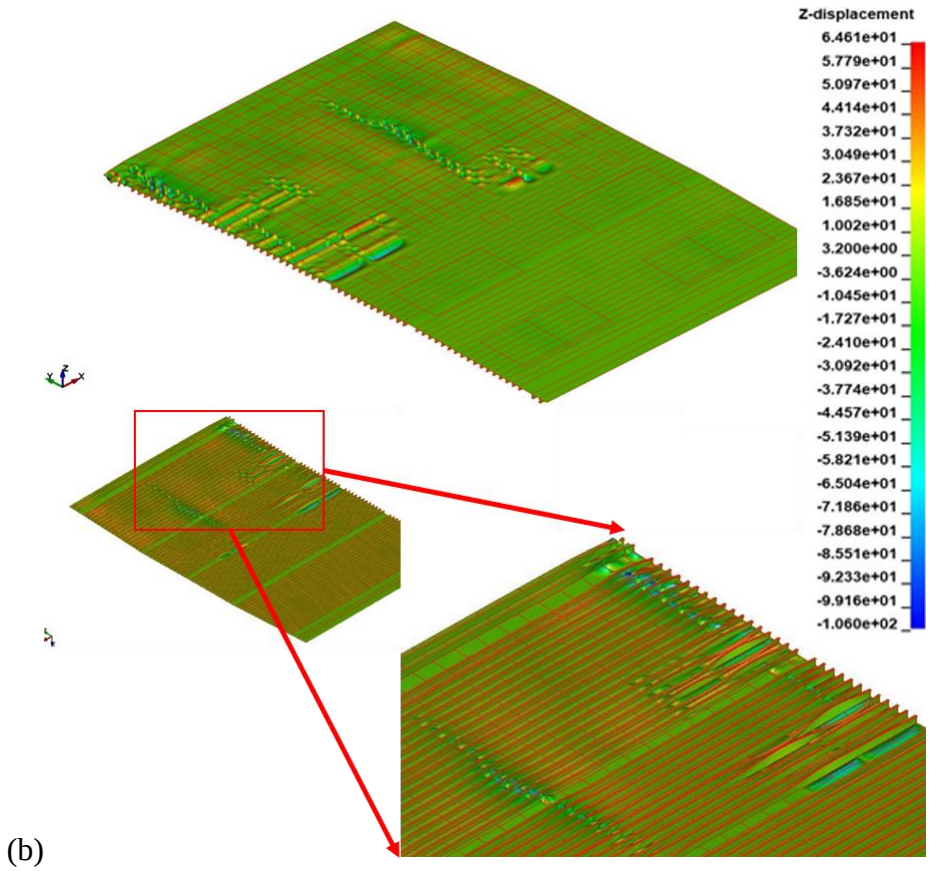

(b)

Figure 5.19 Deformed shapes of the upper deck structure at 700 s: (a) Significant release (100 kg leak), (b) major release (350 kg leak).

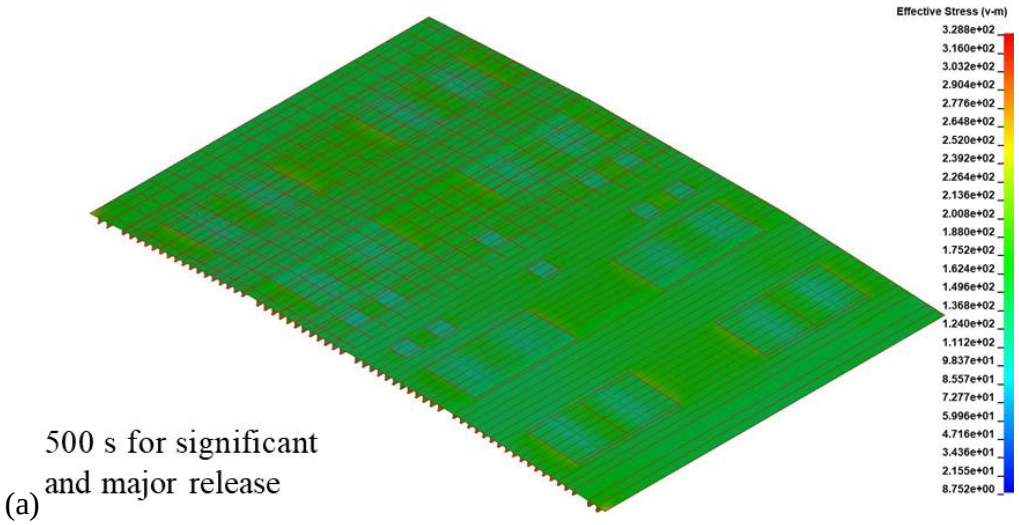

500 s for significant and major release

(a)

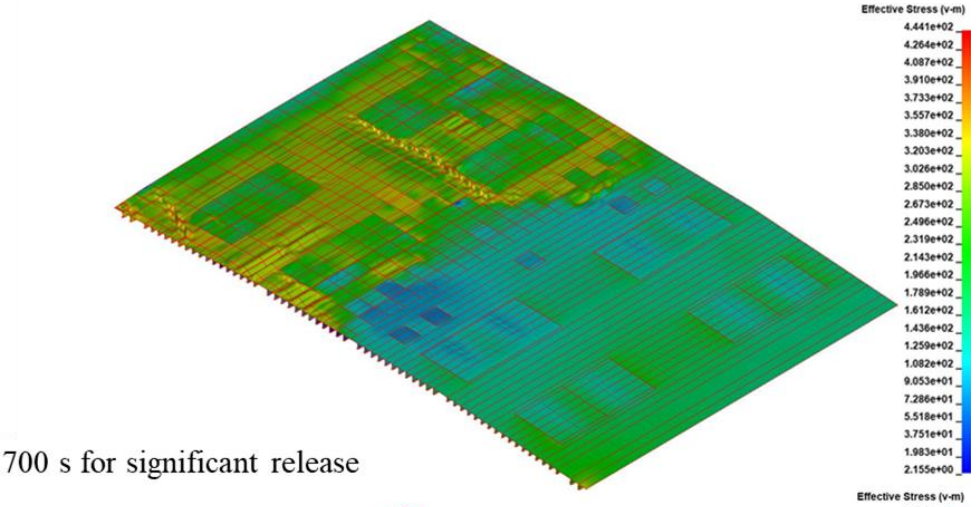

700 s for significant release

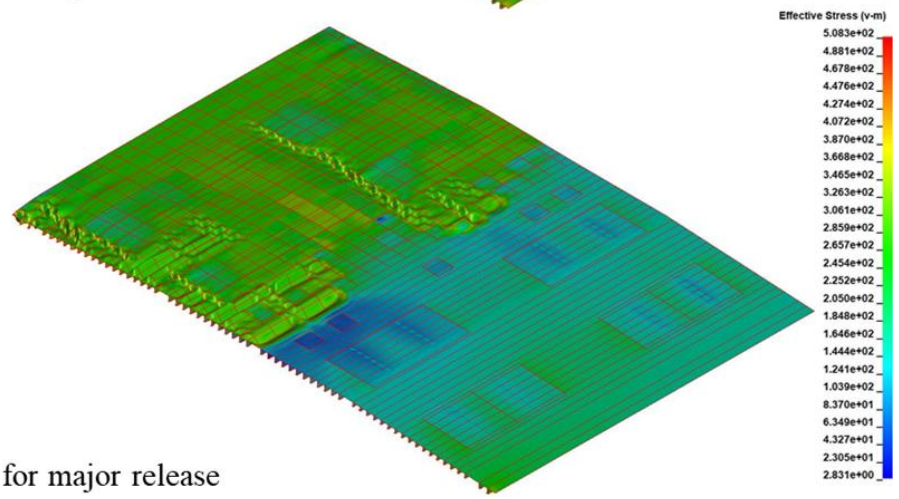

700 s for major release

(b)

Figure 5.20 von Mises stress distribution of the upper deck structure: (a) at 500 s for significant and major release, (b) at 700 s for significant and major release.

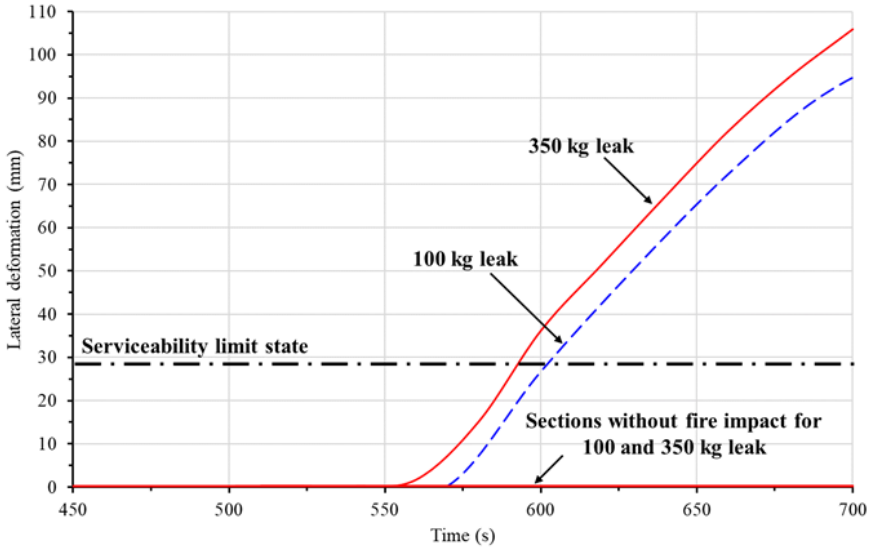

Figure 5.21 Lateral deformation of the most severely deformed section under the significant and major gas release levels versus the serviceability limit state.

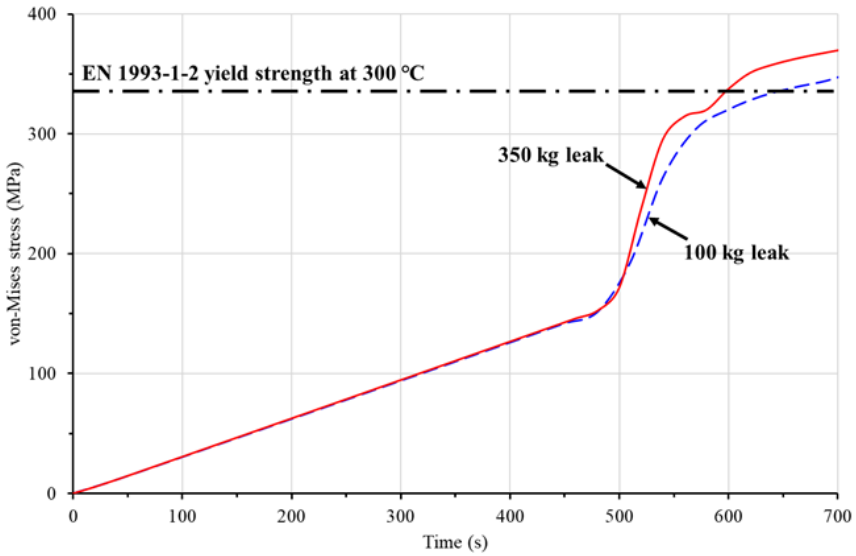

Figure 5.22 von Mises stresses of the most severely deformed section under the significant and major gas release levels versus the EN 1993-1-2 specified yield strength.

5.8 Concluding Remarks

This study demonstrated the applicability of the developed computational models (Chapter 4) for analysing the heat transfer and fire-induced progressive collapse behaviour of the topside structures of ship-shaped offshore installations. CFD simulations involving fire events under three gas release levels were performed. Nonlinear FE-method-based computational modelling

was performed to analyse the heat transfer and the thermal elastic-plastic large-deformation. The following conclusions were derived.

- CFD simulations involving fire events under three gas release levels (minor, significant and major) were performed to obtain the heat flux data and gas cloud dispersion on the upper deck structure of a hypothetical VLCC-class FPSO hull. It was noted that the upper deck was not affected by the fire in the minor release scenario.
- Shell elements were used to model the upper deck structure. The temperature, lateral deformation and von Mises stress results for two types of release scenarios were compared. The modelling technique successfully realised the heat transfer analysis and nonlinear structural response (fire-induced progressive collapse) analysis.
- The temperature of the transverse frames indicated that their mechanical properties were not affected by the fire. Hence, PFP was not necessary for this circumstance. In other scenarios, in which the transverse frames may be exposed to considerably higher temperatures, the mechanical properties may be affected. In such scenarios, PFP must be applied.
- Heat fluxes were transferred from the fire to the surrounding structures via convection and radiation.

Chapter 6 Conclusions and Future Works

6.1 Conclusions

The key research questions are formulated after conducting review surveys on the published work that is relevant to the crashworthiness of structures in fires (Chapter 2). It has been to examine the mechanism of structural crashworthiness of stiffened plate structures commonly used in ships and offshore structures in fires and establish advanced computational models for the fire collapse analysis of stiffened plate structures.

Subsequently, with the help of the designed test jigs, one side of the full-scale physical model of the stiffened plate structure (4.8 m × 7 m) was exposed at an elevated temperature while the other side was subjected to two lateral patch loads at the centre of two transverse frames. The increase of ambient temperature inside the furnace, steel temperatures and lateral deformations were measured during the test. Furthermore, the computational model was developed by using LS-DYNA code. To effectively model the steel structures with PFP, steel and PFP were modelled as shell elements in a single layer in LS-DYNA. The validation of the computational model has been made by comparing its lateral deformation results of transverse frames and temperature results of the plate structure with the experimental results.

In conclusion, to make up for the lack of a test database from large-scale fire testing on steel plated structures, a fire test database on the collapse of full-scale steel stiffened plate structures without or with PFP is acquired from the present study (Chapter 3). Advanced computational models for heat transfer analysis and nonlinear structural response analysis for steel stiffened plate structures without or with PFP are developed and it was validated by comparison with the test data (Chapter 4). Finally, the applicability of developed numerical methods is demonstrated by applying them to a hypothetical VLCC-class floating, production, storage and offloading unit hull structure (Chapter 5).

For academic discipline, the present study presents a fire test database on the collapse of full-scale steel stiffened plate structures without or with PFP for future researchers to validate their computational models. It also presents advanced computational models for structural crashworthiness analysis in fires, the developed computational models will be useful to quantify the fire

consequences within the framework of quantitative risk assessment in association with PFP which is useful for future research methods.

For industrial practices, the present study presents advanced computational models for structural crashworthiness analysis in fires which is helpful in effectively managing fire accidents. Its invention of a realistic approach for analysing the fire-induced progressive collapse of steel plated structures with complex geometries might help with fire safety engineering. This study will be useful for fire-structural analysis procedures and fire safety for offshore constructions in service.

Based on the results of this study, the following conclusions and insights can be drawn.

- Steel temperatures transferred from the heat of gas clouds were measured at monitoring points using thermo-electric couple sensors, as well as gas cloud temperatures inside the furnace for both tests (without and with PFP). The temperatures of transverse frames installed with PFP remained low.
- The time history of the lateral deformations at three monitoring points was measured for both tests and the test data were compared. It was confirmed that PFP is an effective option to delay the collapse of structures in fires.
- The potential application for determining the benefits of PFP in practical applications.
- The test database presented in Appendix can be useful to validate computational models for the structural crashworthiness analysis in fires in association without or with PFP.
- According to the comparisons between numerical results and tests results in Chapter 4, it is justified that modelling the steel structure and PFP as shell elements in a single layer is successful for both the heat transfer analysis and the nonlinear structural response.
- For heat transfer analysis, heat fluxes are transferred from fire to the surrounding structures in association with convection and radiation.
- For structural response analysis, geometric properties and material properties should be defined accurately, as well as loading and boundary conditions.

- For fire safety engineering, not only the fire collapse loads but also the critical period until the collapse is reached should be determined. This critical period is important for establishing the safety scheme of escape and evacuation.
- The proposed procedure can help simulate the structural crashworthiness including structural collapse behaviour in fires.
- To perform a quantitative fire risk assessment, the consequences of the fires must be quantified.
- The proposed methods can help ensure the safety of engineering structures and infrastructures in fire events by quantifying the fire consequences within the framework of quantitative risk assessment.

6.2 Future Works

For other researchers, it is recommended to use the test database presented in this study to validate their computational models for the structural crashworthiness analysis in fires without and with PFP.

Below are some considerations and recommendations for future research that are relevant and important regarding the current study. However, they are not conducted due to time constraints.

The proposed computational methods were applied only to a hypothetical VLCC-class FPSO unit hull topside structure. It would be valuable to extend the analyses to incorporate other ship types, other fire scenarios, and more complex structures (cargo hold). It is anticipated that different ship types and fire scenarios would cause different characteristics of the gas dispersion patterns which may lead to the change of the results of heat transfer analysis and nonlinear structural response analysis. More complex structures are anticipated to have a different critical period until the structure reached the ultimate limit state (or collapse) after the fires started.

In addition, as mentioned in Chapter 5, the FLACS code was used to obtain the gas cloud temperature data at the monitoring locations, which were then used in the heat transfer analysis to determine the steel temperature. However, this process is time-consuming. The more monitoring points there are, the more gas cloud temperature data there will be, resulting in a longer data import time. Further research should be carried out to shorten this time or allow data to be imported automatically, which should be easy to use and

easily accessible. In this way, unnecessary time-consuming can be shortened, and researchers can obtain analysis results more conveniently and timely.

The temperature of the transverse frames in this study suggested that the fire did not affect their mechanical properties (Chapter 5). As a result, PFP was not necessary for this situation. Conversely, in other scenarios, the mechanical properties of the transverse frames may be changed if they are exposed to much greater temperatures. PFP must be applied in such situations. Further studies can be conducted to apply the developed computational models to realistic steel plated structures in fires where PFP effects should be investigated. In such instances, it is expected that the PFP will be able to successfully delay the structural collapse.

References

ABS (2014). Guidance noted in fire-fighting systems. American Bureau of Shipping, Texas.

Ahmad A, Hassan SA, Ripin A, Ali MW, Haron S (2013). A risk-based method for determining passive fire protection adequacy. Fire Saf J. 58:160—169.

ANSYS (2021). LS-DYNA keyword user's manual Volume I. Livermore Software Technology (LST), California, CA.

AS 1530 (2014). Methods for fire tests on building materials, components and structures—part 4: fire-resistance test of element of construction. Standards Australia, Australia.

ASTM International (2020). Standard test methods for elevated temperature tension testing of metallic materials & standard test methods for tension testing of metallic materials. American Association State, West Conshohocken, PA.

Bradley I, Willoughby D, Royle M (2019). A review of the applicability of the jet fire resistance test of passive fire protection materials to a range of release scenarios. Process Saf Environ Prot. 122:185—191.

British Steel Corporation (1987). Compendium of UK standard fire test data on unprotected structural steel, Report No. RS/RSC/S10328/1/87/B. North Lincolnshire.

BS (2014). BS 476-20: Fire tests on building materials and structures – part 20: method for determination of the fire resistance of element of construction (general principles). British Steel Institute, London.

Celnik M, Murray P (2016). Risk-based fire engineering for offshore installations. DNV GL, Hazards 26, NO. 161.

Cengel YA, Ghajar AJ (2010). Heat and mass transfer (in SI units): fundamentals and applications, 4th Edition. McGraw-Hill, Columbus, OH.

Cong S, Liang S, Dong Y (2005). Experimental investigation of behavior of simply supported steel beams under fire. Journal of Southeast University (Natural Science Edition), 35: 66—68 (in Chinese).

Cozzani V, Tugnoli A, Salzano E (2006). Prevention of domino effect: from active and passive strategies to inherently safer design. J Hazard

Mater. 139:209—219.

Czujko J, Paik JK (2012a). Hydrocarbon explosion and fire engineering-assessing and managing hydrocarbon explosion and fire risks in offshore installations. Marine Technology, SNAME, pp.23—25.

Czujko J, Paik JK (2012b). Paradigm change in safety design against hydrocarbon explosions and fires. FABIG Newsletter, Issue 60, pp.20—38.

DIFK (2014). Determination of thermal conductivity-ASTM, KCC cerawool new-bio alpha 1200, Test Report 105-218-00-01. Deutsches Institut für Feuerfest und Keramik GmbH, Rheinstrasse, Höhr-Grenzhausen.

DNV (2010). Design against accidental loads. Recommended practice DNV-RP-C204, Det Norske Veritas, Norway.

DNV (2011). Design of offshore steel structures. General (LRFD Method), Oslo.

DNV (2018). LNG regulatory update. http://www.golng.eu/files/Main/20180417/2.%20Ole%20Vidar%20Nilsen%20-%20DNV%20GL.pdf. Accessed by 15 July 2019.

EMSA (2019). Annual overview of marine casualties and incidents. Praca Europa. 4:1249—1206, European Maritime Safety Agency, Lisbon.

EN 1993-1-2 (2005). Eurocode 3: Design of steel structures—Part 1-2: General Rules-Structural fire design. European Standard, Brussels.

FLACS (2021). User's manual V10.7. Global Explosion Consultants, Bergen.

Franssen JM, Real PV (2010). Fire design of steel structures. ECCS Eurocode design manuals, Ernst & Sohn, Berlin.

Friebe M, Jang BS, Jim Y (2014). A parametric study on the use of passive fire protection in FPSO topside module. Int J Naval Arch Ocean Eng. 6:826—839.

Fu F (2020). Fire induced progressive collapse potential assessment of steel frames building using machine learning. Journal of Constructional Steel Research, 166: 105918.

Gernay T, Gamba A (2018). Progressive collapse triggered by fire induced column loss: detrimental effect of thermal forces. Engineering Structures, 172: 483—496.

He KH, Kim HJ, Thomas G, Paik JK (2022). Analysis of fire-induced progressive collapse for topside structures of a VLCC-class ship-shaped offshore installation. Ships and Offshore Structures, DOI: 10.1080/17445302.2022.2027681.

Hirdaris SE, Bai W, Dessi D, Ergin A, Gue X, Hermundstad OA, Huijsmans R, Iijima K, Nielsen UD, Parunov J, Fonseca N, Papanikolaou A, Argyriadism K, Incecik A (2015). Loads for use in the design of ships and offshore structures. Ocean Eng. 78 131—174.

HSE (2000). Review of the response of pressurised process vessels and equipment to fire attack. Offshore Technology Report - OTO 2000 051, Health and Safety Executive, London.

HSE (2005). Accident statistics for floating offshore units on the UK continental shelf (1980–2003). HMSO RR 353, Health and Safety Executive, London.

HSE (2017). Offshore accident and failure frequency data sources – review and recommendations. Research Report RR1114, Health and Safety Executive, Derbyshire, UK.

HyperWorks (2017). HyperMesh 2017 user guide. Altair Engineering Inc., Troy, Michigan.

IACS-CSR (2021). Common structural rules for bulk carriers and oil tankers. International Association of Classification Societies, London.

ISO 834 (1999). Fire resistance tests—elements of buildings constructions—part 1: general requirement. International Organization for Standardization, Geneva.

ISO/TR 13387-1 (1999). Fire Safety Engineering—Part 1: Application of fire performance concepts to design objectives technical report. International Organization for Standardization, Geneva.

Kim JH (2014). A new procedure for fire structural assessment of offshore installations. Pusan National University, Busan.

Kim JH, Kim DC, Kim CK, Islam MS, Park SI, Paik JK (2013). A study on methods for fire load application with passive fire protection effects. Ocean Eng. 70:177—187.

Kim SJ, Lee J, Paik JK, Jung, Seo JK, Shin WH, Park JS (2016). A study on fire design accidental loads for aluminum safety helidecks.

International Journal of Naval Architecture and Ocean Engineering 8: 519—529.

Kumar W, Sharma UK, Shome M (2021). Mechanical properties of conventional structural steel and fire-resistant steel at elevated temperatures. Journal of Constructional Steel Research, 181:106615.

Landucci G, Rossi F, Nicolella C, Zanelli S (2009). Design and testing of innovative materials for passive fire protection. Fire Saf J. 44(8):1103—1109.

Lim JW, Baalisampang T, Garaniya V, Abbassi R, Khan F, Ji J (2019). Numerical analysis of performances of passive fire protections in processing facilities. J Loss Prev Process Ind. 62:103970.

Lou G, Wang C, Jiang J, Jiang Y, Wang L, Li G (2018). Fire tests on full-scale steel portal frames against progressive collapse. Journal of Constructional Steel Research, 145: 137—152.

LR (2014). Rules and regulations for the classification of offshore units: Guidelines for the calculation of probabilistic explosion loads. Lloyd's Register, Southampton.

LS-DYNA (2019). User's manual for LS-DYNA, Version 970. Livermore Software Technology Corporation, CA.

LS-PrePost (2020). LS-PrePost User's Manual – An advanced pre and post processor and model editor for LS-DYNA, Version 4.7. Livermore Software Technology Corporation, CA.

Maraveas C (2019). Local buckling of steel members under fire conditions: a review. Fire Technology, 55:51—80.

Mroz K, Hager I, Korniejenko K (2016). Material solutions for passive fire protection of buildings and structures and their performances testing. Proc Eng. 151:284—291.

NEPA-921 (2017). Guide for fire and explosion investigations. National Fire Protection Gaithersburg, MD.

NIST (2018). National Institute of Standards and Technology. U.S. Department of Commerce, Gaithersburg, MD.

NORSOK (2010). Standard Z-013: Risk and emergency preparedness assessment (thirded). NORSOK, Oslo.

Paik JK (2015). Making the case for adding variety to Goal-Based Standards. The Naval Architect, The Royal Institution of Naval Architects, London.

Paik JK (2018). Ultimate limit state analysis and design of plated structures, 2nd Edition. John Wiley & Sons, Chichester.

Paik JK (2020). Advanced structural safety studies with extreme conditions and accidents. Springer, Singapore.

Paik JK (2022). Ship-shaped offshore installations: design, construction, operation, healthcare and decommissioning, 2nd Edition. Cambridge University Press, Cambridge.

Paik JK, Kim JH, Park SI, Islam S, Lee DH (2013). A new procedure for the nonlinear structural response analysis of offshore installations in fires. SNAME Maritime Convention, Bellevue, WA.

Paik JK, Lee DH, Noh SH, Park DK, Ringsberg JW (2020). Full-scale collapse testing of a steel stiffened plate structure under axial-compressive loading triggered by brittle fracture at cryogenic condition. Marine Science and Application, 4: 658—673.

Paik JK, Lee DH, Noh SH, Park DK, Ringsberg JW (2020). Full-scale collapse testing of a steel stiffened plate structure under cyclic axial-compressive loading. Structures, 26: 996—1009.

Paik JK, Lee DH, Park DK, Ringsberg JW (2020). Full-scale collapse testing of a steel stiffened plate structure under axial-compressive loading at a temperature of -80^{o}C. Ships and Offshore Structures, 16(3): 255—270.

Paik JK, Ryu MG, He KH, Lee DH, Lee SY, Park DK, Thomas G (2021a). Full-scale fire testing to collapse of steel stiffened plate structures under lateral patch loading (part 1)–without passive fire protection. Ships and Offshore Structures, 16(3): 227—242.

Paik JK, Ryu MG, He KH, Lee DH, Lee SY, Park DK, Thomas G (2021b). Full-scale fire testing to collapse of steel stiffened plate structures under lateral patch loading (part 2)–with passive fire protection. Ships and Offshore Structures, 16(3): 243—254.

Paik JK, Thayamballi AK (2013). Ultimate limit state design of steel-plated structures. Wiley, Chichester.

Park DK, Kim JH, Park JS, Ha YC, Seo JK (2021). Effects of the structural strength of fire protection insulation systems in offshore installations. International Journal of Naval Architecture and Ocean Engineering, 13:493—510.

Parthasarathi N, Thiagarajan K, Satyanarayanan KS, Thamilarasu V (2018). Nonlinear analysis of the progressive collapse for two-dimensional steel frame under fire conditions. Materialstoday Proceedings, 5(2:3): 8718—8726.

Purkis JA (2006). Fire safety engineering—design of structures, 2nd Edition. Elsevier, New York.

Rahmanian I, Wang Y (2009). Thermal conductivity of gypsum at high temperatures. Acta Polytechnica 49:16—20.

Roberts TA, Shirvill LC, Waterton K, Buckland I (2010). Fire resistance of passive fire protection coatings after long-term weathering. Process Saf Environ Prot. 88:1—19.

Ryu MG, He KH, Lee DH, Park SI, Thomas G, Paik JK (2021). Finite element modeling for the progressive collapse analysis of steel stiffened-plate structures in fires. Thin-Walled Structures, 159: 107262.

Shallcross DC (2013). Using concept maps to assess learning of safety case studies – The Piper Alpha disaster. Education for Chemical Engineers, 8(1): e1—e11.

Shan S, Li S (2020). Fire-induced progressive collapse mechanisms of steel frames with partial infill walls. Structures, 25: 347—359.

Shan S, Li S, Wang S, Sezen H, Kose HM (2019). Influence of masonry infill walls on fire-induced collapse mechanisms of steel frames. Journal of Constructional Steel Research, 155: 426—437.

Shetty NK, Soares CG, Jensen FM (1998). Fire safety assessment and optimal design of passive fire protection for offshore structures. Reliab Eng Syst Saf. 61(1–2):139—149.

Spouge J (1999). A guide to quantitative risk assessment for offshore installations. The Centre for Marine and Petroleum Technology, London.

Sun R, Huang Z, Burgess IW (2012). Progressive collapse analysis of steel structures under fire conditions. Engineering Structures, 34: 400—

413.

Suwondo R, Cunningham L, Gillie M, Bailey C (2019). Progressive collapse analysis of composite steel frames subject to fire following earthquake. Fire Safety Journal, 103: 49—58.

Van den Boogaard AH, Meinders T, Hu´etink J (2003). Efficient Implicit FEM Simulations of Sheet Metal Forming. VII International Conference on Computational Plasticity, COMPLAS, Barcelona.

Wainman DE, Kirby BR (1987). Compendium of UK standard fire test data on unprotected structural steel-1, Report No. RS/RSC/S10328/1/87/B. British Steel Corporation, Rotherham.

Yin F, Song ZB, He ZW, Qin BY, John GF, Zhang L, Su PH, Zhang WS, Yang T (2022). Chemical fingerprinting and characterization of spilled oils and burnt soot particles – A case study on the Sanchi oil tanker collision in the East China Sea. Science of The Total Environment, 824: 153896.

Yi MS, Hyun CM, Paik JK (2019). An empirical formulation for predicting welding-induced biaxial compressive residual stresses on steel stiffened plate structures and its application to thermal plate buckling prevention. Ships and Offshore Structures, 14(S1): S18—S33.

Yi MS, Lee DH, Lee HH, Paik JK (2020). Direct measurement and numerical predictions of welding-induced initial deformations in a full-scale steel stiffened plate structure. Thin-Walled Structures, 164: 107889.

Yi MS, Noh SH, Lee DH, Seo DH, Paik JK (2021). Direct measurements, numerical predictions and simple formula estimations of welding-induced biaxial residual stresses in a full-scale steel stiffened plate structure. Structures, 29: 2094—2105.

Appendix. Test Databases

Tables in this chapter provide all the useful test databases obtained from the two fire tests, which can be used to validate computational models for the fire collapse analysis for the test structures with and without PFP.

A.1 Thermal Conductivity of Carbon Steel as Shown in Figure 2.5

Temperature (°C)	Conductivity (W/mK)
20	53.3
100	50.7
200	47.3
300	44.0
400	40.7
500	37.3
600	34.0
700	30.7
701	30.7
702	30.6
703	30.6
704	30.6
705	30.5
706	30.5
707	30.5
708	30.4
709	30.4
710	30.4
711	30.3
712	30.3
713	30.3
714	30.2
715	30.2
716	30.2
717	30.1
718	30.1
719	30.1
720	30.0
721	30.0
722	30.0
723	29.9
724	29.9
725	29.9
726	29.8
727	29.8
728	29.8
729	29.7
730	29.7
731	29.7

Temperature (°C)	Conductivity (W/mK)
732	29.6
733	29.6
734	29.6
735	29.5
736	29.5
737	29.5
738	29.4
739	29.4
740	29.4
741	29.3
742	29.3
743	29.3
744	29.2
745	29.2
746	29.2
747	29.1
748	29.1
749	29.1
750	29.0
751	29.0
752	29.0
753	28.9
754	28.9
755	28.9
756	28.8
757	28.8
758	28.8
759	28.7
760	28.7
761	28.7
762	28.6
763	28.6
764	28.6
765	28.5
766	28.5
767	28.5
768	28.4
769	28.4
770	28.4

Temperature (°C)	Conductivity (W/mK)
771	28.3
772	28.3
773	28.3
774	28.2
775	28.2
776	28.2
777	28.1
778	28.1
779	28.1
780	28.0
781	28.0
782	28.0
783	27.9
784	27.9
785	27.9
786	27.8
787	27.8

Temperature (°C)	Conductivity (W/mK)
788	27.8
789	27.7
790	27.7
791	27.7
792	27.6
793	27.6
794	27.6
795	27.5
796	27.5
797	27.5
798	27.4
799	27.4
800	27.3
900	27.3
1000	27.3
1100	27.3
1200	27.3

A.2 Specific Heat of Carbon Steel as Shown in Figure 2.5

Temperature (°C)	Specific heat (J/KgK)
0	440
20	440
21	440
21.9	441
23	442
24.4	443
25.9	444
29.3	446
33	449
35.1	450
37.2	452
39.4	453
41.8	455
44.2	456
46.7	458
49.3	459
51.8	461
57	464
59.6	466
62.2	467
64.8	469
67.4	470
70.1	472
72.8	473

Temperature (°C)	Specific heat (J/KgK)
75.4	475
78.1	476
80.8	478
83.5	479
86.2	481
91.6	483
96.9	486
102	489
105	490
107	491
110	493
113	494
115	495
123	499
131	502
136	504
141	507
148	510
156	513
158	514
163	516
168	518
175	520
182	523

Temperature (°C)	Specific heat (J/KgK)
189	526
196	528
205	532
209	533
214	535
218	536
220	537
228	540
235	542
239	543
246	546
252	548
260	551
265	553
271	554
276	556
283	559
290	561
293	562
298	564
303	566
306	567
310	568
313	570
316	571
319	572
325	574
328	575
331	576
334	577
338	579
340	580
342	581
347	582
352	585
354	585
359	588
373	593
381	597
385	599
390	601
395	604
400	606
405	608
408	610
414	613
415	614

Temperature (°C)	Specific heat (J/KgK)
418	615
420	616
423	618
427	620
437	625
438	626
440	627
442	628
444	629
450	633
455	636
458	638
460	639
463	641
466	643
470	645
472	647
474	648
477	650
480	652
484	655
490	659
496	663
502	668
506	671
511	675
514	678
520	682
524	686
528	689
532	692
534	694
536	696
541	700
544	703
552	710
557	715
561	719
575	733
586	744
592	751
599	759
603	762
605	764
609	767
613	770
620	776

Temperature (°C)	Specific heat (J/KgK)
632	789
642	802
644	804
651	816
658	828
660	832
665	844
672	864
676	875
682	898
685	910
687	921
690	939
694	960
697	985
700	1010
701	1020
702	1030
703	1040
704	1050
705	1060
706	1070
707	1090
708	1100
709	1110
710	1130
711	1150
712	1170
713	1190
714	1210
715	1230
716	1260
717	1290
718	1320
719	1350
720	1390
721	1430
722	1480
723	1530
724	1590
725	1670
726	1750
727	1850
728	1970
729	2110
730	2290
731	2520

Temperature (°C)	Specific heat (J/KgK)
732	2830
733	3270
734	3920
735	5000
736	4110
737	3520
738	3090
739	2770
740	2530
741	2330
742	2170
743	2030
744	1920
745	1820
746	1730
747	1660
748	1590
749	1540
750	1480
751	1440
752	1390
753	1360
754	1320
755	1290
756	1260
757	1230
758	1210
759	1180
760	1160
761	1140
762	1120
763	1100
764	1090
765	1070
766	1050
767	1040
768	1030
769	1010
770	1000
771	991
772	980
773	969
774	959
775	950
776	941
777	932
778	924

Temperature (°C)	Specific heat (J/KgK)
779	916
780	909
781	901
782	894
783	888
784	881
785	875
786	869
787	863
788	858
789	852
790	847
791	842

Temperature (°C)	Specific heat (J/KgK)
792	837
793	832
794	828
795	823
796	819
797	815
798	811
799	807
800	803
900	650
1000	650
1100	650
1200	650

A.3 Thermal Conductivity of Cerawool as Shown in Figure 3.15

Temperature (°C)	Conductivity (W/mK)
0	0.043
200	0.058
400	0.097
600	0.154
800	0.23100001
1000	0.33399999
1100	0.39399999

A.4 Applied Lateral Patch Loads for Two Fire Tests as Shown in Figure 3.24

Time (s)	Load for the fire test without PFP (tf)	Load for the fire test with PFP (tf)
0	15	15
1580	15	15
1591	0	15
1601	0	0
1611	18	2
1621	47	13
1631	50	28
1641	50	42

Time (s)	Load for the fire test without PFP (tf)	Load for the fire test with PFP (tf)
1651	50	49
1661	50	50
2631	50	50
2641	0	50
3091	0	50
3101	0	75
3252	0	75
3262	0	0

A.5 Maximum Gas Cloud Temperature for Two Fire Tests as Shown in Figure 4.6

Time (s)	Gas temperature for the fire test without PFP (°C)	Gas temperature for the fire test with PFP (°C)
0	27	16
10	87	95
20	135	156
30	203	237
40	261	321
50	330	401
60	380	459
70	431	500
80	461	519
90	496	529
100	521	531
110	543	528
120	563	524
130	578	520
140	595	520
150	611	522
160	625	530
170	634	538
180	645	547
190	652	557
200	659	568
210	666	578
220	673	590
230	676	602
240	681	616
250	685	632
260	688	641
270	690	656
280	694	666
290	697	682
300	698	693
310	700	704
320	706	712
330	712	720
340	716	727
350	718	730
360	721	734
370	722	737
380	723	741
390	721	746
400	719	751
410	718	755

Time (s)	Gas temperature for the fire test without PFP (°C)	Gas temperature for the fire test with PFP (°C)
420	719	757
430	719	759
440	718	760
450	718	761
460	718	762
470	717	765
480	716	767
490	714	768
500	712	770
510	712	773
520	710	775
530	709	776
540	707	777
550	706	775
560	703	776
570	701	773
580	698	768
590	696	760
600	695	750
610	693	746
620	691	743
630	689	739
640	688	736
650	687	731
660	686	726
670	685	722
680	684	722
690	684	724
700	683	729
710	682	736
720	681	742
730	682	748
740	682	752
750	683	756
760	684	758
770	685	756
780	686	751
790	687	747
800	687	743
810	686	741
820	686	739
830	686	737

Time (s)	Gas temperature for the fire test without PFP (°C)	Gas temperature for the fire test with PFP (°C)
840	687	736
850	688	734
860	689	734
870	690	733
880	691	731
890	693	731
900	695	730
910	696	730
920	696	733
930	696	734
940	697	735
950	698	736
960	699	737
970	700	738
980	701	739
990	702	740
1000	702	741
1010	703	741
1020	705	737
1030	706	730
1040	706	725
1050	707	724
1060	707	723
1070	708	724
1080	709	727
1090	709	728
1100	711	730
1110	712	730
1120	712	731
1130	713	734
1140	714	736
1150	714	739
1160	716	741
1170	717	743
1180	718	744
1190	719	745
1200	720	746
1210	721	746
1220	722	746
1230	723	746
1240	724	746
1250	725	745
1260	726	744
1270	727	744
1280	728	744

Time (s)	Gas temperature for the fire test without PFP (°C)	Gas temperature for the fire test with PFP (°C)
1290	729	744
1300	729	744
1310	729	747
1320	729	752
1330	730	755
1340	731	760
1350	732	763
1360	733	765
1370	734	768
1380	735	768
1390	736	771
1400	737	772
1410	739	773
1420	739	775
1430	740	775
1440	741	777
1450	742	778
1460	742	778
1470	743	778
1480	744	779
1490	745	780
1500	745	781
1510	745	782
1520	746	781
1530	746	782
1540	747	783
1550	749	784
1560	750	784
1570	751	785
1580	752	786
1591	752	788
1601	753	791
1611	754	791
1621	755	791
1631	756	791
1641	757	791
1651	756	792
1661	754	792
1671	753	792
1681	752	794
1691	751	794
1701	750	796
1711	750	796
1721	749	796
1731	749	797

Time (s)	Gas temperature for the fire test without PFP (°C)	Gas temperature for the fire test with PFP (°C)
1741	750	798
1751	751	799
1761	752	800
1771	753	801
1781	752	801
1791	752	801
1801	753	801
1811	754	803
1821	754	803
1831	755	805
1841	755	805
1851	756	806
1861	758	806
1871	760	807
1881	761	808
1891	761	808
1901	763	809
1911	763	810
1921	764	810
1931	765	811
1941	765	812
1951	765	814
1961	765	814
1971	766	814
1981	766	814
1991	766	815
2001	767	815
2011	768	815
2021	768	814
2031	768	814
2041	769	816
2051	770	816
2061	770	817
2071	770	818
2081	771	818
2091	772	818
2101	771	819
2111	772	820
2121	774	820
2131	774	821
2141	773	821
2151	773	822
2161	774	823
2171	774	824
2181	774	826

Time (s)	Gas temperature for the fire test without PFP (°C)	Gas temperature for the fire test with PFP (°C)
2191	774	827
2201	775	828
2211	775	829
2221	775	829
2231	777	828
2241	777	828
2251	777	828
2261	778	829
2271	779	828
2281	781	828
2291	782	829
2301	782	830
2311	782	830
2321	783	831
2331	784	832
2341	784	832
2351	785	832
2361	786	832
2371	787	832
2381	788	832
2391	789	833
2401	789	833
2411	788	833
2421	788	834
2431	788	834
2441	789	837
2451	791	837
2461	791	838
2471	792	839
2481	792	839
2491	793	840
2501	794	840
2511	794	841
2521	795	841
2531	796	841
2541	797	840
2551	798	840
2561	798	839
2571	798	838
2581	799	838
2591	801	839
2601	801	839
2611	801	838
2621	802	837
2631	804	837

Time (s)	Gas temperature for the fire test without PFP (°C)	Gas temperature for the fire test with PFP (°C)
2641	807	837
2651	808	838
2661	808	838
2671	807	837
2681	806	837
2691	806	838
2701	806	838
2711	807	840
2721	805	841
2731	792	842
2741	767	843
2751	732	843
2761	705	842
2771	676	840
2781	651	840
2791	627	840
2801	610	841
2811	592	841
2821	578	841
2831	567	842
2841	553	842
2851	544	842
2861	532	843
2871	524	843
2881	515	843
2891	508	844
2901	501	843
2911	495	843
2921	491	844
2931	483	845
2941	479	845
2951	473	845
2961	468	846
2971	463	846
2981	459	847
2991	455	847
3001	451	848
3011	447	849
3021	442	849
3031	440	848
3041	435	849
3051	432	849
3061	429	849
3071	425	850
3081	422	850

Time (s)	Gas temperature for the fire test without PFP (°C)	Gas temperature for the fire test with PFP (°C)
3091	418	850
3101	417	850
3111	412	850
3121	410	851
3131	406	855
3141	403	857
3151	399	859
3161	396	860
3171	394	860
3182	391	861
3192	389	861
3202	387	861
3212	385	860
3222	382	860
3232	380	861
3242	378	861
3252	376	860
3262	373	860
3272	372	859
3282	369	859
3292	367	860
3302	365	861
3312	363	861
3322	362	859
3332	359	859
3342	358	859
3352	356	860
3362	354	861
3372	352	861
3382	351	863
3392	350	863
3402	346	863
3412	345	863
3422	343	864
3432	341	863
3442	339	862
3452	337	862
3462	336	862
3472	334	861
3482	333	861
3492	331	861
3502	330	861
3512	327	861
3522	326	863
3532	325	863

Time (s)	Gas temperature for the fire test without PFP (°C)	Gas temperature for the fire test with PFP (°C)
3542	323	864
3552	322	865
3562	321	868
3572	320	872
3582	318	871
3592	317	871
3602	316	870
3612	315	869
3622	314	869
3632	313	869
3642	312	869
3652	311	868
3662	310	867
3672	309	868
3682	308	869
3692	307	870
3702	306	869
3712	305	869
3722	304	867
3732	303	867
3742	303	868
3752	302	868
3762	301	868
3772	300	867
3782	299	869
3792	299	869
3802	297	869
3812	296	869
3822	295	869
3832	295	869
3842	294	870
3852	293	871
3862	292	871
3872	291	871
3882	291	871
3892	290	871
3902	289	871
3912	288	872
3922	287	873
3932	286	873
3942	286	873
3952	285	873
3962	284	873
3972	284	873
3982	282	874

Time (s)	Gas temperature for the fire test without PFP (°C)	Gas temperature for the fire test with PFP (°C)
3992	282	873
4002	281	874
4012	280	873
4022	279	873
4032	278	874
4042	277	875
4052	276	875
4062	276	875
4072	275	875
4082	275	876
4092	274	877
4102	273	877
4112	272	878
4122	271	878
4132	270	878
4142	270	878
4152	269	879
4162	268	884
4172	267	889
4182	266	893
4192	266	897
4202	265	899
4212	264	904
4222	263	911
4232	262	915
4242	261	918
4252	261	921
4262	260	922
4272	259	922
4282	258	922
4292	257	921
4302	256	920
4312	256	919
4322	255	918
4332	254	918
4342	254	919
4352	253	922
4362	252	923
4372	252	923
4382	251	924
4392	250	924
4402	249	925
4412	249	925
4422	248	925
4432	247	926

Time (s)	Gas temperature for the fire test without PFP (°C)	Gas temperature for the fire test with PFP (°C)
4442	246	927
4452	246	925
4462	245	924
4472	244	924
4482	244	924
4492	243	923
4502	-	924
4512	-	927
4522	-	931
4532	-	932
4542	-	934
4552	-	934
4562	-	934
4572	-	934
4582	-	933
4592	-	933
4602	-	933
4612	-	932
4622	-	932
4632	-	934
4642	-	934
4652	-	935

Time (s)	Gas temperature for the fire test without PFP (°C)	Gas temperature for the fire test with PFP (°C)
4662	-	935
4672	-	935
4682	-	937
4692	-	939
4702	-	939
4712	-	940
4722	-	941
4732	-	941
4742	-	941
4752	-	942
4762	-	943
4773	-	944
4783	-	945
4793	-	946
4803	-	947
4813	-	947
4823	-	947
4833	-	946
4843	-	945
4853	-	944
4863	-	943
4864	-	943

A.6 Steel Temperatures for the Fire Test Without PFP as Shown in Figure 4.8

	Temperature (°C)	
Time (s)	Point D	Point P
0	28	28
10	36	36
20	42	42
30	49	49
40	56	55
50	65	62
60	68	66
70	78	72
80	84	77
90	90	83
100	96	89
110	102	94
120	108	100
130	113	105

	Temperature (°C)	
Time (s)	Point D	Point P
140	119	110
150	124	116
160	131	120
170	136	125
180	144	131
190	150	136
200	156	141
210	162	146
220	169	152
230	175	156
240	181	161
250	187	166
260	191	169
270	198	175

Time (s)	Temperature (°C)	
	Point D	Point P
280	203	179
290	211	185
300	216	189
310	222	194
320	227	198
330	233	202
340	238	206
350	241	210
360	249	215
370	252	218
380	258	223
390	263	227
400	268	231
410	272	234
420	277	238
430	282	242
440	285	244
450	292	249
460	297	252
470	302	256
480	306	259
490	311	262
500	316	266
510	320	269
520	325	272
530	329	274
540	334	278
550	336	280
560	341	284
570	345	286
580	348	289
590	353	292
600	356	294
610	361	297
620	364	299
630	368	302
640	371	304
650	376	306
660	379	308
670	383	311
680	387	313
690	392	315
700	396	317
710	400	320
720	404	322
730	408	324

Time (s)	Temperature (°C)	
	Point D	Point P
740	412	326
750	416	327
760	421	330
770	425	331
780	430	333
790	434	335
800	439	337
810	443	339
820	447	341
830	451	342
840	454	344
850	459	346
860	463	348
870	468	350
880	471	351
890	476	353
900	479	355
910	483	356
920	487	358
930	490	359
940	495	361
950	498	363
960	502	365
970	506	366
980	509	367
990	513	369
1000	516	371
1010	519	373
1020	520	374
1030	525	376
1040	528	376
1050	531	378
1060	534	380
1070	537	381
1080	540	383
1090	543	384
1100	546	386
1110	547	387
1120	551	388
1130	552	390
1140	556	391
1150	558	392
1160	561	394
1170	563	395
1180	564	396
1190	567	398

	Temperature (°C)	
Time (s)	Point D	Point P
1200	569	399
1210	571	400
1220	573	401
1230	575	403
1240	577	404
1250	580	406
1260	582	407
1270	583	408
1280	585	409
1290	587	411
1300	588	412
1310	590	413
1320	591	414
1330	593	415
1340	595	416
1350	597	417
1360	599	419
1370	600	420
1380	601	421
1390	603	422
1400	603	423
1410	606	424
1420	606	425
1430	609	426
1440	610	427
1450	611	428
1460	612	429
1470	614	430
1480	615	432
1490	616	432
1500	618	433
1510	619	434
1520	620	436
1530	621	436
1540	623	438
1550	624	438
1560	625	439
1570	626	440
1580	627	441
1591	628	442
1601	629	443
1611	631	444
1621	631	445
1631	633	445
1641	633	447
1651	634	447

	Temperature (°C)	
Time (s)	Point D	Point P
1661	634	447
1671	635	448
1681	635	449
1691	635	450
1701	636	450
1711	636	451
1721	636	452
1731	637	452
1741	637	453
1751	638	454
1761	638	455
1771	639	455
1781	639	456
1791	640	457
1801	640	457
1811	641	458
1821	641	459
1831	642	460
1841	642	460
1851	643	461
1861	643	462
1871	643	462
1881	644	463
1891	644	464
1901	644	465
1911	645	465
1921	645	466
1931	646	466
1941	646	467
1951	647	468
1961	647	468
1971	647	469
1981	647	469
1991	648	470
2001	648	471
2011	648	471
2021	648	472
2031	649	472
2041	649	473
2051	650	473
2061	650	474
2071	651	474
2081	651	475
2091	652	476
2101	652	476
2111	653	477

	Temperature (°C)	
Time (s)	Point D	Point P
2121	653	477
2131	653	478
2141	654	478
2151	654	479
2161	655	480
2171	655	480
2181	656	480
2191	656	481
2201	657	481
2211	657	482
2221	657	482
2231	658	483
2241	658	484
2251	658	485
2261	659	485
2271	659	485
2281	659	486
2291	660	486
2301	660	487
2311	660	487
2321	660	488
2331	661	488
2341	661	489
2351	661	489
2361	661	490
2371	662	491
2381	662	491
2391	663	492
2401	663	492
2411	663	493
2421	664	493
2431	664	493
2441	664	494
2451	665	494
2461	665	495
2471	665	495
2481	665	496
2491	666	496
2501	666	497
2511	666	497
2521	666	498
2531	666	498
2541	666	498
2551	666	499
2561	666	499
2571	666	500

	Temperature (°C)	
Time (s)	Point D	Point P
2581	666	500
2591	666	501
2601	666	501
2611	666	501
2621	666	501
2631	666	501
2641	666	502
2651	666	503
2661	667	503
2671	668	504
2681	668	504
2691	669	505
2701	670	505
2711	670	505
2721	669	505
2731	666	504
2741	662	502
2751	655	499
2761	649	496
2771	643	493
2781	638	490
2791	632	487
2801	628	484
2811	622	481
2821	617	478
2831	613	476
2841	608	472
2851	603	469
2861	597	466
2871	594	463
2881	589	460
2891	585	458
2901	580	454
2911	576	452
2921	574	450
2931	568	446
2941	564	444
2951	559	440
2961	556	438
2971	552	435
2981	548	433
2991	544	430
3001	540	427
3011	538	426
3021	533	422
3031	531	420

	Temperature (°C)	
Time (s)	Point D	Point P
3041	526	417
3051	523	415
3061	520	412
3071	516	410
3081	513	407
3091	509	405
3101	508	403
3111	503	400
3121	500	398
3131	496	395
3141	493	393
3151	490	390
3161	487	388
3171	484	386
3182	481	383
3192	478	381
3202	475	379
3212	472	377
3222	470	374
3232	467	373
3242	465	371
3252	462	368
3262	459	366
3272	457	364
3282	454	362
3292	452	360
3302	450	358
3312	447	356
3322	446	354
3332	442	352
3342	440	350
3352	438	348
3362	436	346
3372	433	345
3382	431	343
3392	429	341
3402	427	339
3412	425	338
3422	422	336
3432	420	334
3442	418	332
3452	416	330
3462	413	329
3472	411	326
3482	409	325
3492	407	324

	Temperature (°C)	
Time (s)	Point D	Point P
3502	405	323
3512	402	320
3522	401	319
3532	399	317
3542	397	316
3552	395	314
3562	393	313
3572	391	312
3582	389	310
3592	388	309
3602	386	307
3612	384	306
3622	382	305
3632	380	303
3642	379	302
3652	377	301
3662	375	300
3672	373	298
3682	372	297
3692	370	296
3702	368	295
3712	366	294
3722	365	292
3732	363	291
3742	361	290
3752	360	289
3762	358	288
3772	356	286
3782	355	285
3792	354	285
3802	352	283
3812	351	282
3822	349	281
3832	348	280
3842	346	279
3852	345	278
3862	343	277
3872	342	276
3882	342	274
3892	340	274
3902	339	273
3912	337	272
3922	336	271
3932	335	270
3942	333	269
3952	332	268

	Temperature (°C)	
Time (s)	Point D	Point P
3962	331	267
3972	330	266
3982	329	265
3992	328	264
4002	326	263
4012	325	262
4022	324	261
4032	323	260
4042	322	259
4052	321	258
4062	320	258
4072	319	257
4082	318	256
4092	317	255
4102	315	254
4112	314	253
4122	313	252
4132	312	252
4142	311	251
4152	311	250
4162	309	249
4172	309	248
4182	307	247
4192	306	247
4202	305	246
4212	304	245
4222	303	244

	Temperature (°C)	
Time (s)	Point D	Point P
4232	302	243
4242	301	242
4252	300	242
4262	300	241
4272	299	240
4282	298	240
4292	297	239
4302	296	238
4312	295	237
4322	294	236
4332	293	235
4342	292	234
4352	291	234
4362	290	233
4372	289	232
4382	288	231
4392	287	231
4402	286	230
4412	286	230
4422	285	229
4432	284	228
4442	283	228
4452	282	227
4462	281	226
4472	280	225
4482	279	225
4492	278	224

A.7 Steel Temperatures for the Fire Test With PFP as Shown in Figure 4.9

	Temperature (°C)		
Time (s)	Point D	Point P	Point C
0	18	17	17
10	25	29	17
20	33	38	17
30	44	47	17
40	53	54	17
50	61	61	17
60	68	67	17
70	75	72	17
80	80	75	17
90	85	79	17
100	91	83	17

	Temperature (°C)		
Time (s)	Point D	Point P	Point C
110	95	86	17
120	99	89	17
130	103	93	17
140	106	96	17
150	108	99	18
160	114	104	18
170	118	109	18
180	123	113	18
190	127	118	18
200	132	122	18
210	137	127	18

	Temperature (°C)		
Time (s)	Point D	Point P	Point C
220	143	132	18
230	148	137	18
240	153	141	18
250	160	148	18
260	164	152	18
270	172	159	18
280	177	164	18
290	184	170	18
300	189	175	18
310	196	181	19
320	202	186	19
330	208	191	19
340	214	197	19
350	219	201	19
360	225	207	19
370	230	211	19
380	237	217	19
390	243	222	19
400	248	227	19
410	254	232	20
420	258	236	20
430	266	242	20
440	269	245	20
450	277	252	20
460	283	256	20
470	289	261	20
480	295	266	21
490	300	270	21
500	306	275	21
510	312	279	21
520	319	284	21
530	323	287	21
540	330	293	21
550	334	296	22
560	341	300	22
570	346	304	22
580	350	306	22
590	356	310	22
600	361	312	23
610	365	314	23
620	367	316	23
630	372	318	23
640	377	320	24
650	381	322	24
660	385	324	24
670	389	326	25
680	393	329	25

	Temperature (°C)		
Time (s)	Point D	Point P	Point C
690	397	331	25
700	401	334	25
710	405	336	26
720	410	339	26
730	413	341	26
740	419	345	27
750	423	347	27
760	427	349	27
770	431	351	28
780	434	353	28
790	437	354	28
800	441	355	29
810	444	357	29
820	447	358	29
830	451	360	30
840	453	361	30
850	457	362	30
860	460	364	31
870	464	366	31
880	467	367	31
890	470	368	32
900	473	369	32
910	475	370	32
920	480	372	33
930	482	372	33
940	486	374	34
950	489	375	34
960	492	376	34
970	495	377	35
980	497	378	35
990	500	380	36
1000	502	380	36
1010	507	382	36
1020	509	383	37
1030	514	384	37
1040	517	386	37
1050	519	387	38
1060	522	388	38
1070	525	389	38
1080	527	390	39
1090	529	391	39
1100	532	392	40
1110	534	393	40
1120	537	394	41
1130	540	396	41
1140	543	397	42
1150	546	398	42

	Temperature (°C)		
Time (s)	Point D	Point P	Point C
1160	548	399	42
1170	551	401	43
1180	552	402	43
1190	556	403	44
1200	558	404	44
1210	561	405	45
1220	562	406	45
1230	564	407	45
1240	566	408	46
1250	568	409	46
1260	570	410	47
1270	572	411	47
1280	573	412	48
1290	575	413	48
1300	577	414	48
1310	579	415	49
1320	581	417	49
1330	583	418	50
1340	586	420	50
1350	588	421	51
1360	590	422	51
1370	592	424	52
1380	593	425	52
1390	596	426	53
1400	598	427	53
1410	600	428	54
1420	602	429	54
1430	603	431	54
1440	605	432	55
1450	606	433	55
1460	608	434	56
1470	608	435	56
1480	611	436	57
1490	612	437	57
1500	614	438	58
1510	615	439	58
1520	617	440	59
1530	618	441	59
1540	619	442	60
1550	620	443	60
1560	622	444	60
1570	623	445	61
1580	624	446	61
1591	626	447	62
1601	627	447	62
1611	628	449	63
1621	629	450	64

	Temperature (°C)		
Time (s)	Point D	Point P	Point C
1631	631	450	64
1641	632	451	64
1651	633	452	65
1661	634	453	65
1671	635	454	66
1681	636	455	66
1691	637	455	67
1701	638	457	67
1711	639	457	68
1721	640	458	68
1731	641	459	69
1741	642	460	69
1751	642	461	70
1761	643	461	70
1771	645	462	71
1781	646	463	71
1791	647	464	72
1801	648	465	72
1811	649	466	73
1821	650	466	73
1831	651	467	74
1841	652	468	75
1851	652	469	75
1861	653	470	76
1871	654	470	77
1881	655	471	78
1891	655	472	78
1901	656	472	79
1911	657	473	80
1921	658	474	81
1931	659	475	82
1941	659	475	82
1951	660	476	83
1961	661	477	84
1971	661	477	85
1981	662	478	85
1991	662	479	86
2001	663	479	87
2011	664	480	88
2021	664	481	89
2031	665	481	89
2041	666	482	90
2051	666	483	91
2061	667	483	92
2071	667	484	93
2081	668	485	93
2091	669	485	94

	Temperature (°C)		
Time (s)	Point D	Point P	Point C
2101	669	486	95
2111	670	486	96
2121	671	487	97
2131	671	488	98
2141	672	488	98
2151	673	489	99
2161	673	489	100
2171	674	490	101
2181	675	491	102
2191	676	491	103
2201	676	492	104
2211	677	492	105
2221	677	493	105
2231	678	493	106
2241	679	494	107
2251	679	494	108
2261	680	495	109
2271	681	496	110
2281	681	496	111
2291	682	497	112
2301	682	497	112
2311	683	498	113
2321	684	498	114
2331	685	498	115
2341	685	499	116
2351	686	500	117
2361	686	500	118
2371	687	501	119
2381	687	501	120
2391	688	502	121
2401	688	502	122
2411	689	503	122
2421	690	503	123
2431	690	503	124
2441	691	504	125
2451	691	504	126
2461	692	505	127
2471	692	505	128
2481	693	506	129
2491	693	506	130
2501	694	507	131
2511	695	507	132
2521	695	508	132
2531	696	508	134
2541	696	509	134
2551	697	509	136
2561	697	509	137

	Temperature (°C)		
Time (s)	Point D	Point P	Point C
2571	697	510	137
2581	697	510	138
2591	697	510	139
2601	697	510	140
2611	697	510	141
2621	698	510	142
2631	698	511	143
2641	698	511	144
2651	698	511	145
2661	699	511	146
2671	699	511	147
2681	699	512	148
2691	699	512	149
2701	700	512	149
2711	700	513	151
2721	700	513	152
2731	700	513	153
2741	700	513	154
2751	701	514	155
2761	701	514	156
2771	701	514	157
2781	702	514	157
2791	702	514	158
2801	701	515	159
2811	701	515	160
2821	701	515	161
2831	701	515	162
2841	702	515	163
2851	702	515	164
2861	703	516	165
2871	703	516	166
2881	704	516	167
2891	704	516	168
2901	704	517	169
2911	704	517	170
2921	705	517	171
2931	705	517	172
2941	705	517	173
2951	706	518	174
2961	706	518	175
2971	706	518	176
2981	707	519	177
2991	707	519	178
3001	707	519	179
3011	708	519	180
3021	708	520	181
3031	708	520	182

	Temperature (°C)		
Time (s)	Point D	Point P	Point C
3041	708	520	183
3051	709	520	184
3061	709	521	184
3071	709	521	186
3081	709	521	187
3091	710	521	188
3101	710	522	189
3111	710	522	190
3121	710	522	191
3131	711	522	192
3141	711	523	193
3151	711	523	194
3161	711	523	195
3171	711	524	195
3182	712	524	197
3192	712	525	198
3202	712	525	199
3212	713	526	200
3222	713	526	201
3232	713	526	202
3242	713	527	203
3252	714	527	204
3262	714	527	204
3272	714	528	206
3282	714	528	206
3292	715	528	208
3302	715	529	209
3312	715	529	210
3322	716	529	211
3332	716	529	212
3342	716	529	212
3352	717	530	213
3362	717	530	215
3372	717	530	215
3382	718	531	216
3392	718	531	217
3402	718	531	218
3412	719	532	219
3422	719	532	220
3432	719	532	221
3442	719	532	222
3452	720	532	223
3462	720	532	224
3472	720	533	225
3482	720	533	226
3492	720	533	227
3502	721	533	228

	Temperature (°C)		
Time (s)	Point D	Point P	Point C
3512	721	533	229
3522	721	534	230
3532	722	534	231
3542	722	534	232
3552	722	534	233
3562	723	535	234
3572	723	535	235
3582	723	535	236
3592	723	536	237
3602	724	536	238
3612	724	536	239
3622	724	536	239
3632	725	537	240
3642	725	537	241
3652	726	537	242
3662	726	538	243
3672	726	538	244
3682	726	538	245
3692	726	539	246
3702	726	539	247
3712	727	539	248
3722	727	539	249
3732	727	539	249
3742	727	540	251
3752	727	540	252
3762	728	540	252
3772	728	540	254
3782	728	541	255
3792	728	541	255
3802	729	541	256
3812	729	541	257
3822	729	541	258
3832	729	542	259
3842	730	542	260
3852	730	542	261
3862	730	542	262
3872	730	542	263
3882	731	543	264
3892	731	543	265
3902	731	543	265
3912	731	544	266
3922	732	544	267
3932	732	544	268
3942	732	544	269
3952	732	544	270
3962	733	545	271
3972	733	545	272

	Temperature (°C)		
Time (s)	Point D	Point P	Point C
3982	733	545	273
3992	733	545	274
4002	733	545	275
4012	734	546	276
4022	734	546	276
4032	734	546	277
4042	734	546	278
4052	734	547	279
4062	734	547	280
4072	734	547	281
4082	734	547	282
4092	735	547	282
4102	735	547	283
4112	735	547	284
4122	735	548	285
4132	735	548	286
4142	735	548	287
4152	736	549	288
4162	736	549	289
4172	736	550	290
4182	736	550	290
4192	736	550	291
4202	737	550	292
4212	738	551	293
4222	739	552	294
4232	740	552	295
4242	742	553	296
4252	743	554	297
4262	745	555	298
4272	746	556	298
4282	748	556	299
4292	749	557	300
4302	750	558	301
4312	751	558	302
4322	752	559	303
4332	753	560	303
4342	754	561	304
4352	755	562	305
4362	756	563	306
4372	756	563	307
4382	756	564	307
4392	757	565	309
4402	757	565	310
4412	757	566	310
4422	757	566	311
4432	758	567	312

	Temperature (°C)		
Time (s)	Point D	Point P	Point C
4442	758	568	313
4452	759	568	314
4462	759	568	315
4472	759	569	315
4482	760	570	316
4492	760	570	317
4502	760	570	318
4512	761	571	319
4522	762	571	320
4532	764	572	321
4542	765	573	322
4552	765	573	322
4562	766	574	323
4572	767	574	324
4582	768	575	325
4592	769	575	326
4602	770	576	327
4612	771	576	328
4622	772	577	329
4632	773	577	329
4642	774	578	330
4652	774	578	331
4662	775	578	332
4672	775	579	332
4682	776	580	334
4692	776	580	334
4702	776	580	335
4712	777	581	336
4722	778	581	337
4732	779	582	338
4742	779	582	339
4752	779	583	339
4762	780	583	340
4773	780	583	341
4783	781	584	342
4793	781	584	343
4803	782	585	344
4813	782	585	345
4823	782	586	345
4833	782	586	346
4843	783	586	347
4853	783	587	348
4863	783	587	349
4864	783	587	349

A.8 Time History of Lateral Deformations at the Three Monitoring Points Obtained from the Test Without PFP as Shown in Figure 3.36

Time (s)	Lateral deformation (mm)		
	C1	C2	C3
0	-4.24	-4.61	-4.11
100	-7.42	-8.01	-7.32
200	-10.79	-11.92	-10.43
300	-12.91	-15.02	-12.54
400	-14.26	-16.52	-13.44
500	-14.55	-17.22	-13.24
600	-13.69	-16.62	-12.14
700	-12.05	-15.62	-10.23
800	-10.41	-14.02	-8.23
900	-8	-12.42	-6.12
1000	-6.17	-11.21	-3.51
1100	-4.05	-9.61	-0.9
1200	-2.31	-8.81	1.2
1300	-0.77	-7.91	3.41
1400	0.39	-7.51	4.92
1500	1.25	-7.61	6.22
1580	-122.02	-141.28	-113.46
1600	-136.28	-155.5	-126.9

Time (s)	Lateral deformation (mm)		
	C1	C2	C3
1630	-148.04	-167.42	-137.84
1700	-165.68	-185.34	-154.29
1800	-184.09	-203.46	-171.35
1900	-199.12	-218.68	-185.89
2000	-212.81	-232.5	-198.93
2100	-225.91	-245.72	-212.48
2200	-238.93	-258.14	-225.22
2300	-250.4	-269.85	-236.65
2400	-263.5	-282.57	-249.7
2500	-265.71	-286.77	-253.71
2600	-260.19	-278.26	-248.19
2700	-253.17	-271.35	-241.17
2800	-248.05	-266.35	-236.05
2823	-246.95	-265.34	-234.95
2900	-	-262.14	-232.34
3000	-	-258.94	-229.83
3100	-	-256.43	-227.43
3200	-	-254.23	-226.02

A.9 Time History of Lateral Deformations at the Three Monitoring Points Obtained from the Test With PFP as Shown in Figure 3.42

Time (s)	Lateral deformation (mm)		
	C1	C2	C3
1	-3.47	-3.49	-3.61
101	-1.35	-1.2	-1.5
201	0.29	0	-0.1
301	2.12	1.39	1.61
401	3.47	2.49	2.91
501	4.63	3.79	4.31
601	6.26	5.58	5.82
701	11.08	10.66	10.33
801	13.49	13.75	12.94
901	16	16.04	15.15
1001	20.53	20.43	19.46
1101	23.03	22.52	21.67
1201	24.77	24.71	24.08
1301	26.6	26.11	25.58
1401	28.43	27.5	27.59
1501	29.97	28.5	29.19
1591	30.84	29.19	30.6
1601	36.34	34.48	35.81
1665	17.16	13.35	17.26

Time (s)	Lateral deformation (mm)		
	C1	C2	C3
1701	16.58	12.46	16.65
1801	15.61	10.46	16.35
1901	14.75	8.97	15.95
2001	14.26	6.97	15.65
2101	13.4	4.98	15.35
2201	12.24	3.39	14.85
2301	11.47	1	14.45
2401	10.7	-1.1	13.84
2501	9.45	-2.69	13.64
2601	8.39	-5.08	13.04
2701	7.61	-7.17	12.84
2801	6.46	-9.27	12.64
2901	4.72	-12.06	11.14
3001	2.6	-14.85	10.13
3091	1.16	-16.54	9.93
3101	-13.3	-32.08	-3.21
3201	-216.65	-268.13	-206.56
3250	-268.51	-322.34	-258.42
3298	-261.19	-315.56	-251.1